Human In Vitro Models of Pediatric Muscular Diseases

Permanent link

Terms of Use

Share Your Story

Accessibility

Human *In Vitro* Models of Pediatric Muscular Diseases

A dissertation presented

by

Alexander Peyton Nesmith

to

The John A. Paulson School of Engineering and Applied Sciences

in partial fulfillment of the requirements
for the degree of

Doctor of Philosophy

in the subject of

Engineering Sciences

Harvard University
Cambridge, Massachusetts

December, 2016

Dissertation Advisor: Professor Kevin Kit Parker   Author: Alexander Peyton Nesmith

Human *In Vitro* Disease Models of Pediatric Muscular Diseases

Abstract

The development of new therapies for pediatric diseases over the past few decades has been hampered by a lack of human-relevant model systems and inherent challenges with pediatric clinical trials. In particular, many diseases of childhood are rare genetic diseases that limit clinical trial utility due to small patient populations. Recent advances in stem cell, gene editing, and organ on chip technologies present a unique opportunity to develop *in vitro* analogs of pediatric patients that can potentially expedite drug screening and development. Here, we review the spatiotemporal scales of muscular diseases of childhood in order to specify the design criteria of *in vitro* disease models requisite for recapitulation of diseased muscle structure and function. Moreover, we review advances in the development of induced pluripotent stem cell-derived muscle, gene editing, as well as approaches to mimic diseased microenvironments *in vitro*. Next, we present an *in vitro* model of allergic asthma developed using human cells. We replicated the laminar, anisotropic structure of the human airway musculature through microcontact printing of extracellular matrix protein cues. To mimic the inflammation critical for driving airway dysfunction, we treated the engineered airway smooth muscle tissues with interleukin-13, a known mediator of asthma. We tested our system by replicating the cholinergic challenge, used clinically to diagnose asthma, *in vitro*. We found that interleukin-13 promoted hypercontractility in the engineered airway smooth muscle, but even hypercontractions could be

reversed using standard airway drugs, an important hallmark that distinguishes asthma from other obstructive diseases of the airway. Furthermore, we observed that interleukin-13 promoted greater cell spreading, increased alignment of the actin cytoskeleton, and upregulation of RhoA. As a proof of principle, we targeted the RhoA-ROCK pathway and demonstrated ROCK inhibition could both prevent hypercontractions and improve airway smooth muscle relaxation beyond existing therapies. Lastly, we present a model Duchenne muscular dystrophy (DMD), the most common childhood-lethal genetic disease. Specifically, we sought to recapitulate the impaired muscular repair and contractile weakness of DMD skeletal muscle. We found that myoblasts, a muscle stem cell, from DMD patients failed to align and polarize with respect to the extracellular matrix cues, resulting in poorer muscle formation and maturation. These deficits in muscle formation were reflected by profound contractile weakness in these tissues, as observed in quantitative muscle testing performed clinically. Collectively, these human-derived *in vitro* diseases models represent substantial progress towards the ultimate goal of replacing animal models with human-based models in preclinical trials.

Table of Contents

Table of Figures

Acknowledgments

The path to earning a PhD is long and arduous, having less to do with intelligence and more to do with grit, persistence, and patience. I am very grateful to my parents, Nick and Elizabeth Nesmith, for instilling these virtues through example throughout my life. Although, growing up I did not always recognize the effort and sacrifices they endured to ensure my sisters and I had every opportunity imaginable available to us, the daily grind of successes and failures throughout my PhD provided me a better perspective. When I faced tough times and wanted to quit, I often reflected on my mother's grit. When I was in 5th grade, she was diagnosed with breast cancer and persevered through radiation and chemotherapy. But not only did she endure the miserable days of these treatments, she also continued to work as a certified public accountant, even through the crazy hours of tax season. If she didn't make excuses, I knew I couldn't make any excuses. I knew that I didn't know what it meant to be tired or miserable. From my father, I have learned ambition and vision. Although his profession is real estate, he has great passion for art and architecture that is evident from walking around our home where his prolific production of artwork is quite evident. Growing up, his restlessness always drove me crazy. He was always working on something – paintings of all types, building gates and walkways in our yard, whatever project was next. We would drive around seemingly endlessly looking at houses as he drew inspiration or maybe even collecting stones or wood that could be useful for yet another new project. My PhD has proven to me how valuable it is to constantly seek improvement, to never be satisfied. I love and appreciate my parents and could not have achieved a PhD without them. I also have immense gratitude for my sisters, Haley and Whitney. My older sister Whitney has always set an example for me in school, sports, and now in parenthood as an adult. She has always been extremely diligent and hardworking. I'm lucky to

have had such high expectations to live up to my whole life. And, it has come to my great relief to realize that the rest of the world is not composed of people as smart and talented as my younger sister Haley. To me, growing up, it seemed impossible to impress anyone with her around. I'm so thankful for her energy, constant stream of ideas, and her friendship, particularly in the last year of my PhD while she has lived in Boston.

I am similarly indebted to the members of the Disease Biophysics Group, my team, and the numerous friends and mentors that have taught and supported me throughout my undergraduate research experiences into my graduate work. I'd like to specifically thank Borna Dabiri, Pat Alford, Ashu Agarwal, Leila Deravi, Francesco Pasqualini, Sung Jin Park, Johan Lind, Megan McCain, and Andrew Capulli for their mentorship and friendships. And additionally, I'd like to acknowledge the great collaborators I've had throughout my PhD. Mark Pincus and Paul August from Sanofi and now Icagen provided me a unique insight into drug development from the perspective of a pharmaceutical company. Their experience and insights were critical for our project's success. And lastly, my collaborators Professor Olivier Pourquie and Jerome Chal, whom we are continuing to work with. Their expertise in stem cell biology and specifically muscle biology have played a crucial role in our progress to date.

Lastly, I would like to thank Kit Parker. I met Kit as an undergraduate and my life forever changed. He has constantly pushed, challenged, and most often demanded that I get better in every facet of science and life. He is the only person I have ever met that has had higher expectations for me than myself and for that I am extremely humbled and grateful. For I know that is an extremely difficult role to take on. His honesty and bluntness have pushed me to do more than I ever imagined accomplishing. He continues to serve as an inspiration to me through is incredible dedication and commitment to his country, his community, his research group, his

students, and his family. He is a mentor and friend whose relationship I will value for the rest of my life.

1 Muscular Diseases in Children – Can Organ on Chips Improve the Current Paradigm for Pediatric Clinical Trials?

1.1 Introduction

Pediatric clinical trials face significant challenges due to inherently smaller patient populations[1, 2]. Clinical trials rely on large patient populations in order to achieve the statistical power needed to distinguish treatment effect[3]. However, many of the diseases that afflict children are rare genetic diseases like Duchenne muscular dystrophy (DMD)[4]. In addition, the specificity of emerging therapeutic approaches such as morpholino antisense oligomers[1] and CRISPR/Cas9[5, 6] presents similar issues due to the targeting of genetic mutations implicated in disease subpopulations[1, 7]. In 2012, in effort to minimize the barriers for development of therapies for rare diseases, the FDA Safety and Innovation Act was passed to expand approval of new drugs on the basis of drug effects on surrogate endpoints likely to predict clinical benefit for serious conditions that lack effective treatments, instead of randomized controlled trials designed to assess a clinical effect[8]. However, the recent, controversial approval of eteplirsen (Exondys 51)[1], a morpholino antisense oligomer therapy for DMD, highlights the persisting challenges of rare disease clinical trials that have small numbers of patients. Hence, new tools are needed to supplement rare disease clinical trials with human safety and efficacy data in order to speed the development of new therapies.

Traditionally, human diseases are modeled using animal models, which are often used in preclinical screening prior to drug testing in humans. But, these pre-clinical animal models often fail to predict drug toxicity and efficacy in human patients, as just 12% of drugs[9] that

successfully proceed through the preclinical stage of drug approval are eventually approved by the FDA due to safety or efficacy issues in human patients. One reason for this failure is the poor recapitulation of the spatiotemporal scales of human disease in animal models. For example, in the primary mouse model of DMD, skeletal muscle exhibits an upregulation of the protein utrophin[10], which functions similarly to the absent protein dystrophin, unlike human forms of DMD[11]. As consequence, decreased muscle degeneration and improved muscle regeneration are observed in these mice compared to human DMD patients, resulting in a less severe disease phenotype[11-13]. Hence, it is unsurprising that therapies optimized to improve the condition in mice have not yielded an efficacious therapy for humans.

The development of human-relevant organ-on-chips in conjunction with advances in stem cell biology[14-19] and gene editing techniques[15, 20, 21] can provide the basis for improved models of human disease and thus enable a new paradigm for testing drug safety and efficacy in pediatric diseases. Improved *in vitro* models of pediatric diseases can be engineered through the reconstitution of native microenvironmental cues in the form of cellular, mechanical, and chemical components. Moreover, *in vitro* systems are amenable to quantification of many clinically-relevant readouts such as protein expression, tissue structure, and functional readouts like contractile force[16]. Hence, engineering *in vitro* systems that possess functional readouts that register with clinical diagnostics could significantly supplement clinical trials. And while significant progress has been made in *in vitro* modeling of the liver [22-26], the kidney [27, 28], the heart [16, 29-32], the small airway [33, 34], the alveolus [35, 36], and the gut [37-39] using human-derived cells, *in vitro* models that recapitulate diseases of skeletal and smooth muscle in children remain an unmet need.

1.2   Design Considerations for *In Vitro* Models of Pediatric Muscle Diseases

1.2.1   The Spatiotemporal Scales of Skeletal Muscle Diseases

The goal of organ on chips is to mimic the simplest structural and functional units of tissues and organs that enable recapitulation of human organ function[36, 40]. *In vivo*, skeletal muscle is critical for locomotion, breathing, mastication and swallowing, vision, as well as maintenance of sphincter tone for urinary and fecal continence. These functions are facilitated by a highly ordered, multi-scale hierarchical structure. Tensional forces are generated by nanoscale actomyosin crossbridging interactions within microscale contractile apparati, called sarcomeres. Assemblies of linear arrays of sarcomeres, called myofibrils, extend beyond the millimeter length scale along the entire length of a single myofiber and couple to each other radially within the cellular cytosol through cytoskeletal linkages enabling generation of the strong forces requisite for organ-scale movement. Forces generated within myofibrils are transmitted from inside the myofiber extracellularly to a fibrous network of connective tissue that envelops myofibers through the transmembrane dystroglycan complexes and integrins that couple of the cellular cytoskeleton to the extracellular matrix (ECM). The ECM of skeletal muscle is a hierarchal structure, where the basal lamina surrounding a single myofiber integrates continuously with the connective tissue of thousands of myofibers thereby facilitating coordinated force transmission from thousands of myofibers to a single tendon to actuate movement[41]. The assembly of single myofibers into tissue and organ structures differs throughout the body. Within large leg muscles, myofibers are aligned anisotropically within densely packed, 3-dimensional structures that enable generation of strong forces. Whereas, the myofibers within the tongue that enable sagittal bending during swallowing assemble as a thin laminar, anisotropic skeletal muscle tissue. Hence, it is most critical to replicate the architecture

of sub-myofiber scales in order to replicate the simplest structural and functional unit of skeletal muscle.

In developing *in vitro* disease models of skeletal muscle, it is similarly critical to replicate the spatiotemporal scales of disease. The majority of skeletal muscle diseases of childhood result from single gene mutations that scale across several orders of spatial magnitude to result in clinical symptoms. For example, in Duchenne muscular dystrophy (DMD), a mutation in the dystrophin gene results in loss of expression of the dystroglycan complex within the sarcolemma of myofibers, potentiating injury at a single cell-level that scales to the organ and patient-level in the form of clinical symptoms such as weakness that disrupts the patients' ability to walk, eat, breathe, and ultimately survive (Fig.1-1). Moreover, skeletal muscle diseases manifest over many temporal scales. In DMD, dystrophin-deficiency results in muscle weakness and injury acutely, and repeated cycles of muscle injury and failed muscle repair over the time course of days and weeks results in progression of replacement of muscle with fibrofatty tissue over a time course of years that ultimately results in early patient death (Fig. 1-1).
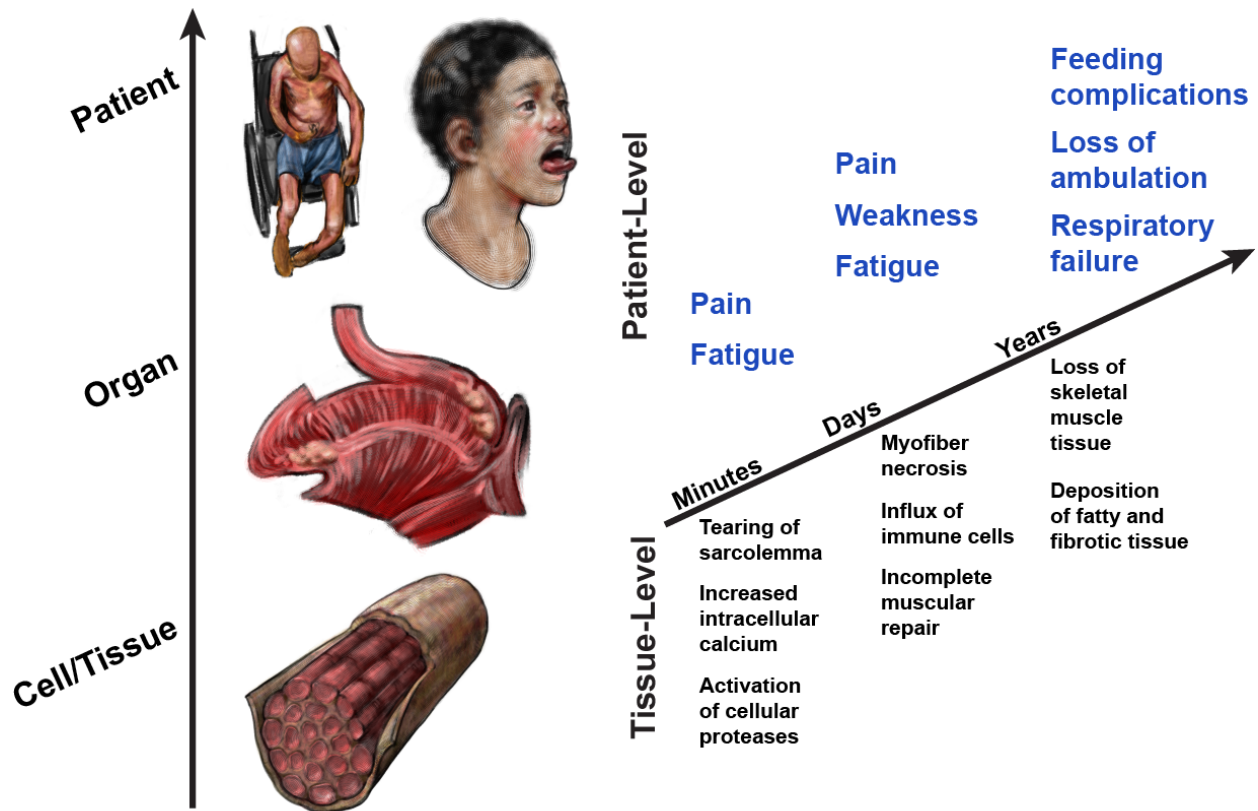
Figure 1-1. Spatiotemporal scales of skeletal muscle diseases of childhood.

1.2.2 The Spatiotemporal Scales of Smooth Muscle Diseases

Smooth muscle lines airways, vasculature, gastrointestinal tract, sphincters, and the stomach and function to modulate the flow of air, blood, waste, and digested food through the body. Within the walls of these organs, anisotropic smooth muscle tissue layers [42, 43] wrap circumferentially or helically around the lumen such that muscle contraction causes narrowing of the lumen restricting the flow of fluids like air and blood and initiating flow of solids like digested food. Similar to skeletal muscle, smooth muscle generates tensional forces within its cytoskeleton through interactions of actin and myosin [44]. However, in contrast to skeletal muscle, actin and myosin are not organized into periodic structures like sarcomeres[44]. Instead, actin filaments anchor to the plasma membrane at sites called dense plaques via a complex of adhesion proteins including talin, vinculin, paxillin, and α-actinin which couple actin to the cytoplasmic tails of integrin proteins, which couples the cell's cytoskeleton to the ECM, or to cadherin proteins, which mechanically couple adjacent cells [44-48]. Actin filaments extend in each direction from the dense bodies in parallel with the longitudinal axis of the cell and hence form a principal axis for force generation.

Throughout health and disease, smooth muscle exhibits a range of phenotypes ranging from quiescent and contractile to proliferative and migratory[43, 49]. In order to modulate their phenotype, smooth muscle cells sense and transduce chemical and mechanical cues within the microenvironment and remodel their cytoskeleton, alter expression of contractile proteins, and modulate the composition of cellular organelles within the cytosol[49]. Throughout the body, smooth muscle is exposed to a broad range of mechanical and chemical cues including pulsatile flow, shear stresses, tensile stress, inflammation, as well as contractile and relaxation agonists. In contrast to skeletal muscle, the majority of diseases affecting smooth muscle in pediatric

populations are caused by changes to microenvironmental cues that in turn modulate the phenotype or contractile state of smooth muscle cells rather than genetic mutations[43, 50-52]. For example, in asthma, hypersensitivity of the immune system triggers large immune responses when exposed to allergens and other stimuli[53]. The immune response causes immune cells to secrete chemicals called cytokines that can act directly on membrane-bound receptors of smooth muscle, eliciting changes in cellular behavior that can include increased contractility, increased proliferation, and increased ECM deposition as well as many other functions[53]. These distinct consequences of inflammation manifest over several orders of temporal magnitude (Fig. 1-2). In asthma, an early phase immune response can trigger smooth muscle contraction resulting in airway narrowing on a time scale of minutes that traps carbon dioxide within the lungs. Hours later, the early phase immune response is followed by a second immune response that occurs as consequence of recruitment of more immune cells to the airway wall that again elicits dangerous airway narrowing causing the clinical symptoms of coughing and breathlessness. Over a time course of years, uncontrolled inflammation potentiates remodeling of the airway wall causing a transition from disease of reversible airway narrowing to irreversible airway narrowing due to increased deposition of fibrotic tissue within the airway wall.
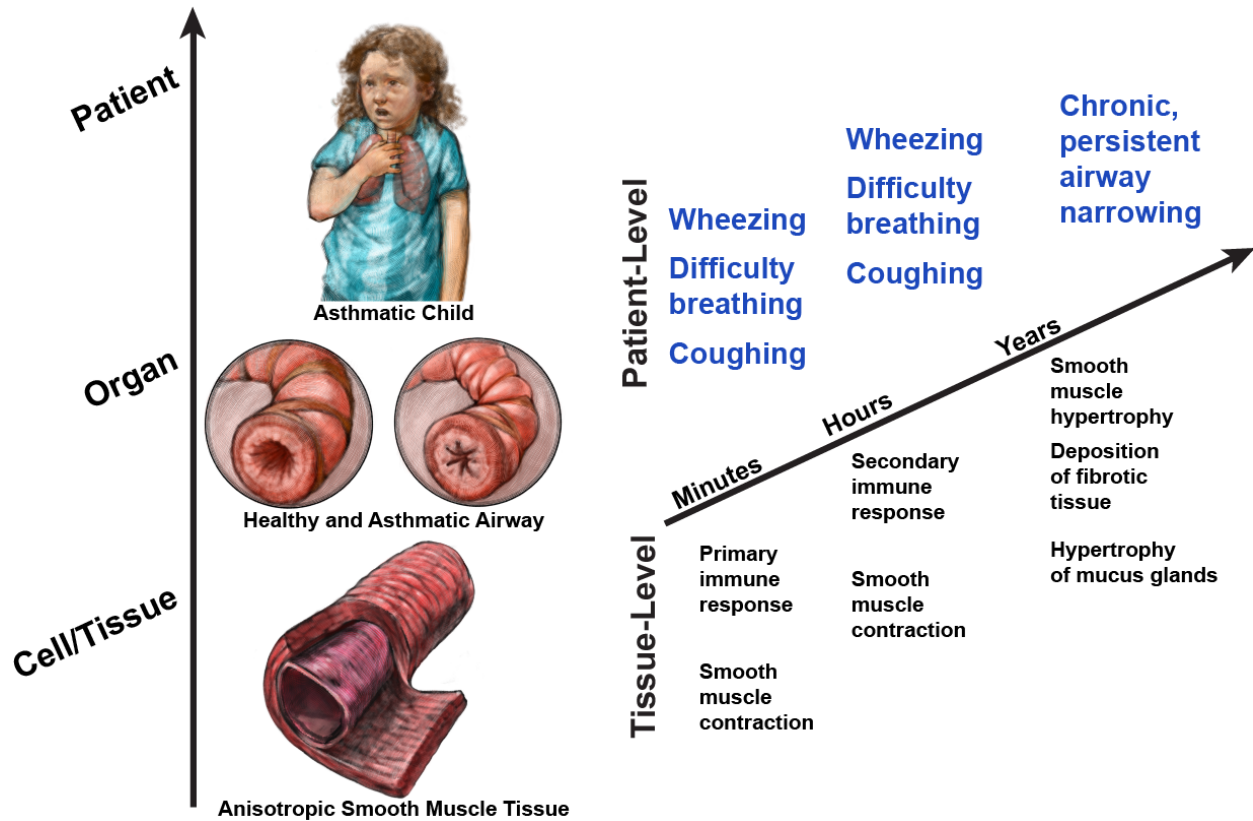
Figure 1-2. Spatiotemporal scales of smooth muscle diseases of childhood.

1.3 Engineering Human *In Vitro* Models

1.3.1 Healthy and Diseased Human Cell Sources

The development of human *in vitro* disease models relies on the availability and quality of the relevant healthy and diseased cell types (Fig.1-3). For many years, primary, patient-derived human cells have served as the only available substrate for engineering these models. While smooth muscle cells are not terminally differentiated and exhibit phenotypic plasticity[42] enabling expansion as well as *de novo* tissue formation[54-56], human skeletal muscle myoblasts, the precursor to mature skeletal muscle myofibers, have demonstrated only limited ability to fuse and form contractile muscle tissue[57, 58]. However, the development of induced pluripotent stem cells over last decade [15, 17, 33] now offers a renewable source of patient-specific muscle

progenitors that can be differentiated into muscle. Generation of induced pluripotent stem cells consists of reprogramming of mature somatic cells to an embryonic-like state through the introduction of the transcription factors Oct3/4, Sox2, c-Myc, and Klf4 [19]. Since this discovery, many protocols have been developed enabling the differentiation of specific cell types, including smooth and skeletal muscle [14, 15, 17]. Specifically, Chal et al. recently demonstrated the ability to differentiate induced pluripotent stem cells in to myofibers that exhibit sarcomeres and spontaneous contraction in culture [14, 15] through recapitulation of chemical signaling that occurs during sequential stages of paraxial mesoderm development. In addition to myofibers, their differentiation protocol generated satellite cells that associate with myofibers reminiscent of *in vivo* muscle [14, 15]. These advances provide a critical building substrate for the development of human-relevant models, although significant work remains to develop models of diseased muscle.

To this end, the development of accurate gene editing techniques has enabled introduction of diseased genotypes into the genome of healthy cells for modeling disease. In particular, programmable nucleases derived from the microbial adaptive immune system have been leveraged for targeted and efficient genome editing in mammalian cells [21]. RNA-guided endonucleases, called Cas9, can be targeted to host DNA with high specificity through predesigned guide RNA sequences[21]. There, the Cas9 endonucleases introduce double strand breaks within the host DNA[59, 60], which, in the absence of an exogenous homology repair template, can induce deletions or insertions via the native non-homologous end-joining process[61]. Hence, in conjunction with induce pluripotent stem cell technology, the ability to develop healthy and diseased genotypes of human cell types for modeling of disease now exists. These tools have been leveraged to model the mitochondrial cardiomyopathy Barth Syndrome[16] but have not yet been utilized for modeling diseases of smooth and skeletal muscle.

Human Cell Sources

Engineered Culture Conditions to Mimic Healthy and Disease Chemical Microenvironments

Recapitulation of Tissue Structure

Engineered Materials to Mimic Native ECM Stiffness and Composition

Readouts that Provide Functional, Clinically-Relevant Data
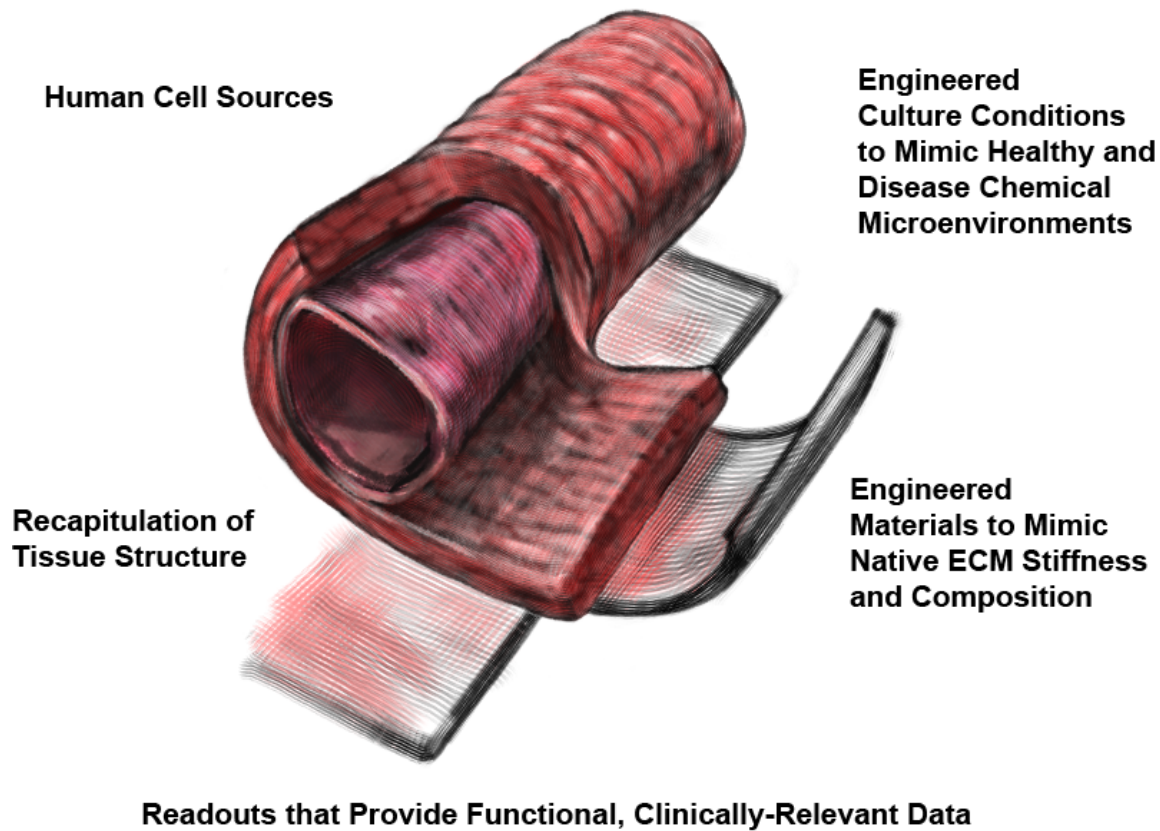
Figure 1-3. Critical components for developing accurate pediatric muscular disease models

1.3.2   Recapitulating Structure-Function Relationships in Health and Disease

The structure and function of healthy and diseased muscle is largely derived from cues provided by the local microenvironment. A number of techniques have been developed to recapitulate the structure and composition of the ECM, the mechanical cues, and the chemical cues of healthy and diseased microenvironments that in turn guide the structure and function of engineered tissues. For example, soft lithography is a widely used technique that enables high fidelity microscale patterning of ECM proteins on to a two dimensional surface[62, 63]. When muscle cells are seeded on to defined patterns of ECM proteins, the myocytes sense the boundaries of the ECM pattern and take on the shape of the pattern[62-64]. Furthermore, myocytes organize their cytoskeletal architecture with respect to their cell shape[56, 64]. Previously, McCain

et al. leveraged this technique to engineer cellular aspect ratios of cardiomyocytes on hydrogels of different elasticities to study the structure-function relationships of the heart[65]. They found that cardiomyocytes that had similar aspect ratios of those found in hypertrophic cardiomyopathy had greater stress generation on hydrogels of stiffness similar to the diseased heart compared to myocytes that had aspect ratios similar to those found in a healthy heart[65]. These findings indicate that myocytes reorganize their structure with respect to microenvironmental cues to optimize their functional performance; hence, by replicating the microenvironmental cues of health and disease, diseased structure-function relationships can be engineered *in vitro* (Fig. 1-3).

In addition, mechanical cues have been utilized to engineer healthy and diseased muscular tissues *in vitro*. In order to replicate the mechanical forces present in homeostatic conditions of mature skeletal muscle, Grossi et al. differentiated mouse myoblasts on a substrate coated with ferromagnetic beads coated with ECM proteins. The application of a magnetic field mechanically stimulated the myoblasts bound to the magnetic beads. They found that mechanical stimulation improved muscle differentiation [66]. Furthermore, the application of distinct mechanical stimuli has also been leveraged to model disease function. Gilbert et al. engineered hydrogels of stiffnesses reminiscent of healthy and fibrotic muscle and demonstrated that skeletal muscle stem cells on stiff substrates exhibited poorer self renewal compared to those on substrates of stiffness similar to healthy muscle[67]. In another study, vascular smooth muscle tissues were engineered on an elastic substrate that enabled application of large tensional forces to mimic those experienced in the vasculature during traumatic blast injury[55]. Using this technique, they found that the large tensional forces induced a phenotypic switch in the smooth muscle tissues that resulted in altered functional performance providing important insight into

blast-induced vasospasms. Hence, mechanical cues can also be utilized to direct both healthy and diseased function *in vitro.*

Lastly, the chemical microenvironment additionally plays a critical regulatory role in function of muscle tissues. Accurate temporal recapitulation of chemical growth factors is critical for successful differentiation of human skeletal muscle from pluripotent stem cells [14, 15]. Similarly, a microenvironment rich in growth factors promotes a synthetic phenotype in smooth muscle tissues; whereas, the removal of growth factors promotes a mature, contractile phenotype in smooth muscle tissues *in vitro*[42, 56]. Moreover, our group mimicked the inflammation that occurs during an acute asthma attack to promote the hypercontractility of airway smooth muscle seen in asthmatic bronchospasms[54]. A short term treatment with the asthmatic cytokine interleukin 13 caused upregulation of contractile proteins, induced reorganization of the actin cytoskeleton, and promoted hypercontractility of the smooth muscle in response to the contractile agonist acetylcholine[54]. Hence, both timing and concentration of chemical mediators within the local microenvironment can be utilized *in vitro* to direct either healthy or diseased function of muscle tissues.

1.4   Conclusions

Collectively, advances in stem cell, gene editing, materials, and organ on chip technologies have provided an opportunity to overcome many of the limitations of disease modeling in animals for improved modeling of human muscular diseases. Induced pluripotent stem cells and gene editing techniques such as CRISPR/Cas9 afford generation of healthy and diseased muscle cells that possess human genotypes. Materials engineering and microfabrication techniques enable recapitulation of native ECMs that enable extended culture of engineered muscle tissues. And lastly, exposure to homeostatic and pathologic mechanical and chemical cues can be utilized

to induce healthy and diseased structure-function relationships *in vitro.* While many of these techniques have been utilized independently to model aspects of human disease, significant work remains to be done in order to replicate the full spatiotemporal scales of human disease. In particular, long-term exposure to pathologic stimuli has not been well modeled in human *in vitro* models. Improvement in this regard is critical for improved models of human disease for development and screening of new therapies.

2   Human Airway Musculature on a Chip: An In Vitro Model of Allergic Asthmatic Bronchoconstriction and Bronchodilation

Many potential new asthma therapies that show promise in the pre-clinical stage of drug development do not demonstrate efficacy during clinical trials. One factor contributing to this problem is the lack of human-relevant models of the airway that recapitulate the tissue-level structural and functional phenotypes of asthma. Hence, we sought to build a model of a human airway musculature on a chip that simulates healthy and asthmatic bronchoconstriction and bronchodilation *in vitro* by engineering anisotropic, laminar bronchial smooth muscle tissue on elastomeric thin films. In response to a cholinergic agonist, the muscle layer contracts and induces thin film bending, which serves as an *in vitro* analogue for bronchoconstriction. To mimic asthmatic inflammation, we exposed the engineered tissues to interleukin-13, which resulted in hypercontractility and altered relaxation in response to cholinergic challenge, similar to responses observed clinically in asthmatic patients as well as in studies with animal tissue. Moreover, we reversed asthmatic hypercontraction using a muscarinic antagonist and a β-agonist which are used clinically to relax constricted airways. Importantly, we demonstrated that targeting RhoA-mediated contraction using HA1077 decreased basal tone, prevented hypercontraction, and improved relaxation of the engineered tissues exposed to IL-13. These data suggest that we can recapitulate the structural and functional hallmarks of human asthmatic musculature on a chip, including responses to drug treatments for evaluation of safety and efficacy of new drugs. Further, our airway musculature on a chip provides an important tool for enabling mechanism-based search for new therapeutic targets through the ability to evaluate engineered muscle at the levels of protein expression, tissue structure, and tissue function.

2.1 Introduction

Asthma is a leading cause of emergency department visits and hospitalization in pediatric populations [227]. In allergic asthma, the clinical symptoms of coughing, wheezing, and breathlessness result from an exaggerated increase in smooth muscle tone in response to allergen provocation of the immune system [228, 229]. Current therapeutic strategies target inflammation using glucocorticoids and excessive airway narrowing with β agonists[230]. Unfortunately, many patients remain resistant to these treatments and are at greater risk for exacerbation [181, 231, 232]. Despite this sizable clinical problem, only two new classes of airway drugs have been approved by the FDA in the last thirty years: anti-leukotrienes and anti-IgE antibodies [157]. This suggests an emergent need to accelerate the pipeline for discovery and validation of airway drugs.

Preclinical studies for therapies against diseases such as asthma are traditionally performed using animal models that may present translational challenges due to interspecies differences [233, 234]. In addition to animal models, there are several *ex vivo* and *in vitro* approaches to assess the contractility of airway smooth muscle (ASM) in response to the allergic immune response observed in asthma. Airway smooth muscle strips and rings mounted on force transducers are advantageous for studying tissue-level structure and contractility, but the assays are lower-throughput and human tissue supply is scarce [235]. In addition, magnetic twisting cytometry and traction force microscopy are effective tools for studying the effects of chemical, mechanical, and pharmacological stimuli on cellular stiffness and cellular force generation, respectively [236, 13, 14]. However, it remains unclear how to extrapolate the single cell data obtained from these studies to tissue-level structural and functional responses to drugs [237, 238]. Three dimensional ASM-fibroblast microtissues have been fabricated and exhibited basal tone, active contraction, and relaxation, but have not yet been used to model disease [239]. Hence, we

sought to develop a robust, functional, human-relevant model that can be used for screening new therapies against asthma.

We hypothesized that we could build a model of a human airway musculature on a chip that recapitulates healthy and asthmatic bronchoconstriction and bronchodilation *in vitro*. We recapitulated the simplest structural and functional unit of the human airway by engineering anisotropic human bronchial smooth muscle (BSM) lamellae and mimicked the local immune response in the asthmatic airway by exposing the engineered tissue to interleukin-13 (IL-13), a cytokine prominently found in the airway of asthmatic patients [240, 241]. IL-13 caused an increase in the expression of proteins in the RhoA/ROCK2 pathway, increased co-alignment of actin fibers within the tissue, and elicited hyperresponsiveness to acetylcholine, similar to results seen both in clinical studies and animal models. We reversed hypercontraction using standard therapies as well as a recently proposed strategy such as treatment with a rho kinase inhibitor. Lastly, we prevented hypercontraction using a rho kinase inhibitor prior to induction of contraction, demonstrating the utility of our *in vitro* model as a means for evaluating new pharmaceutical compounds, identifying disease mechanisms, and performing mechanism-based searches for therapeutics.

2.2 Results

2.2.1 Mimicking Allergic Asthma with a Human Airway on a chip

The human airway consists of anisotropic smooth muscle layers that wrap circumferentially around the lumen and contract and relax to decrease and increase its diameter, respectively (Fig. 2-1 A). To recapitulate the architecture and contraction of BSM *in vitro*, we designed an airway musculature chip that consists of human bronchial smooth muscular thin films (bMTF). bMTFs comprise a bottom layer of the elastic polymer polydimethylsiloxane

(PDMS) and a top layer of engineered BSM (Fig. 2-1 B) [242, 243]. When the muscle layer contracts, the bMTF bends reducing the radius of curvature of the tissue in the same manner that smooth muscle causes the airway to narrow. The bMTF chips were fabricated on glass coverslips by spincoating a layer of the temperature-sensitive polymer poly(N-isopropylacrylamide) (PIPAAm) within spatially defined regions, spincoating a layer of PDMS [243-247], and laser engraving arrays of cantilevers [247] (Fig. 2-1 B, 2-2). Using microcontact printing, a fibronectin pattern of 15 μm wide lines with 2 μm spaces was transferred to the PDMS substrate to enable cellular adhesion and anisotropic tissue formation (SM). Normal human primary BSM cells in growth medium were then seeded on to the micropatterned lines, promoting self-assembly of anisotropic monolayers that recapitulate the lamellar muscle architecture of the airway.
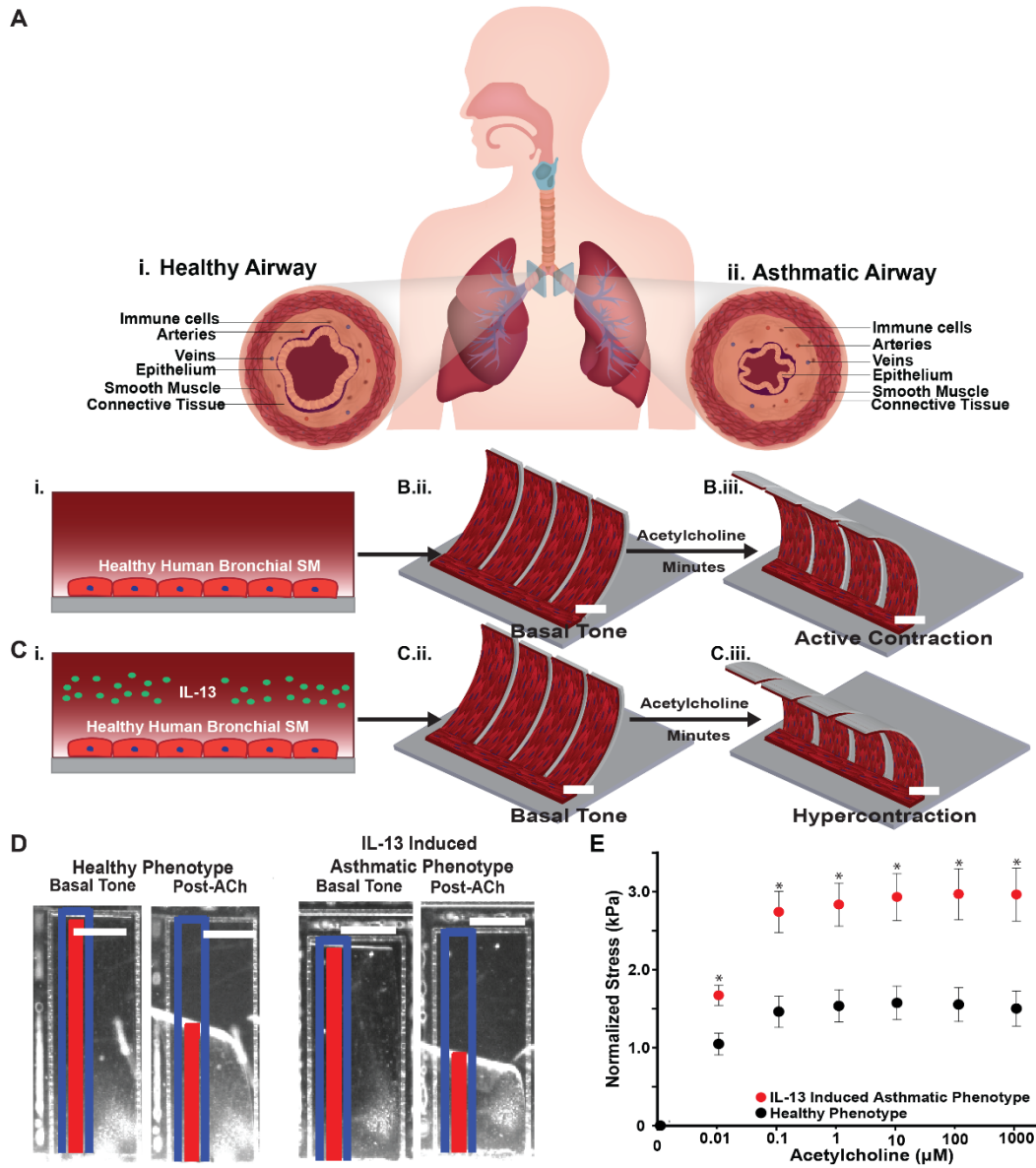
Figure 2-1. Design, build, test: airway musculature on a chip.

(A) Schematic of the healthy and asthmatic airway. Anisotropic, muscular lamellae wrap around the human airway to control airway tone. (i) The healthy airway is characterized by few immune cells and a patent airway. (ii) The asthmatic airway is characterized by influx of immune cells, structural remodeling, and a constricted airway. (B) Schematic depicting acetylcholine-induced

(continued) contraction of healthy bMTF chip. (i) The healthy airway was recapitulated by engineering anisotropic, muscular lamella on thin films. (ii) The bMTFs are peeled and assumed a basal tone. (iii) Active contraction is induced by administering acetylcholine (ACh). Scale bar represents 2 mm. (C) Schematic depicting ACh-induced contraction of asthmatic bMTF chip. (i) The asthmatic airway was recapitulated by administering interleukin 13 (IL-13) to the engineered BSM (BSM) during culture. (ii) The asthmatic bMTFs are peeled and assume a basal tone. (iii) Active contraction is induced by administering ACh. Scale bar represents 2 mm. (D) Representative images of bMTFs at basal tone and post-ACh administration. Scale bar represents 1 mm. The blue outline and red tracker represent the original length and horizontal projection of the film, respectively. (E) Stress is plotted against ACh concentration (10 nM to 1 mM) and measured from the initial basal tone. n=15 films, 3 chips for the healthy phenotype; n=23 films, 4 chips for the IL-13 induced asthmatic phenotype. Data points represent mean +/- standard error. * indicates $p < 0.05$ at a given dose of ACh.
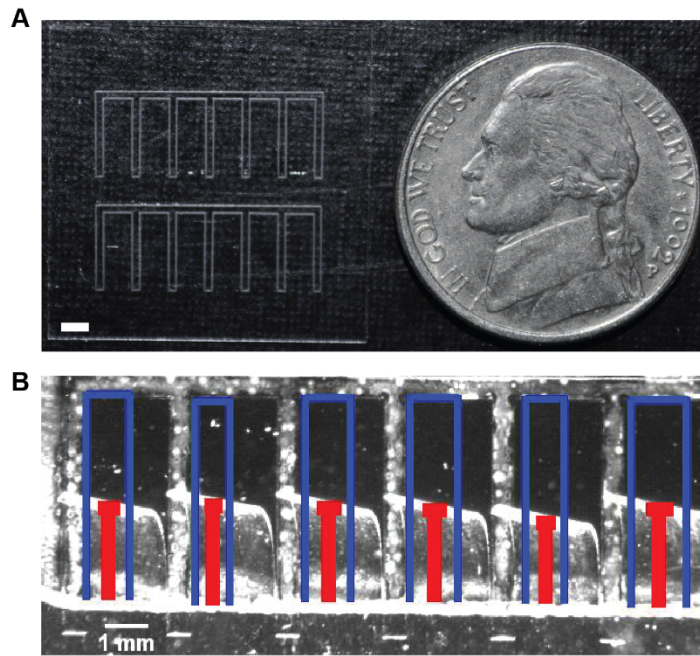
Figure 2-2. Representative airway chip.

(A) Example airway on a chip substrate prior to cell seeding. The glass cover slip is 22 x 22 mm. The films are 5 mm long and 2 mm wide. Scale bar represents 2 mm. **(B)** Representative contractile stress experiment. The blue region enables thresholding for tracking of the film edge and is equal in length to the unpeeled film. The red line tracks the projection of the film and is used for calculating the radius of curvature of the film. Scale bar represents 1 mm.

IL-13 is a cytokine prominently found in the airway of asthmatic patients and is known to contribute to increased constriction of the airway as well as structural remodeling[181]. To induce an allergic asthma phenotype in our engineered BSM, growth medium was replaced with serum-free medium to induce the switch to a physiological, contractile phenotype for 24 hours. Next, IL-13 was administered to the anisotropic, laminar BSM for an additional 10-14 hours (Fig. 2-1

C). When tissue was ready for experiments, the bMTF chip was transferred to Tyrode's solution and the bMTFs were peeled from the substrate. The temperature was briefly dropped below 32°C to allow PIPAAm to dissolve and to leave a freestanding, cantilevered film. The film assumed an initial curvature corresponding to the basal tone within the tissue (Fig. 2-1 B-C). Active contraction of the BSM was induced by directly adding the cholinergic agonist acetylcholine, which is natively secreted from autonomic innervation of the bronchi, causing the film to curl further over a time scale of minutes (Fig. 2-1 B-C). Tissue stresses were derived from observing the extent of bMTF bending and hence our chip provides quantitative measurements of basal tone and active contraction in engineered human tissue.

We asked if we could mimic an allergic bronchoconstriction on our chip. Clinically, airway hypersensitivity and hyperresponsiveness are assessed using spirometry, where the maximal forced expiratory volume (FEV) and the forced expiratory volume in one second (FEV1) are measured [183, 248]. In this diagnostic test, bronchoconstriction is elicited using a cholinergic agonist and changes in the FEV and FEV1 are measured as a result of the smooth muscle contraction and subsequent airway narrowing. Asthmatic patients experience a significant decrease in their FEV1 compared to healthy patients[249], suggesting excessive airway narrowing due to BSM contraction leading to coughing and wheezing. To test whether we could mimic allergic asthma bronchoconstriction *in vitro*, we simulated this diagnostic test by quantifying the contractile stresses of bMTFs in response to increasing concentrations of the bronchoconstrictor acetylcholine. Contraction of tissues was elicited by cumulatively dosing acetylcholine from 10 nM to 1 mM with ten minute dosing intervals (Fig. 2-1 D). Prior to constriction, the basal tone of healthy and asthmatic phenotypes was not statistically different, a result that may be clinically analogous to the normal specific airway resistance seen in asthmatic

children [250]. All stress values were quantified as the difference from the basal tone, denoted as normalized stress (Fig. 2-1 E). The tissues exposed to IL-13 generated greater stress at each dose of acetylcholine (10 nM-1 mM) when compared to healthy phenotype at the same dose (Fig. 2-1 E). This increased contractile response in our IL-13 induced asthmatic phenotype is reminiscent of the reduction of FEV1 seen in spirometry studies of human asthmatic patients [249, 251] and corresponds with elevated agonist-induced increases in cellular stiffness in human and rabbit airway smooth muscle measured with atomic force microscopy and magnetic twisting cytometry[106, 252]. These data suggest IL-13 exposure does not increase the basal tone, but induces hypercontraction of human BSM in response to acetylcholine. Thus, bMTFs model a hallmark pathological feature of asthma related to hypercontraction of BSM.

2.2.2 Physiological and impaired relaxation in asthma

Clinically, asthma is distinguished from other obstructive airway diseases by the reversibility of airway obstruction in response to β-agonists [253], such as albuterol and isoproterenol, which induce relaxation by reducing intracellular calcium through production of cyclic adenosine monophosphate (cAMP) [254]. We asked if we could recapitulate these responses in our airway on a chip model. Healthy and IL-13 treated bMTFs were peeled and assumed a basal tone (Fig. 2-3 A-B). Next, 100 μM isoproterenol and 1 mM isoproterenol doses were administered to the tissues in order to induce relaxation. The IL-13 induced asthmatic phenotype had a greater magnitude of relaxation in response to 1 mM isoproterenol compared to the healthy phenotype, indicating IL-13 alone does not cause impaired relaxation of human BSM although it has been shown to reduce the ISO-induced reduction of cell stiffness[117]. This result is reminiscent of greater increases in pulmonary function in response to dosing with a β-agonist seen in asthmatic patients compared to control groups [255, 256].
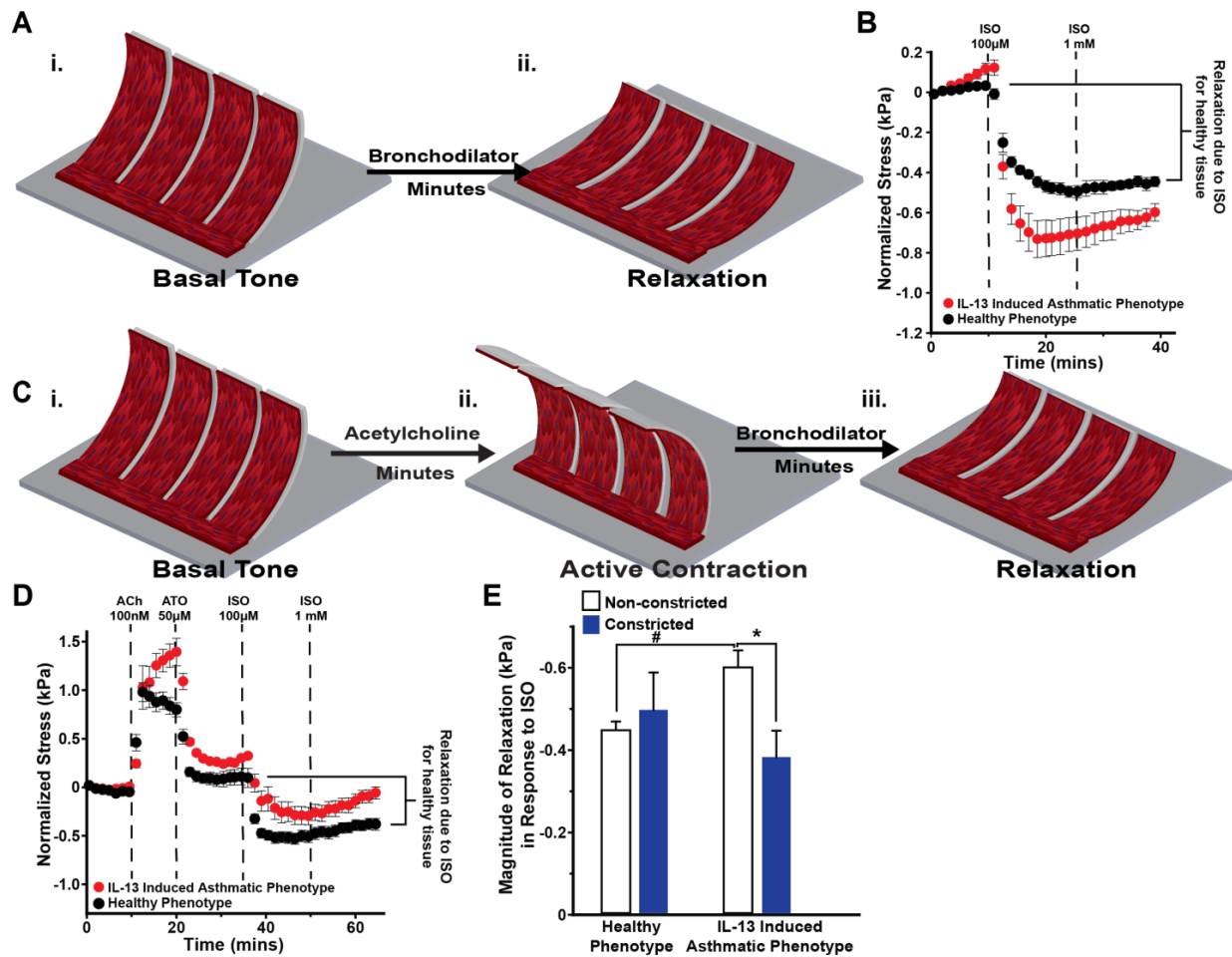
Figure 2-3. Impaired relaxation due to synergistic effect of IL-13 and ACh.

(A) Schematic depicting (i) the basal tone and (2) bronchodilator-induced relaxation of bMTF chip. (B) Relaxation was quantified in response to the β-agonist isoproterenol (ISO). Stress is measured from the basal tone. n=12 films, 2 chips for the healthy phenotype; n=10 films, 2 chips for the IL-13 induced asthmatic phenotype. Data points represent mean ± standard error. (C) Schematic depicting (i) basal tone (ii) preconstriction and (iii) bronchodilator-induced relaxation of airway on a chip after initially constricting the tissue. (D) Tissues were constricted using ACh then subsequently treated with ATO 50 μM, ISO 100 μM, and ISO 1 mM in series to induce relaxation. Stress is measured from the basal tone. n=11 films for the healthy phenotype, 2 chips; n=12 films, 2 chips for the IL-13 induced asthmatic phenotype. Data points represent mean ±

standard error. **(continued)** (E) The magnitude of relaxation in response to ISO was quantified for non-constricted tissues (dark gray) and constricted tissues (black). For non-constricted tissues, the change in stress was measured between the basal tone and the tone after administration of 1 mM ISO (seen in the stress traces in Fig. 2B). For constricted tissues, the change in stress was measured between the tone after administration of 50 µM ATO and the tone after administration of 1 mM ISO (seen in the stress traces in fig. 2D). * and # indicate p<0.05.

Despite the clinical success of β-agonists and glucocorticoids in the majority of asthma patients, 5% to 10% are non-responsive to these therapies and are at a greater risk for hospitalization [156, 232]. Previous work in animals has shown functional antagonism between cholinergic-induced contraction and β-agonist-induced relaxation [257, 258]. We sought to determine if one reason for impaired BSM relaxation in therapy-resistant patients is exposure to specific cytokines and subsequent triggering of intracellular signaling by acetylcholine as IL-13 has been shown to reduce ISO induced relaxation in acetylcholine-preconstricted rabbit airway smooth muscle[252]. To determine the effect of acetylcholine on isoproterenol-induced relaxation in our engineered human tissues, we constricted tissues with acetylcholine prior to inducing relaxation and compared this response to tissues that were relaxed from their basal tone. We peeled the healthy and IL-13 treated bMTFs, allowing them to assume a basal tone (Fig. 2-3 C), and then constricted the tissues using 100 nM acetylcholine. Next, the muscarinic antagonist and bronchodilator atropine was administered to prevent any further contraction due to acetylcholine binding to muscarinic receptors, as well as to induce relaxation to a stress level near the initial basal tone (Fig. 2-3 C). Further relaxation was induced using 100 µM and 1 mM isoproterenol, and the magnitude of relaxation was quantified by calculating the difference of stress after the 1

mM isoproterenol dosing interval and the 50 µM atropine dosing interval (Fig. 2-3 D). The healthy phenotypic tissues constricted with acetylcholine prior to induction of relaxation with isoproterenol did not have a statistically different magnitude of relaxation compared to the healthy phenotype that had not been constricted prior to induction of relaxation (Fig. 2-3 E). However, the IL-13 induced asthmatic phenotypic tissues constricted prior to induction of relaxation had a significant decrease in the magnitude of relaxation in response to isoproterenol compared to the IL-13 induced asthmatic phenotypic tissues that had not been constricted prior to induction of relaxation (Fig. 2-3 E). These data suggest IL-13 and acetylcholine may act synergistically on the same pathway to disrupt relaxation of human BSM.

2.2.3   Effect of IL-13 on structure and protein expression

Thickening of BSM in the airway wall is a structural hallmark of asthma[186, 259] and potentiates airway narrowing. We asked whether IL-13 induced cellular hypertrophy of human BSM in our system. To test this hypothesis, we stained the actin cytoskeleton and nuclei in confluent tissues after culture and treatment with either IL-13 or vehicle (Fig. 2-4 A). We then determined the number of cells per field of view as a measure of average cell under the assumption of confluence (Fig. 2-4 B). The healthy phenotype had a statistically larger number of cells per field of view compared to tissue exposed to IL-13. These results suggest that IL-13 caused increased cellular size of human BSM. This result is similar to the cellular hypertrophy observed in the peripheral airways of asthmatic patients [260].
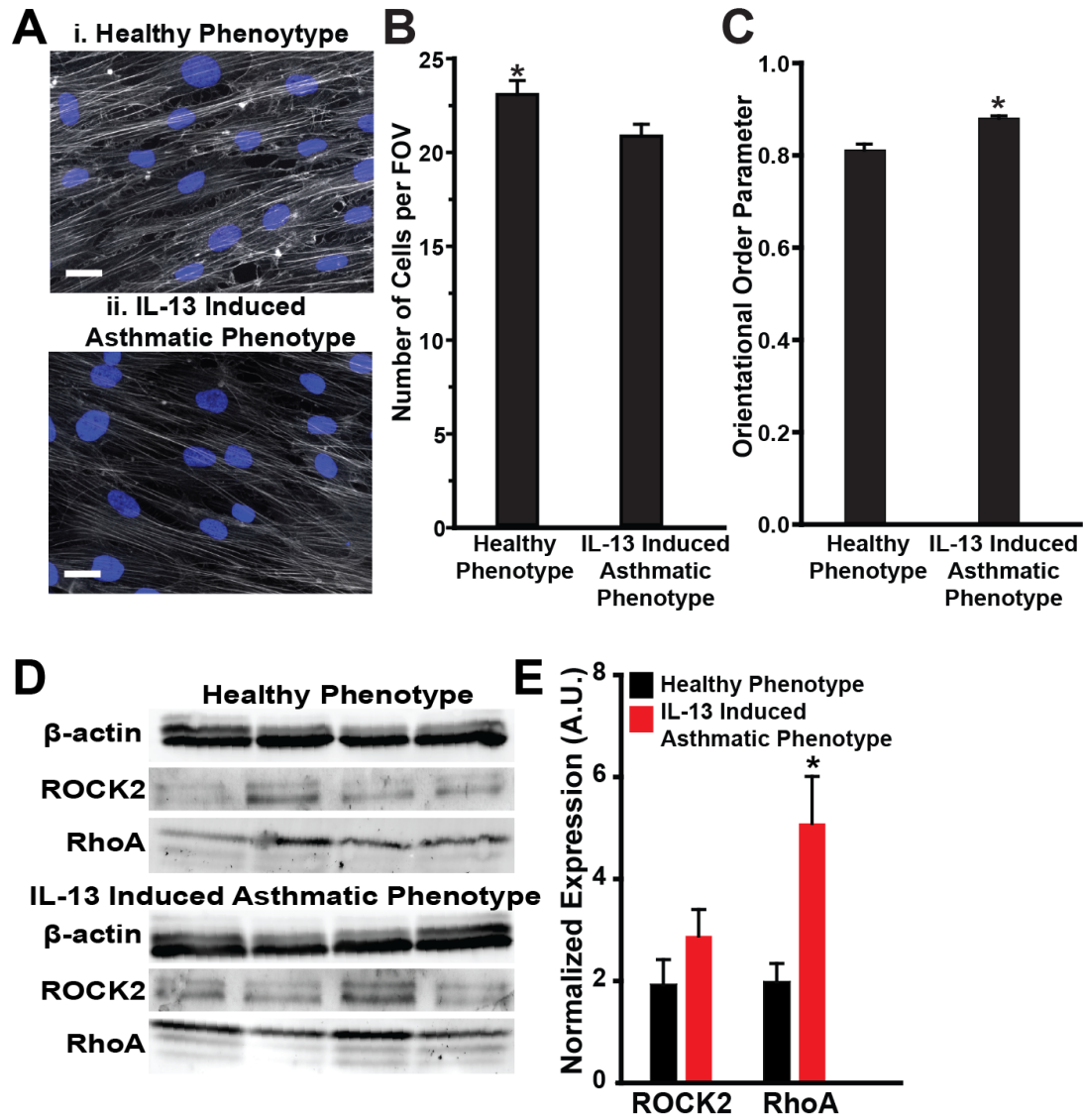
Figure 2-4. Structural and protein expression changes due to IL-13.

(A) Representative (i) healthy and (ii) IL-13 exposed engineered BSM tissues immunostained for f-actin (gray) and nuclei (blue). Scale bar is 25 μm. **(B)** The average number of cells per field of view (222 μm by 166 μm) was quantified with the assumption each cell had a single nucleus. Mean ± standard error, n=5 chips, for healthy and the IL-13 induced asthmatic phenotypes, 10 fields of view per sample, * indicates p<0.05. **(C)** The actin orientational order parameter (OOP) is plotted for each condition. Mean ± standard error, n=5 chips, 10 fields of view per sample for healthy and the IL-13 induced asthmatic phenotypes, * indicates p<0.05. **(D)** Western blot gel

using β-actin as **(continued)** a control for total protein expression. **(E)** Normalized protein expression, measured by Western blot, for ROCK2 and RhoA. Mean ± standard error, n=4 tissues for each condition, * indicates p<0.05.

We also asked if IL-13 altered contraction by modifying the organization of the actin cytoskeleton. In the human airway, actin cytoskeletal fibers orient in parallel to the longitudinal axis of the BSM cells [261], which wrap circumferentially around the airway [262, 263]. To investigate tissue architecture, we measured actin orientation angles using an algorithm based on fingerprint identification [264] and quantified their global alignment by calculating the orientational order parameter (OOP), where 1 represents perfect alignment and 0 represents random organization [265] (Fig. 2-4 C). Both healthy and IL-13 induced asthmatic phenotypes had high values of OOP, suggesting highly aligned tissues, reminiscent of BSM in human airway [262, 263]. The IL-13 induced asthmatic phenotype had a greater OOP than the healthy phenotype, indicating IL-13 induced increased alignment of actin fibers. Together, these results mimic changes of the cellular architecture seen in the culture of hypercontractile BSM in previous reports [266] and post mortem tissue [267].

Next, we asked whether IL-13 altered expression of proteins that regulate contraction in bronchial smooth muscle. Expression of α-smooth muscle actin and smooth muscle myosin heavy chain are thought to be indicative of the contractile phenotype of airway smooth muscle [268]. To determine whether a phenotypic switch contributed to hypercontraction of the tissues exposed to IL-13 in our system, we used Western blot to determine the normalized expression of α-smooth muscle actin in the IL-13 induced asthmatic and healthy phenotypes. The contractile phenotype was supported by observation of diffuse expression of α-smooth muscle actin in

immunostained images (Fig. 2-5 A), but there was no statistical difference between protein expression in the healthy and asthmatic conditions (Fig. 2-5 B). Upregulation of the RhoA/ROCK pathway has been implicated as a key player in augmented bronchoconstriction in asthma [118, 130]. Here, we asked if the RhoA/ROCK pathway acts as an effector of hypercontraction of BSM in human asthma. We used Western blot to determine the normalized expression of RhoA and ROCK2 relative to β actin (Fig. 2-4 D). IL-13 induced statistically greater expression of RhoA in the IL-13 induced asthmatic phenotype compared to the healthy phenotype (Fig. 2-4 E), similar to previous reports [117, 118]. Additionally, there was increased expression of ROCK2, a downstream effector of RhoA in the IL-13 induced asthmatic phenotype, but this result was not found to be statistically significant. These results suggest that the hypercontraction of the IL-13 induced asthmatic phenotype observed in our system may be induced through upregulation of RhoA.

A

Healthy Tissue | IL-13 Exposed Tissue

B

β-actin

α-SM actin

Healthy Tissue | IL-13 Exposed Tissue
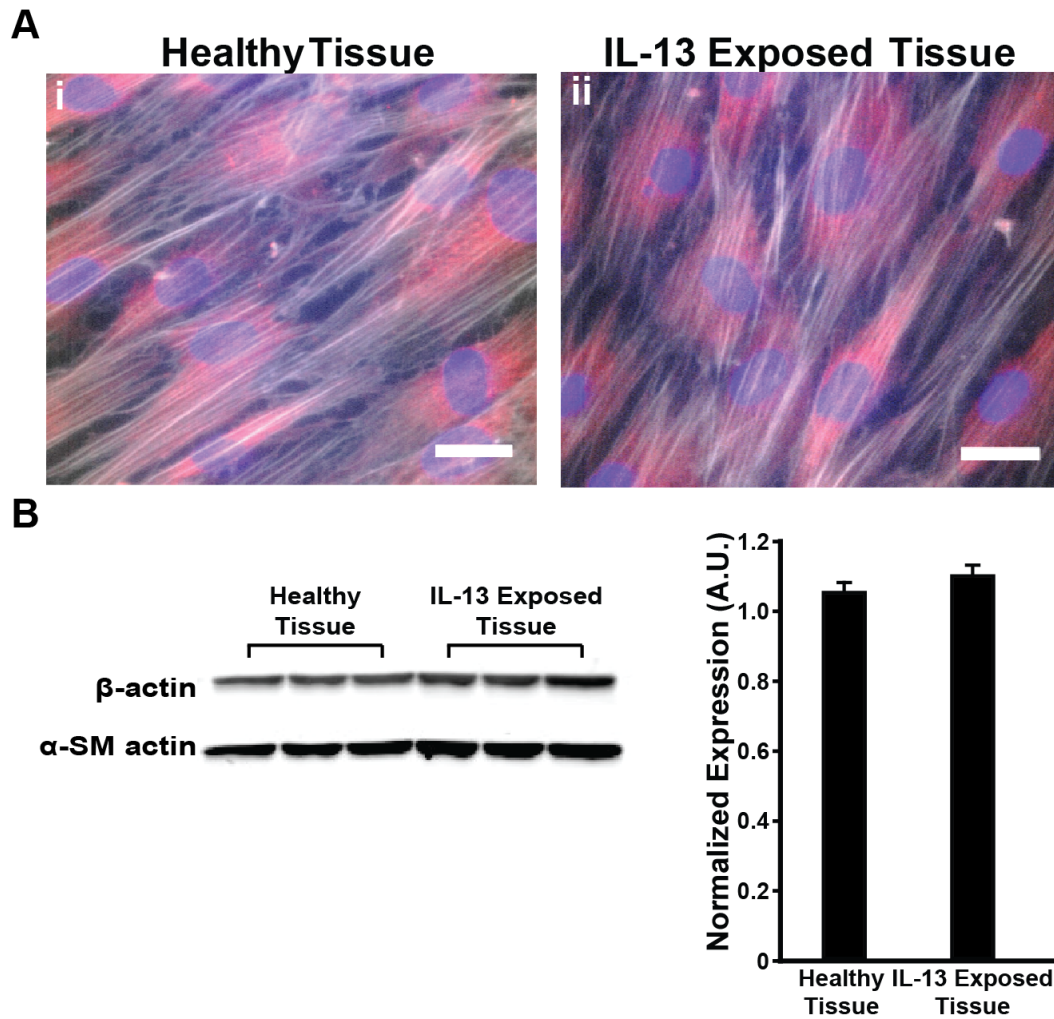
Figure 2-5. Bronchial smooth muscle phenotype.

(A) Example tissues immunostained for f-actin (white) to detect the actin cytoskeleton, α-smooth muscle actin (red) to identify muscular phenotype, and nuclei (blue). Scale bar is 25 μm. **(B)** Western blot gel using β-actin as a control for total protein expression. Normalized protein expression, measured by Western blot, for α-smooth muscle actin. Mean ± standard error, n=3 tissues for each condition, no statistical significance.

2.2.4   Regulation of hypercontraction and impaired relaxation by ROCK

The contractile strength of smooth muscle is dependent on the intracellular concentration of calcium and calcium sensitization mediated through RhoA [170]. Since we observed that IL-13-induced upregulation of RhoA, we asked if pretreatment with HA1077, an inhibitor of Rho-mediated calcium sensitization and contraction, would prevent hypercontraction as seen in IL-13-treated mouse BSM[118] and ovalbumin-sensitized guinea pigs [269]. To test this hypothesis, we pretreated the IL-13 induced asthmatic phenotype with 10 μM HA1077 for fifteen minutes in serum-free culture media and washed the drug out with PBS thirty minutes prior to initiation of the acetylcholine dose response. The IL-13 induced asthmatic phenotypic tissues that were pretreated with HA1077 exhibited a statistically lower basal tone than both the healthy phenotype and untreated, IL-13 induced asthmatic phenotype (Fig. 2-6 A). HA1077-pretreated, IL-13 induced asthmatic phenotypic tissues additionally exhibited statistically lower stresses than both the healthy and untreated IL-13 induced asthmatic phenotypic tissues up to 1 μM acetylcholine (Fig. 2-6 A). For the doses of 10 μM to 1 mM acetylcholine, HA1077-pretreated tissues exposed to IL-13 did not have statistically different stresses compared to the healthy phenotype, but did have statistically lower stress compared to untreated tissues exposed to IL-13 (Fig. 2-6 A). This result indicates HA1077 decreases the basal tone of our engineered BSM tissue and prevents hypercontraction.
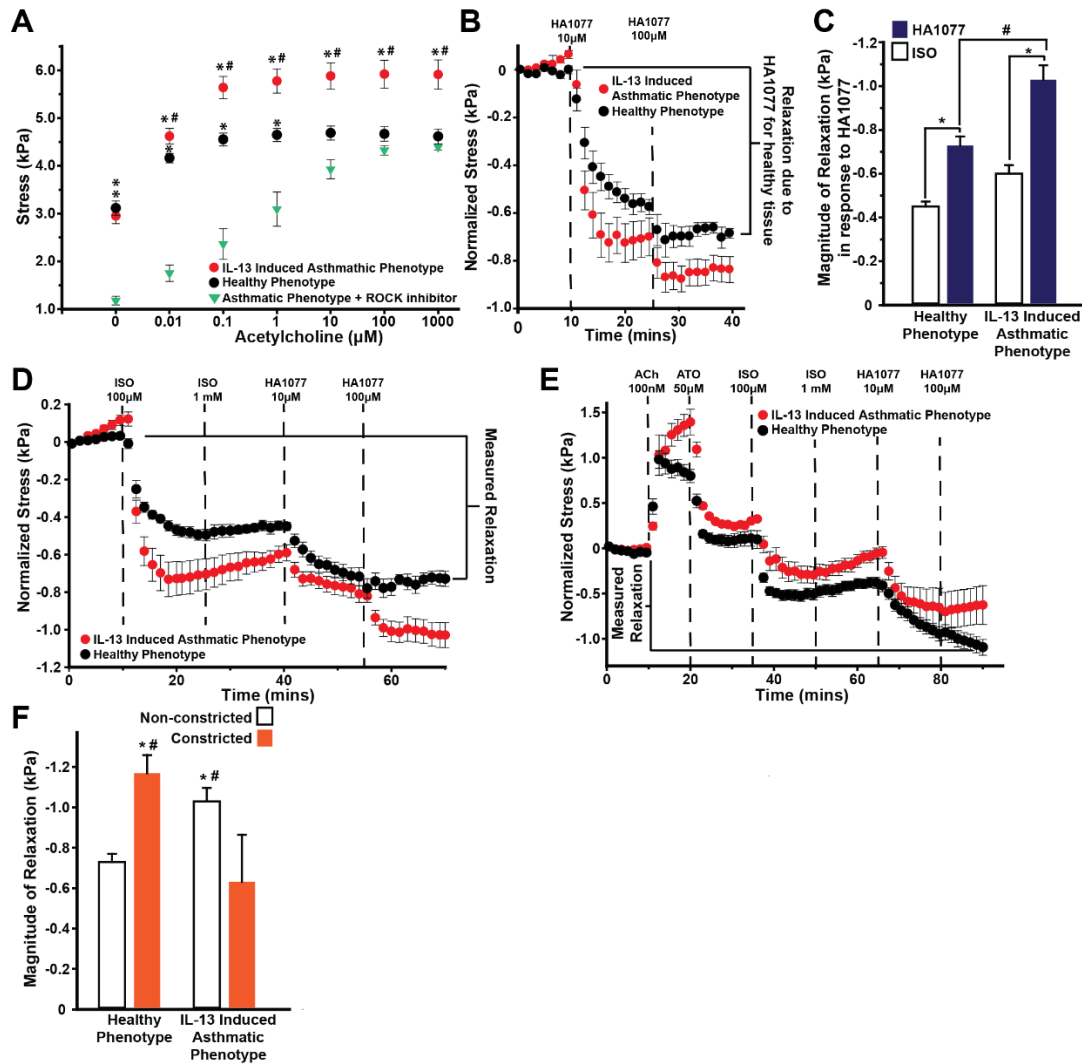
Figure 2-6. Regulation of hypercontraction via the RhoA/ROCK2 pathway.

(A) The contractile response of the IL-13 induced asthmatic phenotype pretreated with 10 μM HA1077. n=15 films, 3 chips for the healthy phenotype; 4 chips, n=23 films for the IL-13 induced asthmatic phenotype; n=12 films, 2 chips for IL-13 tissue pretreated with HA1077. Data points represent mean ± standard error. The ACh dose response was plotted versus concentration denoting statistical significance at each dose, * indicates p<0.05 relative to IL-13 tissue pretreated with HA1077 and # indicates p<0.05 relative to both healthy phenotypic tissues and the IL-13 induced asthmatic phenotypic tissues pretreated with HA1077. **(B)** For the healthy and the IL-13 induced asthmatic phenotypes, relaxation was quantified in response to HA1077.

Stress is **(continued)** measured from the basal tone. n=12 films for the healthy phenotype, 2 chips; n=12 films, 2 chips for the IL-13 induced asthmatic phenotype. Data points represent mean ± standard error. **(C)** The magnitude of relaxation in response to HA1077 was quantified measuring the change in stress between the basal tone and the tone after the administration of 100 μM HA1077. This response was compared to the relaxation induced in response to 1mM ISO seen in Fig. 2B. * and # indicate p<0.05. **(D)** Healthy and the IL-13 induced asthmatic phenotypes were relaxed from the basal tone using ISO and HA1077 in series. Stress is measured from the basal tone. n=10 films, 2 chips for the healthy phenotype; n=11 films, 2 chips for the IL-13 induced asthmatic phenotype. Data points represent mean ± standard error. **(E)** Tissues were constricted using ACh, then relaxed using ATO, ISO, and HA1077 in series. Stress is measured from the basal tone. n=11 films for the healthy phenotype, 2 chips; n=12 films, 2 chips for the IL-13 induced asthmatic phenotype. Data points represent mean ± standard error. **(F)** The relaxation was quantified by measuring the change in stress between the basal tone and the tone after administration of 100 μM HA1077. * indicates p<0.05 between non-constricted and constricted tissues within a condition. # indicates p<0.05 of the non-constricted/constricted tissues between the healthy and IL-13 conditions.

Next, we asked whether inhibiting rho kinase would also be effective for inducing relaxation. Similar to the relaxation studies performed using isoproterenol, we peeled the bMTFs, allowed them to assume a basal tone, and then induced relaxation with 10 μM and 100 μM HA1077 (Fig. 2-6 B). Similar to the results of the isoproterenol-induced relaxation without prior constriction (Fig. 2-6 B), HA1077 induced a statistically greater relaxation of the IL-13 induced asthmatic phenotype compared to the healthy phenotype (Fig. 2-6 C). Additionally, we compared

the efficacy of 100 μM HA1077 to the efficacy of 1 mM isoproterenol (Fig. 2-6 C). For both healthy and the IL-13 induced asthmatic phenotypes, HA1077 elicited a statistically greater relaxation compared to the isoproterenol-induced relaxation.

Because isoproterenol and HA1077 induce relaxation via different mechanisms, we asked whether using both drugs together would have additive effects. To test this hypothesis, we administered 100 μM isoproterenol, 1 mM isoproterenol, 10 μM HA1077, and 100 μM HA1077 at fifteen minute intervals and measured the decrease in stress relative to the basal tone (Fig. 2-6 D). Additionally, we tested the additive effects of isoproterenol and HA1077 of healthy and the IL-13 induced asthmatic phenotypes that had been constricted with acetylcholine prior to inducing relaxation (Fig. 2-6 E). The magnitude of relaxation was measured as the difference of stress after the 100 μM HA1077 dosing interval and the basal tone (Fig. 2-6 E). In non-constricted tissues, we found the serial dosing of isoproterenol and HA1077 induced significantly greater relaxation in the IL-13 induced asthmatic phenotype compared to the healthy phenotype (Fig. 2-6 D, F). However, in constricted tissues, the IL-13 induced asthmatic phenotype had significantly less relaxation compared to the healthy phenotype (Fig. 2-6 E-F). The constricted, IL-13 induced asthmatic phenotype also had significantly less relaxation compared to non-constricted, IL-13 induced asthmatic phenotype, while the constricted, healthy phenotype relaxed significantly more than the non-constricted, healthy phenotype (Fig. 2-6 D-F). These data indicate IL-13 and acetylcholine act synergistically to alter the ability of asthmatic human BSM to relax. Lastly, we found using both isoproterenol and HA1077 improved relaxation compared to tissues relaxed with isoproterenol alone, suggesting that rho kinase inhibitors represent a new class of therapeutics for patients who are resistant to current asthma therapies.

2.3 Discussion

The challenge of organ on chips is to recapitulate healthy and diseased physiology of multiple tissue or organ mimics that communicate *in vitro* in order to supplement animals in preclinical drug development [270]. Developing platforms that allow for acquisition of robust, reliable tissue or organ-level structural and functional outputs while maintaining the simplicity requisite for high throughput fabrication is an immense challenge. In this study, we designed, built, and tested an *in vitro* model of healthy and asthmatic human airway musculature. On our human airway musculature chip, we demonstrated that we could recapitulate many of the hallmark clinical features of asthmatic airway smooth muscle: hyperresponsiveness to acetylcholine, physiological and impaired relaxation in distinct experiments, cellular remodeling, and increased expression of contractile proteins. We tested our system using standard airway drugs and observed appropriate functional responses to β-agonists and muscarinic antagonists. Further, we demonstrated the efficacy of HA1077 in prevention of ACh triggered hypercontraction of IL-13 treated tissues and relaxing the muscle from its basal tone and after contraction as well as showed that HA1077 had an additive effect with isoproterenol in inducing relaxation of human airway musculature.

Reversible airway narrowing in asthma elicits the clinical symptoms of breathlessness, wheezing, and coughing [228, 248]. In asthma, the BSM is hyperresponsive to a number of nonspecific stimuli such as tobacco smoke [271], air pollution [272], cleaning agents [273], and drugs such as non-steroidal anti-inflammatories [274]. Clinically, hyperresponsiveness is assessed using spirometry after exposing the airway to the cholinergic agonist methacholine[249]. In this study, the IL-13 induced asthmatic phenotype did not have statistically different basal tone compared to the healthy phenotype but generated greater contractile stress in response to doses of 10 nM to 1 mM

of acetylcholine, potentially explaining why asthmatic patients have increased reductions in FEV1 measurements compared to healthy patients [249]. These results indicate that IL-13 does not increase human BSM tone alone but instead acts synergistically with acetylcholine to cause hypercontraction. This result may explain why using the synthetic muscarinic antagonist ipratropium bromide as an adjunct to β agonists has successfully reduced asthmatic exacerbation rates in asthma patients[275].

Episodes of excessive airway narrowing are typically managed using β agonists [275]. Here, we tested the relaxation capability of healthy and the IL-13 induced asthmatic phenotypes using the β agonist isoproterenol. First, the tissues were relaxed from their basal tone, and the IL-13 induced asthmatic phenotype achieved a greater magnitude of relaxation compared to the healthy phenotype. This result suggests that IL-13 alone does not alter the relaxation response of bronchial smooth muscle. However, when we tested relaxation after acetylcholine-induced constriction, the constricted, IL-13 induced asthmatic phenotype had significantly less relaxation compared to the IL-13 induced asthmatic phenotype that had not been constricted. The same effect was not observed in constricted healthy phenotypic tissues. Together, these results indicate that synergism occurs between IL-13 and acetylcholine to alter the relaxation response to isoproterenol. Similar functional antagonism between cholinergic-induced contraction and β agonist-induced relaxation has been observed in canine and guinea pig airway smooth muscle [257, 258], which may be due to inhibition of β agonist-induced cAMP production [276]. Here, the impaired relaxation may manifest when both acetylcholine disables cAMP regulation of intracellular calcium and IL-13 upregulation of the Rho/ROCK pathway, consequently causing increased intracellular calcium and increased calcium sensitivity.

Structural remodeling is an additional clinical hallmark of the asthmatic human airway[186, 259]. Further, the severity of asthma is related to the extent of airway remodeling [186]. In this study, we found that IL-13 caused increased cellular size within the tissue. Additionally, an increased alignment of actin fibers within tissue treated with IL-13 was observed. Many studies provide evidence indicating that phosphorylation of myosin light chain and remodeling of the actin cytoskeleton possess independent roles in the contraction of smooth muscle [277], where maximum stress generation may be dependent both on length of actin fibers and myosin light chain phosphorylation. Thus, the structural remodeling of BSM cells may play an important role in hypercontraction in asthma.

Protein expression is commonly used to assess the phenotype of smooth muscle in disease. Expression of α-smooth muscle actin and smooth muscle myosin heavy chain are thought to be indicative of a contractile phenotype of airway smooth muscle [268]. Increased expression of RhoA and coupling to ROCK has been associated with diseases involving hypercontraction of smooth muscle like subarachnoid hemorrhage induced vasospasm and asthma [130]. In this study, the increased expression of RhoA in the IL-13 induced asthmatic phenotype was consistent with pathologically hypercontractile smooth muscle tissue.

Lastly, we evaluated newly proposed treatment strategies, specifically HA1077, as a treatment for preventing hypercontraction of human BSM as well as a treatment for acute bronchoconstriction. Pretreatment of the IL-13 induced asthmatic phenotype with HA1077 caused decreased basal tone compared to both healthy and the non-treated, IL-13 induced asthmatic phenotype. Further, this treatment lowered the maximal contractile response of the IL-13 induced asthmatic phenotype, suggesting that upregulation of the Rho/ROCK pathway plays a critical role in hypercontraction of human bronchial smooth muscle. We found that HA1077

induced greater relaxation in both healthy and IL-13 tissues than isoproterenol. Because isoproterenol and HA1077 act on regulation of intracellular calcium and calcium sensitivity, respectively, we tested the additive effects of relaxing both non-constricted and constricted tissues. This resulted in greater relaxation in constricted healthy phenotypic tissues relative to non-constricted healthy phenotypic tissues, while prior constriction reduced the ability of the IL-13 induced asthmatic phenotypes compared to the non-constricted, IL-13 induced asthmatic phenotype. This demonstrates synergism between acetylcholine and IL-13 in altering relaxation capacity. Importantly, it was additionally demonstrated that isoproterenol and HA1077 together induce greater relaxation compared to isoproterenol, the current standard treatment.

Human organs on chips are of interest because of their promising potential to replace *in vivo* animal studies due to improved specificity, sensitivity, and predictiveness[33]. Our work represents the next stage of development where we build more fidelity into our system by mimicking disease. This is important for drug safety and efficacy testing and disease modeling as well as mechanism-based search for therapeutics. Further, the airway musculature on a chip is amenable to integration into microfluidic system which will enable coupling with other healthy and diseased organ mimics.

2.4   Material and Methods

2.4.1   Chip Fabrication

Glass coverslips (22 mm X 22 mm, VWR, Westbury NY, catalog# 48366-067) were cleaned in 70% ethanol via sonication for thirty minutes and subsequently air dried. A piece of low adhesion Scotch tape (3M, St. Paul, MN) was applied to cover the entire surface of the glass coverslip. Two rectangles with rounded corners with dimensions of 13 mm X 5.5 mm were laser engraved into the tape using a CO_2 laser (VersaLaser 2.0, 10.6 μm wavelength, 10 W, Universal

Laser systems, Scottsdale, AZ) using 10% power and 2% speed settings [247]. The rectangles were then peeled from the coverslip while leaving the remaining surface covered by the tape. A thin layer of poly(N-isopropylacrylamide) (PIPAAm) (Polysciences, Warrington, PA) dissolved in1-butanol (10% w/v) was spin coated at a maximum speed of 6000 RPM for one minute onto the exposed areas of the coverslip in order to serve as a sacrificial layer. After removing the remaining tape, Polydimethylsiloxane (PDMS) (Sylgard 184, Dow Corning, Midland, MI) was mixed at a 10:1 base to curing agent ratio and spin coated at a maximum speed of 4000 RPM for one minute so that a thin layer of PDMS coated both the uncoated and PIPAAm-coated regions of the coverslip. After curing of the PDMS layer over night at 65°C, two rows of six cantilevers with dimensions of 2 mm X 5 mm were laser engraved (Laser cutter settings: 0.2% power and 0.1% speed) [247] into the regions consisting of both PIPAAm and PDMS layers.

2.4.2 Cell Culture

Normal human BSM cells (Lonza, Walkersville, MD) were purchased at passage two and cultured in growth medium consisting of M199 culture medium (GIBCO, Invitrogen, Carlsbad, CA) supplemented with 10% heat inactivated fetal bovine serum, 10 mM HEPES, 0.1 mM MEM nonessential amino acids, 20 mM glucose, 1.5 μM vitamin B-12, 50 U mL^{-1} penicillin, and 50 U mL^{-1} streptomycin (GIBCO) [246]. Cells were allowed to proliferate in tissue culture flasks until they reached 70-80% confluence. Experiments were performed using cells from passage 5-7. The cells were trypsinized with 0.25% of trypsin-EDTA (GIBCO), seeded onto chips at a density of 25,000 cells cm^{-2}, and cultured in the growth media for 48 hours to form a confluent tissue. The growth media was then replaced with a serum free media of M199, supplemented with 10 mM HEPES, 0.1 mM MEM nonessential amino acids, 20 mM glucose, 1.5 μM vitamin B-12, 50 U mL^{-1} penicillin, and 50 U mL^{-1} streptomycin for 24 hours to induce a

contractile phenotype [245]. After 24 hours, induction of the asthmatic phenotype was achieved by supplementing the serum free media with 100 ng mL^{-1} human IL-13 (Sigma-Aldrich) during the final 10-14 hours of culture prior to experiments. Interleukin-13 was reconstituted in 20 mM acetic acid at a concentration of 0.1 mg mL^{-1} then further diluted to 1 μg 1 mL^{-1} in 0.1% BSA for long term storage at -20 °C per the vendor specifications. The vehicle, consisting of 20 mM acetic acid diluted in 0.1% BSA, was added to the control tissue. The tissues were triple rinsed with PBS prior to experiments.

2.4.3   Contractility Experiments

bMTF experiments were performed on a Leica MZ9.5 stereomicroscope (Wetzlar, Germany) with 0.63X magnification, coupled to a National Instruments LabVIEW data acquisition board which was programmed to capture the horizontal projection of the films by taking an image every 30 seconds through the course of the experiment using a Basler A601f-2 camera (Exton, PA). bMTF chips were transferred to a 35 mm Petri dish containing Tyrode's solution (1.8 mM $CaCl_2$, 5 mM glucose, 5 mM HEPES, 1 mM $MgCl_2$, 5.4 mM of KCl, 135 mM of NaCl, and 0.33 mM of NaH_2PO_4 in deionized water, pH 7.4 at 37 °C; reagents from Sigma-Aldrich). Tyrode's solution was allowed to cool below 32 °C to allow dissolution of the PIPAAm layer. The bMTFs were then gently peeled and the dish was placed in a heated plate to re-equilibrate to 37 °C, allowing the films to reach a basal tone. For contractile studies, contraction was induced with cumulative dosing of acetylcholine chloride (Sigma-Aldrich) (ACh) dissolved in distilled water: 10 nM ACh, 100 nM ACh, 1 μM ACh, 10 μM ACh, 100 μM ACh, and 1mM ACh at ten minute intervals.

2.4.4   Relaxation Experiments

For relaxation, there were two types of studies: relaxation without preconstriction and relaxation after preconstriction. For relaxation without preconstriction, the bMTFs were peeled and allowed to achieve a basal tone as done in contractility experiments. Relaxation was then induced using cumulative dosing of isoproterenol (100 μM and 1 mM) (Sigma-Aldrich) dissolved in distilled water, dosing 15 minutes after previous dose. For relaxation after preconstriction, the bMTFs were released to their basal tone and then induced to contract with 100 nM ACh. Next, 50 μM atropine (Sigma-Aldrich) dissolved in water was added to induce relaxation and prevent further contraction. Further relaxation was induced using cumulative dosing of 100 μM isoproterenol and 1 mM isoproterenol with 15 minutes between doses.

2.4.5   Rho Kinase Inhibition Experiments

To test the effect of rho kinase in acetylcholine-induced hypercontraction, asthmatic tissues were pretreated with 10 μM HA1077 (Sigma-Aldrich) for 15 minutes in serum free culture medium. Thirty minutes prior to the contractile experiment, HA1077 was triple washed out using PBS, then moved to Tyrode's solution as described above. To test the relaxation response to HA1077, the bMTFs were peeled and allowed to achieve a basal tone as described, then induced to relax with cumulative dosing of HA1077 (10 μM and 100 μM). To determine whether HA1077 would have an additive effect with isoproterenol, tissues relaxed with cumulative dosing of 100 μM and 1 mM isoproterenol were further relaxed with 10 μM and 100 μM HA1077, with 15 minute intervals between doses.

2.4.6   Microcontact Printing

In order to engineer anisotropic BSM oriented along the longitudinal axis of the thin films, the chips were microcontact printed, as previously published [243, 245, 278]. Briefly, a silicon wafer was coated with a thin layer of SU8-2002 (MicroChem Corporation, Newton, MA), a

negative photoresist, via spin coating. After baking the photoresist-coated silicon wafer, a photomask was brought into contact with the wafer using a mask aligner, and UV light was shown through the mask. Regions exposed to UV light became insoluble and the rest was dissolved away with developer solution. After development, the etched wafer served as a template for fabrication of PDMS stamps. PDMS stamps with 15 μm lines and 2 μm spacing were incubated with 200 μl of human fibronectin (BD Biosciences, Sparks, MD) at 50 μg mL^{-1} in distilled water for one hour. Excess fibronectin was air blown from the PDMS stamp and applied to the chip which had been recently exposed to UV ozone (Model# 342, Jetlight Company Inc., Phoenix, AZ) for eight minutes in order to transiently switch the substrate to a hydrophilic state. Stamps were manually positioned so that lines were oriented along the longitudinal axis of the thin films. Seeding of cells occurred immediately after microcontact printing.

2.4.7   Western Blotting

Tissues were lysed in urea lysis buffer consisting of 100 mM Tris, 4 M urea, 5 mM EDTA, 0.5% SDS, 0.5% NP-40 (Sigma-Aldrich), and Halt Protease and Phosphatase Inhibitor Cocktail (Thermo Scientific, Rockford, IL). Licor TG-SDS running buffer (Lincoln, NE) was used for electrophoresis. Protein concentration was quantified using a bicinchoninic acid assay and a SpectraMaxM2e microplate reader (Molecular Devices, Vienna, VA). 10 μg of total protein was loaded into Criterion 4-15% polyacrylamide gels (Bio-Rad, Hercules, CA) and the gel was run for 90 minutes at 120 V. The gel was transferred to PVDF membranes (Licor) at 70 V for 40 minutes for Western analysis. Membranes were incubated in primary antibody diluted in PBS and Licor blocking buffer for 48 hours at 4°C. Primary antibodies used were α-smooth muscle actin (1:200 dilution, Abcam, Cambridge, MA), ROCK2 (1:50 dilution, Santa Cruz

Biotechnology, Santa Cruz, CA), RhoA (1:200 dilution, Santa Cruz Biotechnology, Santa Cruz, CA), and β actin (1:1000 dilution, Santa Cruz Biotechnology, Santa Cruz, CA). Secondary antibodies were conjugated with infrared labels (1:1000 dilution, Licor, Lincoln, NE) and imaged with a Licor Odyssey reader (Licor, Lincoln, NE). Densitometry analysis was carried out using Odyssey 3.0 software and ImageJ (NIH, Bethesda, MD) and the quantified values were compared using the student's t-test.

2.4.8 Actin alignment quantification

Engineered tissues were fixed with 4% paraformaldehyde (16% stock diluted in PBS, Electron Microscopy Sciences, Hatfield, PA) for 10 minutes and subsequently permeabilized with 0.05% Triton X-100 (Sigma-Aldrich) for 12 minutes. Tissues were triple rinsed with PBS. These fixed and permeabilized tissues were stained with the Alexa Fluor 488-conjugated Phalloidin (Product# A12379 Invitrogen, Carlsbad, CA) and 4', 6-diamidino-2-phenylindole (DAPI) (Catalog #D1306, Invitrogen, Carlsbad, CA) [245]. Ten randomly chosen fields of view for each coverslip were imaged on an inverted light microscope (Leica DMI 6000B, Wetzlar, Germany) in epifluorescence using a 40x objective lens and a Coolsnap HQ CCD camera (Roper Scientific, Tucson, AZ) controlled by IPLab Spectrum (BD Biosciences/Scanalytics, Rockville, MD). Custom MATLAB software (MathWorks, Natick, MA) based on fingerprint detection, as previously reported [244, 245], was used to threshold actin immmunosignals and detect the orientation angles of continuous pixel segments. The orientation angles were consolidated for each tissue for calculation of the orientational order parameter (OOP) [244], where 1 represents perfect alignment and 0 represents random organization [265]. Quantified values were compared using the student's t-test.

2.4.9 Calculation of bMTF Tissue Stress

bMTF tissue stresses were calculated using previously published methods [243, 244]. Images of bMTFs were thresholded using custom ImageJ (NIH, Bethesda, Maryland) software, as previously described [244]. MATLAB software (MathWorks, Natick, MA) was used to calculate the stress generated by each film based on the horizontal projection of the radius of curvature, thickness of the PDMS film, and tissue layer thickness, using methods previously described [244]. The thickness of the PDMS thin films was determined using a contact profilometer (Dektak 6M, Veeco Instruments Inc., Plainview, NY). F-actin was stained with Alexfluor 488 phalloidin (Product# A12379 Invitrogen, Carlsbad, CA) and local thickness was measured using the z-plane projections of f-actin filaments using a Zeiss LSM 5 LIVE confocal microscope with a Plan-Neofluar 40X/1.3 oil objective. Contractility experiments comparing stress values of healthy and IL-13 exposed tissue at each concentration of acetylcholine failed the Shapiro-Wilkinson test for normality and were thus statistically evaluated using the Mann-Whitney Rank Sum Test. For contractility experiments comparing the stress values of healthy tissues, IL-13 exposed tissues, and IL-13 exposed tissues pretreated with HA1077, stresses at each concentration failed the Shapiro-Wilkinson test for normality and therefore were evaluated using the Kruskal-Wallis One Way ANOVA on Ranks and compared pairwise using Dunn's Method. Results with p-values less than 0.05 were considered statistically significant.

2.4.10   Statistical Analysis

Contractility experiments comparing stress values of healthy and the IL-13 induced asthmatic phenotypes at each concentration of acetylcholine failed the Shapiro-Wilkinson test for normality and were thus statistically evaluated using the Mann-Whitney Rank Sum Test. For contractility experiments comparing the stress values of the healthy phenotype, the IL-13 induced asthmatic phenotype, and the IL-13 induced asthmatic phenotype pretreated with

HA1077, stresses at each concentration failed the Shapiro-Wilkinson test for normality and therefore were evaluated using the Kruskal-Wallis One Way ANOVA on Ranks and compared pairwise using Dunn's Method. Results with p-values less than 0.05 were considered statistically significant.

3   A Human *In Vitro* Model of Duchenne Muscular Dystrophy Muscle Formation and Contractility

Tongue weakness, like all weakness in Duchenne muscular dystrophy (DMD), occurs due to contraction-induced muscle damage and deficient muscular repair. While membrane fragility is known to potentiate injury in DMD, whether or not muscle stem cells are implicated in deficient muscular repair remains unclear. We hypothesized that DMD myoblasts are less sensitive to cues in the extracellular matrix designed to potentiate structure-function relationships of healthy muscle. To test this hypothesis, we drew inspiration from the tongue and engineered contractile human muscle tissues on thin films. On this platform, DMD myoblasts formed fewer and smaller myotubes, and exhibited impaired polarization of the cell nucleus and contractile cytoskeleton when compared to healthy cells. These structural aberrations were reflected in their functional behavior as engineered tongues from DMD myoblasts failed to achieve the same contractile strength as healthy tongue structures. These data suggest that dystrophic muscle may fail to organize with respect to extracellular cues necessary to potentiate adaptive growth and remodeling.

3.1   Introduction

Duchenne muscular dystrophy (DMD) is a progressive muscle wasting disease that occurs in childhood and results in early death. Improvements in clinical management [279, 280] have lengthened the lifespan of DMD patients despite the present lack of an etiologic therapy. As patients live longer, management of late stage clinical manifestations such as dysphagia [95, 281], has become increasingly important for maintaining quality of life. In DMD, dysphagia occurs during the oral phase of swallowing [282] where tongue weakness causes failed propulsion of food from the oral cavity to the pharynx. The cause of tongue weakness, like all muscle weakness in

DMD, is failure of muscle stem cells to repair damaged muscle - which is instead replaced with fibrofatty tissue.

We reasoned that muscular repair in the tongue proceeds in the same manner as other muscles: satellite cells proliferate and differentiate into myoblasts which align with the underlying extracellular matrix (ECM), elongate, and fuse to form nascent myotubes [283-285]. In DMD, loss-of-function mutations to dystrophin cause impairment of satellite cell division [68] and degrade the structural integrity of skeletal muscle cells [286]. However, whether dystrophin-deficiency affects myoblasts and the role of ECM cues in fusion and myofibrillogenesis processes is still largely unknown. A study comparing myoblasts derived from young and old *mdx* mice [287], a murine model of DMD, found that fewer cells from old-aged *mdx* muscle exhibited myogenic markers and instead had increased expression of collagen type I. The disparate expression profile of myogenic markers between young and old *mdx* mice suggests DMD myoblasts may have reduced potential to proceed through myogenesis due to acquisition of a fibrotic phenotype.

In this chapter, we introduce a tongue-inspired *in vitro* platform for study of muscle formation and function using myoblasts from healthy and DMD patients. The film bending elicited by muscle contraction on our cantilevered design [244] mimics the tongue bending that occurs during swallowing, where the superior muscle layer contracts more than the inferior muscle layers [288] producing a bending motion. We hypothesized that DMD myoblasts are less sensitive to cues in the ECM designed to potentiate the structure-function relationships of healthy muscle. To test this hypothesis, we analyzed the cytoskeletal and nuclear alignment of healthy or DMD myoblasts seeded on to an array of narrowly spaced ECM bands patterned on our engineered tongue on a chip. We found that the cytoskeleton (CSK) and nuclei of DMD

myoblasts failed to polarize to the same degree as healthy tissues. These structural differences yielded fewer and smaller myotubes in DMD tissues. Furthermore, comparison of contractile function of healthy and DMD tissues revealed profound contractile weakness in DMD engineered tongues. These data suggest impaired polarization with respect to the underlying ECM observed in DMD myoblasts may prevent the muscular repair necessary to potentiate strong and efficient contractile function of healthy muscle.

3.2   Results and Discussion

3.2.1   Developing a tongue on a chip

Tongues are muscular hydrostats whose movements are facilitated by a complex, multilayer architecture [289], where the superior extrinsic muscles align in parallel to the longitudinal axis of the tongue (Fig. 3-1 A) and the intrinsic muscles of the tongue orient orthogonal to the tongue surface. The sagittal tongue bending that occurs during swallowing is achieved by contraction of the superior longitudinal muscle and antagonistic contraction of the intrinsic muscular core, which prevents shortening of the longitudinal muscle [290] and instead causes bending (Fig. 3-1 A). Here, we took inspiration from the bending motion of the tongue to engineer laminar anisotropic muscles on stiff but elastic thin films that bend, instead of shorten, upon muscle contraction (Fig. 3-1 B). We refer to this bio-inspired platform as tongue on a chip as the contractile measurements obtained using this platform can serve as a strength assessment test analogous to measurements of tongue strength performed clinically that quantify the pressure generated during sagittal bending against the palate of the mouth [95, 281].
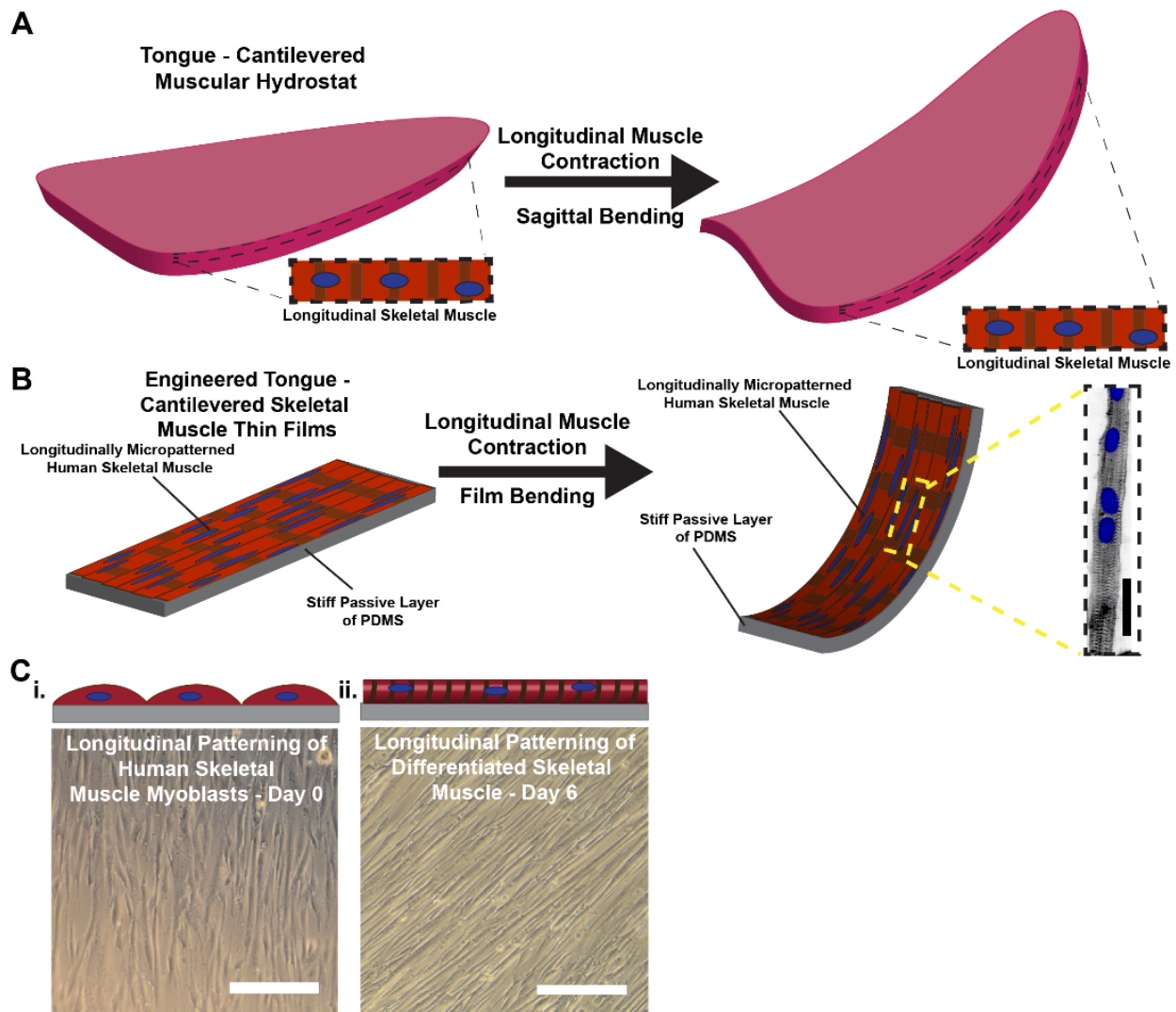
Figure 3-1. Designing tongue on a chip.

(A) Schematic representation of tongue bending due to contraction of a longitudinal skeletal muscle. (B) Schematic representation of tongue on a chip. Immunostain shows myotube cultured on PDMS film (SAA: black; nuclei: blue, Scale = 50 µm). (C) Representative tissue culture images of (i) myoblasts and (ii) differentiated skeletal muscle. Scale = 100 µm.

3.2.2 DMD myoblasts exhibit decreased CSK and nuclear anisotropy

We engineered the tongue chips with human myoblasts from healthy or DMD patients. An inherit limitation of primary cell sources is the variability within the host muscle microenvironment. To minimize differences in host muscle microenvironments such as fibrosis in DMD muscle, myoblasts derived from a 2 year old DMD patient were utilized, an age that typically precedes clinical symptoms [69]. Western blot studies confirmed expression of myogenin in healthy and DMD tissues, indicating the myoblasts had maintained a myogenic phenotype (Fig. 3-2 A); however, contributions of distinct host microenvironments cannot be entirely eliminated in interpretation of the data in this report.
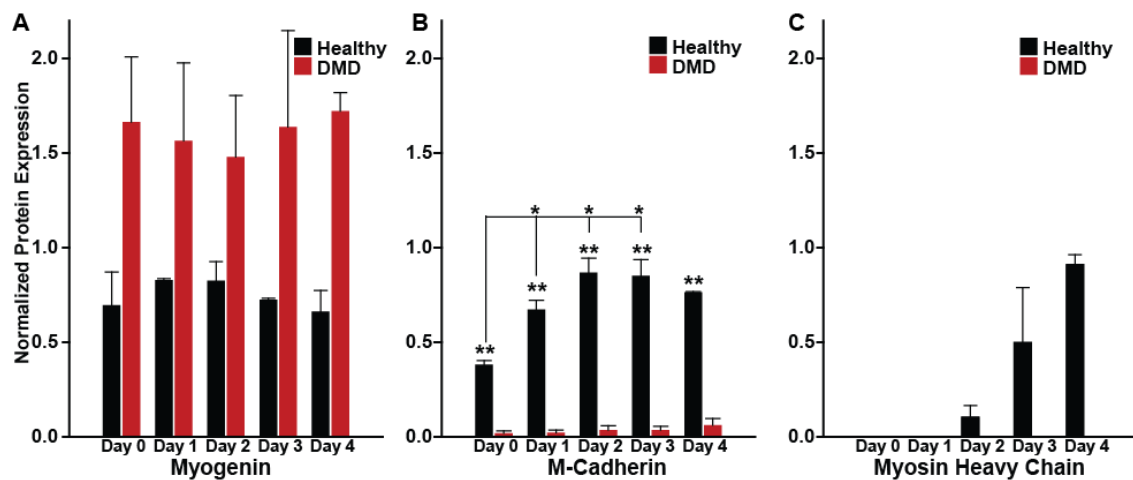
Figure 3-2. Healthy tissues begin fusion before DMD tissues

(A) Normalized myogenin expression is plotted for healthy and DMD tissues for day 0-4 of differentiation. Bars represent mean ± SEM of n=2 independent experiments, where protein was collected from 2 biological replicates for each condition, on each day for each experiment. No statistical significant differences were observed. **(B)** Normalized M-cadherin expression is plotted for healthy and DMD tissues for day 0-4 of differentiation. Bars represent the mean ± SEM of n=2 independent experiments, where protein was collected from 2 biological replicates for each condition, on each day for each experiment. * indicates $p<0.05$ relative to another day

within a **(continued)** condition. ** indicates p<0.05 relative to the DMD condition on the corresponding day. **(C)** Normalized myosin heavy chain expression is plotted for healthy and DMD tissues for day 0-4 of differentiation. Bars represent the mean ± SEM of n=2 independent experiments, where protein was collected from 2 biological replicates for each condition, on each day for each experiment. No quantifiable myosin heavy chain expression was observed in healthy samples on day 0-1. No quantifiable myosin heavy chain expression was observed in DMD samples at any investigated time point during this study.

In vivo, myoblast migration and polarization are guided by ghost fibers left behind by damaged myofibers promoting myotube formation [283]. Fibronectin (FN) [81] and merosin (M) [84] have been identified as critical ECM proteins within the muscle stem cell niche for muscle regeneration. We hypothesized DMD myoblasts are less sensitive to cues in the ECM that guide the alignment and polarization requisite for myotube formation. To test this hypothesis, FN, M, or a mixture of FN and M (FNM) was microcontact printed in an array of narrowly spaced bands and seeded with myoblasts. Myoblasts were cultured in growth media to allow for formation of a confluent tissue (Day 0). Immunohistochemistry was used to identify the actin CSK and nuclei within the tissues (Fig. 3-3 A i-ii). The alignment of the actin CSK was quantified by calculating the orientational order parameter (OOP) [291], a score of global anisotropy ranging from 0 to 1, representing random or parallel alignment, respectively. The actin CSK of the DMD myoblast tissues was less aligned compared to the healthy myoblast tissues cultured on FN, M, and FNM (Fig. 3-3 B, 3-4 A, D, 3-5 A, D), suggesting DMD myoblasts do not align with the underlying ECM as effectively as healthy controls.
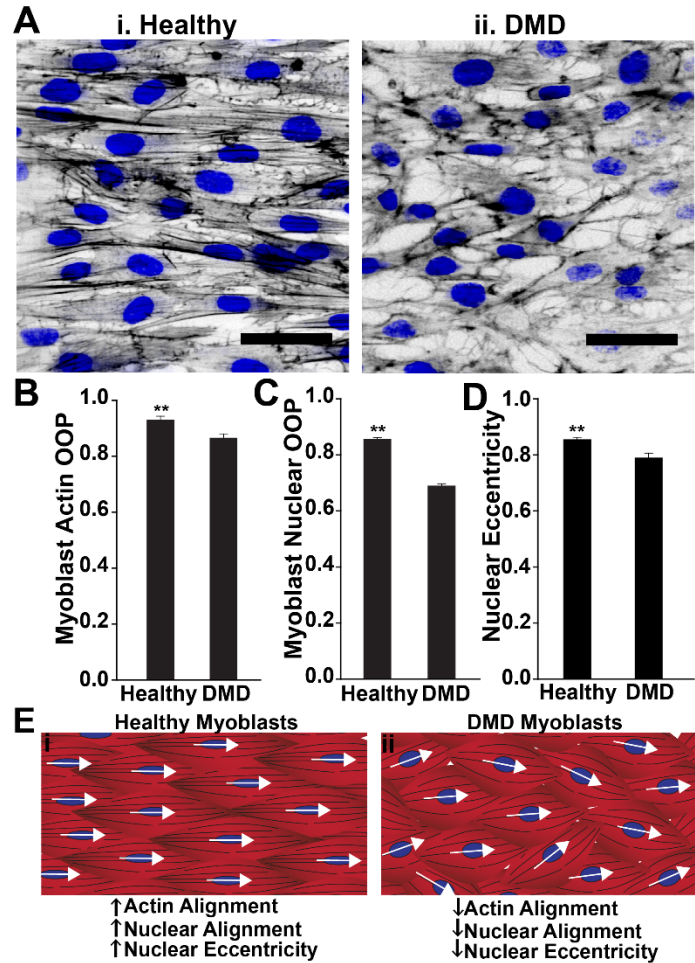
Figure 3-3. DMD myoblasts exhibit decreased cytoskeletal and nuclear anisotropy.

(A) Representative (i) healthy and (ii) DMD myoblast tissues immunostained for f-actin (black) and nuclei (blue). Scale = 50 μm. **(B)** Actin OOP is plotted. N=5 coverslips, 10 FOVs per sample, for each condition. **(C)** Myoblast nuclear OOP is plotted. N=5 coverslips, 3 FOVs per sample, >700 nuclei analyzed for each condition. **(D)** Myoblast nuclear eccentricity is plotted. N=5 coverslips, 3 FOVs per sample, >700 nuclei analyzed for each condition. **(E)** Schematic representation of (i) healthy and (ii) DMD myoblasts and summary of results. Black lines represent actin fibrils. White arrows represent orientation of the nuclei (blue). For all data in this figure, ** indicates p<0.05. All FOVs were 318.5 μm x 318.5 μm. Bars represent mean ± standard error of the mean (SEM).

Moreover, polarized cells of larger aspect ratio exhibit nuclei of greater eccentricity [292,293] and decreased nuclear offset than cells of smaller aspect ratio [293]. To quantify nuclear alignment and shape, we used a previously described method that utilizes an ellipse-fitting tool to outline each nucleus within a field of view [294]. Nuclear OOP was calculated using the orientations of the major axis of the fitted ellipses. A comparison of the nuclear alignment revealed DMD myoblast tissues had decreased nuclear alignment (Fig. 3-3 C, 3-4 E, 3-5 E) relative to healthy controls regardless of ECM composition. Healthy myoblasts formed organized tissues with high nuclear eccentricity when seeded on FN and FNM substrates (Fig. 3-3 D, 3-5 F). Tissues formed on merosin alone exhibited decreased actin OOP, nuclear OOP, and eccentricity in both healthy and DMD samples (Fig. 3-3 B-D, 3-4 D-F, 3-5 D-F). Collectively, these data indicate DMD myoblasts do not align and polarize in same manner as healthy myoblasts in response to ECM cues alone.
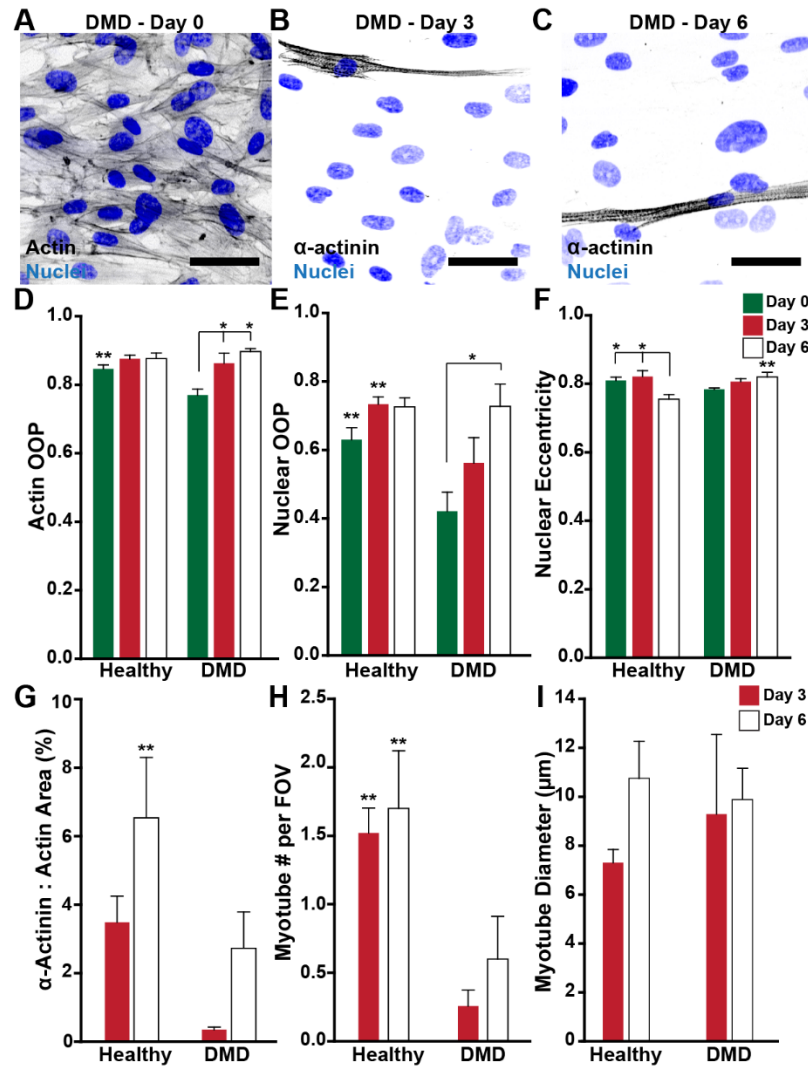
Figure 3-4. Healthy and DMD myoblasts have decreased alignment and form fewer myotubes when cultured on M.

(A) Representative image of D0 DMD myoblast tissue immunostained for actin (black) and nuclei (blue). Scale = 50 μm. **(B-C)** Representative (B) D3 DMD tissue and (C) D6 DMD tissue immunostained for sarcomeric α-actinin (black) and nuclei (blue). Scale = 50 μm. **(D)** Actin OOP is plotted for healthy and DMD tissues. Bars represent the mean ± SEM, n=5 coverslips, 10 fields of view (318.5 μm x 318.5 μm) per sample, for each condition. **(E)** Nuclear OOP is plotted for healthy and DMD tissues. Bars represent the mean ± SEM, n=5 coverslips, 3 fields of view (318.5 μm x 318.5 μm) per sample, >400 nuclei analyzed for each day, for each condition. **(F)**

Nuclear **(continued)** eccentricity is plotted for healthy and DMD tissues. Bars represent the mean ± SEM, n=5 coverslips, 3 fields of view (318.5 μm x 318.5 μm) per sample, >400 nuclei analyzed for each condition. **(G)** The α-actinin to actin area ratio is plotted for each condition for D3 and D6. Bars represent mean ± SEM, n=5 coverslips, 10 fields of view (318.5 μm x 318.5 μm) per sample, for each condition, for each day. **(H)** The myotube number per field of view (318. 5 μm x 318.5 μm) is plotted for each condition. Bars represent the mean ± SEM. **(I)** Myotube diameter is plotted for each condition. Bars represent the mean ± SEM, n=5 coverslips, 10 fields of view (318.5 μm x 318.5 μm) per sample, for each condition, for each day. * indicates p<0.05 relative to another day within a condition. ** indicates p<0.05 relative to the other condition on the corresponding day.
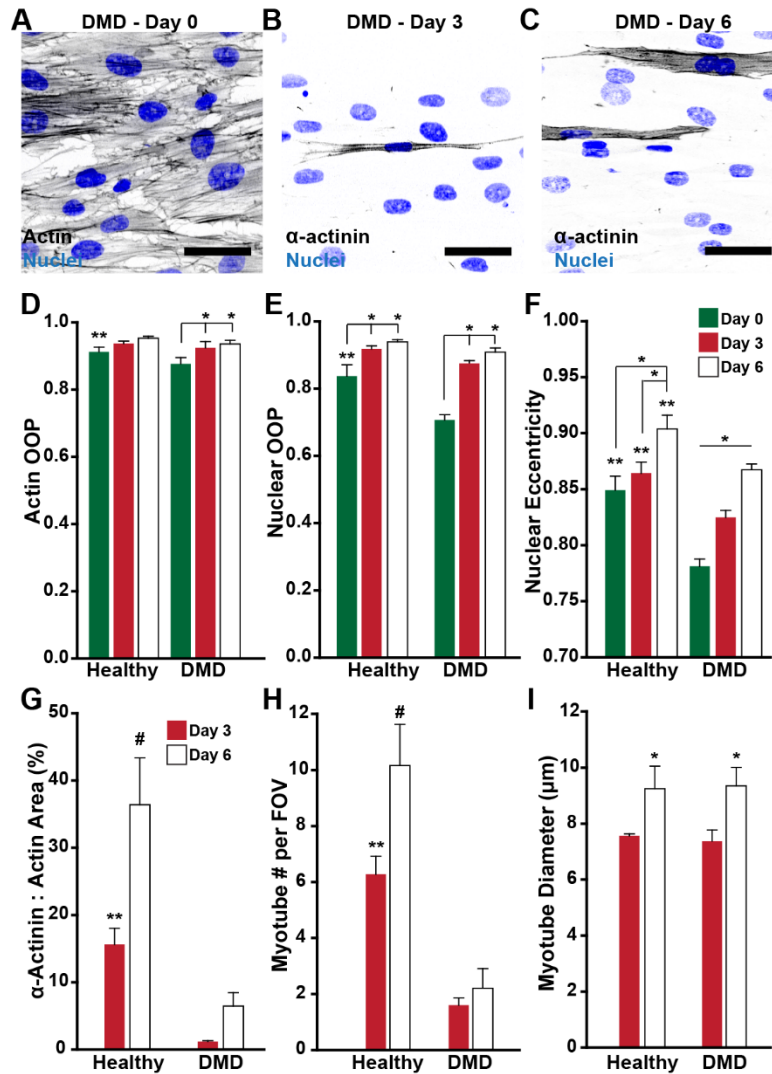
Figure 3-5. Healthy and DMD tissues align and form myotubes similarly when cultured on a mixture of FN and M as compared to FN alone.

(A) Representative image of D0 DMD myoblast tissue immunostained for actin (black) and nuclei (blue). Scale = 50 μm. **(B-C)** Representative (B) D3 DMD tissue and (C) D6 DMD tissue immunostained for sarcomeric α-actinin (black) and nuclei (blue). Scale = 50 μm. **(D)** Actin OOP is plotted for healthy and DMD tissues. Bars represent the mean ± SEM, n=5 coverslips, 10 fields of view (318.5 μm x 318.5 μm) per sample, for each condition. **(E)** Nuclear OOP is plotted for healthy and DMD tissues. Bars represent the mean ± SEM, n=5 coverslips, 3 fields of view

(continued) (318.5 µm x 318.5 µm) per sample, >400 nuclei analyzed for each day, for each condition. **(F)** Nuclear eccentricity is plotted for healthy and DMD tissues. Bars represent the mean ± SEM, n=5 coverslips, 3 fields of view (318.5 µm x 318.5 µm) per sample, >400 nuclei analyzed for each condition. **(G)** The α-actinin to actin area ratio is plotted for each condition for D3 and D6. Bars represent the mean ± SEM, n=5 coverslips, 10 fields of view (318.5 µm x 318.5 µm) per sample, for each condition, for each day. **(H)** The myotube number per field of view (318. 5 µm x 318.5 µm) is plotted for each condition. Bars represent the mean ± SEM, n=5 coverslips, 10 fields of view (318.5 µm x 318.5 µm) per sample, for each condition, for each day. **(I)** Myotube diameter is plotted for each condition. Bars represent the mean ± SEM, n=5 coverslips, 10 fields of view (318.5 µm x 318.5 µm) per sample, for each condition, for each day. * indicates $p < 0.05$ relative to another day within a condition, ** indicates $p < 0.05$ relative to the other condition on the corresponding day. # indicates $p < 0.05$ relative to the other day within a condition and to the other condition on the corresponding day.

3.2.3   DMD myotubes form aligned CSK but have less eccentric nuclei

Previous studies [295, 296] report changes in myoblast morphology from fibroblast-like to an elongated, bi-polar morphology in response to switching to a low-serum differentiation media, prior to fusion. We hypothesized that DMD myoblasts would undergo more significant morphological changes in response to a serum deficit due to decreased polarization in response to ECM cues alone. To test this hypothesis, we assessed cellular polarization in the presence of media containing high (Day 0 (D0)) and low (D3 and D6) amounts of serum by quantifying the actin OOP, nuclear OOP, and nuclear eccentricity (Fig. 3-6 A, Fig. 3-4 D-F, Fig. 3-5 D-F). In healthy and DMD tissues cultured on FN, the actin alignment increased from D0 to D6, but not

in healthy tissues cultured on M or FNM (Fig. 3-6 A-B, 3-4 D, 3-5 D). Additionally, a significant increase in nuclear alignment occurred from D0 to D3 and D6 in healthy and DMD tissues cultured on FN and FNM, as well as DMD tissues cultured on M (Fig. 3-6 C, 3-4 E, 3-5 E). Similarly, nuclear eccentricity increased from D0 to D6 in healthy and DMD tissues cultured on FN or FNM (Fig. 3-6 D, S3 F) but not on M (Fig. 3-4 F). The relatively large increase in nuclear alignment and eccentricity in DMD tissues from D0 to D3 is consistent with the morphological changes observed in myoblasts prior to fusion[297], whereas healthy myoblasts on FN and FNM exhibited highly aligned and eccentric nuclei on D0 due to the ECM patterning alone. Collectively, these data suggest myoblasts align their actin CSK and nuclei in parallel with the underlying ECM prior to fusion; however, DMD myoblasts require additional cues, such as deficits in growth factors, to achieve the alignment and polarization observed in healthy tissues.
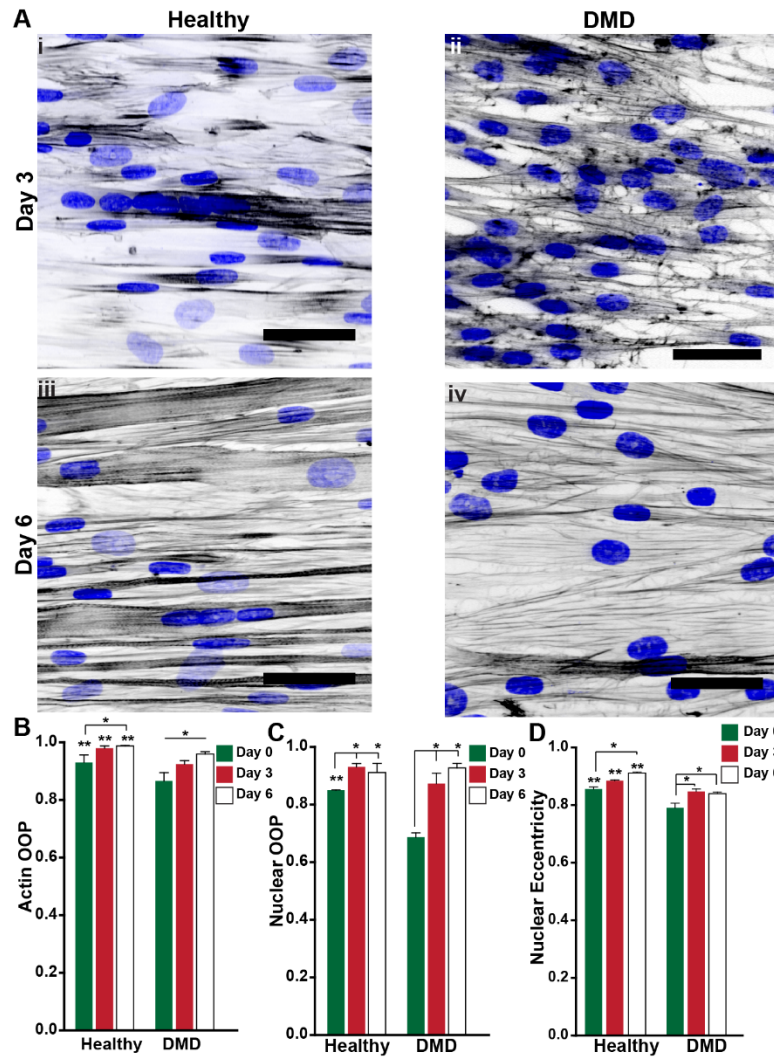
Figure 3-6. DMD myotubes form aligned actin CSK but have less eccentric nuclear shape

(A) Representative images of D3 (i-ii) and D6 (iii-iv) healthy (i, iii) and DMD tissues (ii, iv) immunostained for f-actin (black) and nuclei (blue). Scale = 50 μm. **(B)** Actin OOP is plotted. N=5 coverslips, 10 FOVs per sample, for each condition. **(C)** Nuclear OOP is plotted. N=5 coverslips, 3 FOVs per sample, >400 nuclei analyzed for each day, for each condition. **(D)** Nuclear eccentricity is plotted. N=5 coverslips, 3 FOVs per sample, >400 nuclei analyzed for each condition. For all data in this figure, * indicates $p<0.05$ relative to other days within a condition, ** indicates $p<0.05$ relative to the other condition on the corresponding day. All FOVs were 318.5 μm x 318.5 μm. Bars represent the mean ± SEM.

3.2.4 DMD myoblasts form fewer, smaller, and more immature myotubes

Myoblasts deficient of RhoE were shown to exhibit poor alignment and elongation, similar to DMD myoblasts prior to switching to a low-serum differentiation media, that resulted in failure of myotube formation [297]. We asked whether the decreased and delayed polarization observed in DMD tissues in the present study would result in decreased myotube formation as well. To answer this question, we quantified myotube density by counting the number of myotubes expressing sarcomeric α-actinin (SAA) per field of view. We found that healthy tissues had a greater density of myotubes on D3 and D6 compared to DMD tissues (Fig. 3-7 A, B, 3-4 H, 3-5 H). Moreover, we used Western blot to compare the expression of M-cadherin which localizes at the cell to cell junction of fusing myoblasts [298]. Consistent with the measurements of myotube density, healthy tissues had greater M-cadherin expression on D0 prior to induction of differentiation compared to DMD tissues and continued to have greater expression on D1-4 (Fig. 3-3 B). Comparison of mean myotube diameter revealed healthy myotubes cultured on FN had significantly larger diameters relative to DMD myotubes (Fig. 3-7 A, C), but mean healthy myotube diameter was decreased in tissues cultured on M and FNM compared to FN (Fig. 3-3 I, 3-4 I).
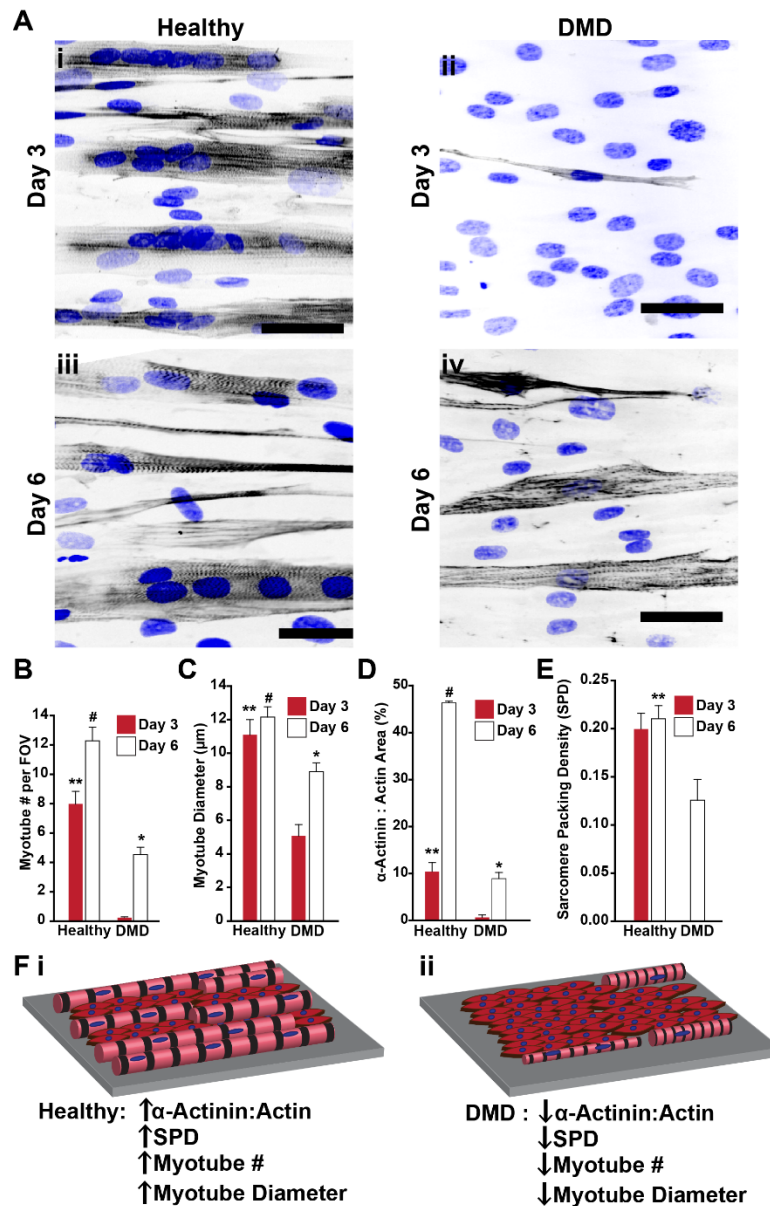
Figure 3-7. DMD myoblasts form fewer, smaller, and more immature myotubes.

(A) Representative (i-ii) D3 healthy and DMD tissues and (iii-iv) D6 healthy and DMD tissues immunostained for SAA (black) and nuclei (blue). Scale = 50 μm. **(B)** Myotube density is plotted. **(C)** Myotube diameter is plotted. **(D)** The SAA to actin area ratio is plotted for D3 and D6. **(E)** SPD is plotted. The D3, DMD condition did not have significant enough SAA expression for statistical comparison. **(F)** Schematic representation of (i) healthy and (ii) DMD tissues and summary of results. Unfused myoblasts are represented in red and fused myotubes

are represented **(continued)** in pink. For all data in this figure, n=5 coverslips, 10 FOVs (318.5 μm x 318.5 μm) per sample, for each condition, for each day. Bars represent mean ± SEM. * indicates p<0.05 relative to D3 within a condition, ** indicates p<0.05 relative to the DMD condition on the corresponding day. # indicates p<0.05 relative to the other day within a condition and to the other condition on the corresponding day.

In addition to remodeling cellular architecture during myoblast fusion, fused myoblasts undergo myofibrillogenesis. Briefly, premyofibrils form at the edges of the myotube in the form of Z-bodies, rich in punctate SAA. Over time, these Z-bodies fuse to form Z-disks that represent the boundaries of the contractile unit called sarcomeres [299]. We asked if the slower alignment of DMD myoblast tissues resulted in delayed myofibrillogenesis. To answer this question, the abundance and ordered structure of SAA of healthy and DMD engineered muscle were quantified. The abundance of SAA was measured by quantifying the projected area of SAA immunosignal relative to the area of f-actin immunosignal on D3 and D6. On D3 in healthy tissues cultured on FN and FNM, myotubes had significant expression of SAA, while very little SAA expression was observed in DMD tissues on any ECM and healthy tissues on M (Fig. 3-7 A, D, 3-4 G, 3-5 G). Furthermore, we observed greater projected area of SAA immunosignal in the healthy condition compared to the DMD condition on D6 (Fig. 3-7 A, D, 3-4 G, 3-5 G) indicating healthy tissues were at a later stage of myogenesis compared to DMD tissues. To determine whether Z-bodies were undergoing organized assembly into Z-disks, we quantified the fraction of periodically distributed SAA immunosignal, termed sarcomeric packing density (SPD) [300]. Healthy tissues had significantly greater SPD compared to DMD tissues on D6 (Fig. 3-7 E). The SAA immunosignal was not significant enough in the DMD condition on D3 to compare

statistically to the healthy condition. The relative lack of SAA and SAA organization observed in the DMD tissues at these time points is likely, in part, due to the delayed fusion in these tissues, not dystrophin deficiency alone. Collectively, these data indicate that DMD myoblasts form myotubes and undergo myofibrillogenesis but these processes are delayed relative to healthy tissues. Moreover, these data, in conjunction with previous reports[301-303], suggest that $\alpha_5\beta_1$ integrin binding to FN during muscle regeneration may serve as a transient, developmental anchor to the ECM prior to forming robust focal adhesions through the $\alpha_7\beta_1$ integrin and the dystroglycan complex binding to M in stronger, mature muscle.

3.2.5   Engineered DMD tissues exhibit contractile weakness

The majority of force transmission from sarcomeres propagates laterally through the CSK to integrin-associated and dystroglycan complexes in the sarcolemma to the ECM [304-306]. We hypothesized that engineered tissues from DMD myoblasts would contract significantly less than healthy tissues due to the absence of dystrophin as well as the relative structural immaturity observed in DMD tissues. When engineered tissues were stimulated with increasing frequency of electrical stimulation, contractile strength increased causing film bending. Using a high-speed camera, we acquired videos of film bending and used a geometrical relation to calculate the change in the radius of curvature [244]. The change in the radius of curvature, the film thickness, and the material properties of the PDMS film were imputed into the growth theory-based model used to calculate contractile stress [243].

To compare the relative contractile strength of the healthy and DMD tissues, baseline stress, peak stress, and dynamic stress were quantified (Fig. 3-8 A-B). DMD tissues had a lower baseline stress on both D3 and D6 compared to healthy tissues (Fig. 3-8 D). Similarly, DMD tissues had weaker peak stress compared to healthy tissues on D6 (Fig. 3-8 E). However, no

observable contractions were obtained from DMD tissues on D3, so a comparison of peak stress was not included for this time point. Lastly, in both conditions, we observed increases in dynamic stress as stimulation frequency was increased (Fig. 3-8 F), but no observable contractions were obtained in DMD tissues when stimulated at frequencies ranging from 1-4 Hz on D6. Healthy tissues had at least an order of magnitude greater dynamic stress on D3 and D6 relative to the D6 DMD tissues at all stimulation frequencies (Fig. 3-8 F). The large differences in dynamic stress could be a result of the structural immaturity, dystrophin deficiency, or a combination of the two, but these factors cannot be decoupled at these time points. Together, these data, for the first time, quantify contractile weakness in engineered human dystrophic skeletal muscle *in vitro*. Hence, we have demonstrated that we can recapitulate aspects of both the decreased muscle regeneration and muscle weakness observed in DMD patients utilizing a human *in vitro* model.
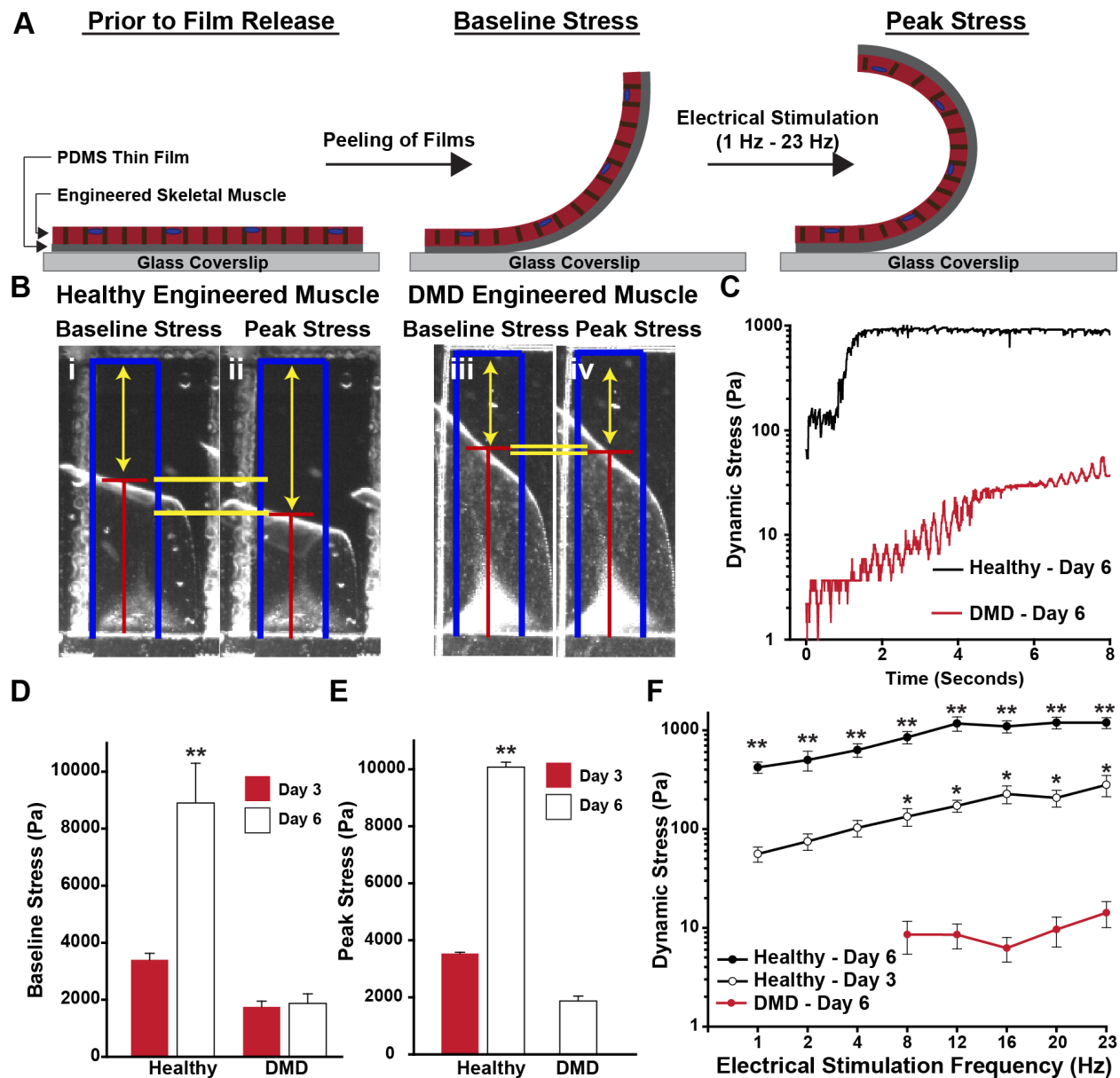
Figure 3-8. DMD tissues exhibit contractile weakness.

(A) Schematic representation of tissues prior to film release, at baseline stress, and at peak stress.

(B) Representative images of (i-ii) healthy and (iii-iv) DMD tissues at baseline (i, iii) and peak stress (ii, iv). Blue rectangles represent film length. The red bar represents the tracking of the film edge. The yellow arrows represent the distance between the projected film length and the unstressed film length. **(C)** Representative stress trace of a healthy and DMD contraction in

(continued) response to 23 Hz stimulation. **(D)** Baseline stress is plotted for the healthy and DMD conditions on D3 and D6. Bars represent median ± SEM. **(E)** Peak stress is plotted for the healthy condition on D3 and D6 and the DMD condition on D6. For the DMD condition, no contraction was observed on D3. Bars represent median ± SEM. **(F)** Dynamic stress is plotted for the healthy condition on D3 and D6 and the DMD condition on D6. For the DMD condition, no contraction was observed on D3. Data points represent the mean ± SEM. For all stress measurements (D-F): for the healthy condition, D3 condition n=11 films 3 chips; for the healthy, D6 condition n=10 films, 3 chips; for the DMD, D3 condition n=12 films, 2 chips; for the DMD, D6 condition n=14 films, 3 chips. ** indicates p<0.05 relative to both conditions on either day. * indicates p<0.05 relative to the DMD condition on D6.

In this chapter, we demonstrate the maladaptive functional consequences of the failure of self-assembly of DMD myoblasts during multiple stages of myogenesis. DMD myoblasts failed to self-organize their actin CSK and nuclei in the same manner as healthy myoblasts in response to ECM cues. These structural aberrations led to impaired myotube assembly in DMD tissues, reflected by reduced density and size of myotubes. Moreover, self-assembly of the contractile apparatus in DMD tissues was reduced and disordered compared to healthy tissues. Collectively, these structural deficits were reflected by severe contractile weakness in DMD tissues. These insights may explain, in part, how the incomplete repair of muscle results in profound muscle weakness in DMD.

3.3   Materials and Methods

3.3.1   Tongue chip fabrication

Glass coverslips (VWR, Westbury, New York) were placed vertically within a metal rack for cleaning via immersion into 70% ethanol, followed by 30 minutes of sonication. After allowing for drying, a low adhesive tape (Patco 5560) was applied to cover the entire surface of the coverslip. Next, a single rectangular island (9 mm by 5.5 mm) was laser engraved into the tape using a CO_2 laser (Epilog, Golden, CO). After removing the rectangular island, leaving the remainder of the coverslip masked, a thin layer of the thermally-sensitive polymer, poly(N-isopropylacrylamide) (PIPAAm) (Polysciences, Warrington, PA) dissolved in 1-butanol (10% w/v), was spin-coated on the exposed glass region of the chip, using a maximum rotational speed of 6000 RPM. After removal of the remaining tape, polydimethylsiloxane (PDMS) (Sylgard 184, Dow Corning, Midland, MI) was mixed at a 10:1 base to curing agent weight ratio and spin-coated at a maximum speed of 4000 RPM for one minute such that a thin, uniform layer of PDMS coated both the entire coverslip surface as well as they thin layer of PIPAAm. Subsequently, the chips were allowed to cure over night at 65°C. Next, an array of 4-6 cantilevers (2 mm wide, 5 mm long) was laser engraved into the polymer layers. Subsequently, the tongue chips were washed vigorously in sterile, 37°C phosphate-buffered saline.

3.3.2   Human skeletal muscle culture

Human skeletal muscle myoblasts (Lonza, Walkersville, MD) were purchased and cultured in a growth media consisting of M199 culture media medium (GIBCO, Invitrogen, Carlsbad, CA) supplemented with 10% heat inactivated fetal bovine serum, 10 mM HEPES, 0.1 mM MEM nonessential amino acids, 20 mM glucose, 1.5 μM vitamin B-12, and 50 U mL^{-1} penicillin (GIBCO). The myoblasts derived from a Duchenne muscular dystrophy patient were

purchased from DV Biologics (Costa Mesa, CA) and were cultured in the same growth media. Cells were plated and expanded in T-75 culture flasks (Corning, Corning, NY) prior to cell seeding. Prior to cell plating, T-75 culture flasks were incubated with 1 wt% gelatin from porcine skin (Sigma Aldrich, St. Louis) in a cell culture incubator for 30 minutes. The 1% gelatin solution was subsequently replaced with grow media in preparation for cell plating. The skeletal muscle myoblasts were allowed to proliferate over the course of 2-3 days and were seeded prior to reaching 70% confluence. Cell culture media was replenished after 48 hours after 3 rinses with sterile phosphate-buffered saline. For myoblast seeding, cells were removed from the cell culture flask using 0.25% of trypsin-EDTA (GIBCO), seeded onto chips at a density of 62,000 cells cm^{-2}. The myoblasts formed confluent monolayers of tissue after 2 days in growth media when cultured on either FN or FNM. On M, healthy and DMD myoblasts formed confluent tissues after 5 days in growth media. Next, to induce differentiation of the myoblasts, the growth media was replaced with a differentiation media consisting of DMEM-F12 (Lonza), supplemented with 2% horse serum (GIBCO). Differentiation media was replenished every 48 hours. Experiments were performed during a period ranging from 3 days culture in differentiation media to 6 days culture in differentiation media.

3.3.3   Microcontact printing

In order to direct anisotropic tissue formation along the longitudinal axis of the muscular thin film, FN, M, or FNM was microcontact printed in a geometrical pattern of an array of 15 μm bands, with 2 μm spacing, using a previously published method [245, 278]. Briefly, a silicone stamp with a defined geometrical pattern on one surface was fabricated by first fabricating a negative replica on a silicon wafer using photolithography. A silicon wafer (76 mm diameter) was coated with a layer of the negative photoresist, SU8-2002 (MicroChem Corporation, Newton, MA)

using spin-coating. After baking the photoresist-coated silicon wafer, a chrome photomask was carefully applied to the surface of the photoresist-coated wafer using a mask aligner, and UV light was shown through the mask for 7-10 seconds. Subsequently, the regions not exposed to UV light were washed away using a development solution and curing was completed by a final baking step at a maximum temperature of 180°C for 30 minutes. This etched wafer serves as a negative template for the silicone stamp. PDMS (Sylgard 184, Dow Corning) was poured over the template and degassed. The PDMS was allowed to cure overnight at 65°C. Next, the PDMS was carefully removed from the etched silicon wafer, and were cut into individual rectangular stamps for application to single coverslips. To transfer a defined pattern of ECM on to the tongue chips, the PDMS stamps were coated and subsequently incubated with human fibronectin (BD Biosciences, Sparks, MD), human merosin (Sigma Aldrich), or an equimass mixture of merosin and fibronectin at 50 μg mL^{-1} in sterile, distilled water for one hour. Next, excess ECM protein was removed from the PDMS stamp using compressed air, and the PDMS stamp was carefully applied to the MTF chip which had been recently exposed to UV ozone (Model# 342, Jetlight Company Inc., Phoenix, AZ) for 8 minutes to transiently functionalize the surface for protein binding. After removal of the PDMS stamp, the chips were rinsed with phosphate-buffered saline and promptly seeded with cells.

3.3.4   Immunohistochemistry

Engineered human skeletal muscle tissues were fixed by treatment with 4% (v/v) paraformaldehyde for 15 minutes (16% stock diluted in phosphate-buffered saline, Electron Microscopy Sciences, Hatfield, PA) and permeabilized with 0.05% (v/v) Triton X-100 in PBS at room temperature for 5 minutes. The samples were then washed with phosphate-buffered saline prior to incubation with primary antibodies. The samples were incubated with a primary antibody

solution consisting of a 1:200 dilution of monoclonal anti-sarcomeric α-actinin antibody (A7811, clone EA-53, Sigma Aldrich, St. Louis, MO) in phosphate-buffered saline for 2 hours at room temperature. After 3X rinsing with room temperature phosphate-buffered saline, the engineered tissues were incubated with a secondary solution consisting of 1:200 dilutions of Alexa Fluor 546-conjugated goat anti-mouse IgG secondary antibody (Invitrogen, Carlsbad, CA), Alexa Fluor 488-conjugated Phalloidin (Product # A12379 Invitrogen, Carlsbad, CA), and 4', 6-diamidino-2-phenylindole (DAPI) (Catalog # D1306, Invitrogen, Carlsbad, CA) for 1 hour at room temperature. Fluorescence microscopy was performed using a Zeiss LSM confocal microscope (Carl Zeiss Microscopy, Jena, Germany) using the EC Plan-Neofluar 40x/1.3 oil DIC M27 objective at room temperature.

3.3.5   Quantitative analysis of nuclear architecture

Nuclear eccentricity and orientation were quantified using a custom MATLAB software (MathWorks, Natick, MA) developed in our group and described previously [294]. Briefly, an ellipse-fitting algorithm was utilized to trace the perimeter of nuclei in immunofluorescence images, enabling measurement of major and minor axes lengths, and eccentricity. In order to measure orientation angle, an orientation vector was drawn through the longitudinal axis of the fitted ellipse. To quantify global nuclear alignment, the orientational order parameter (OOP) was calculated using the mean resultant vector of the measured orientation angles from circular statistics [307]. Measurements were repeated for every nucleus within a field of view, excluding overlapping nuclei as well as nuclei not fully within the field of view. Statistical analysis to compare nuclear data was performed using SigmaPlot™ 12.0 software (San Jose, CA). Data from each condition was analyzed using Two Way ANOVA and compared pairwise using the

Holm-Sidak method. Results with p-values less than 0.05 were considered statistically significant.

3.3.6   Quantitative analysis of actin CSK and sarcomere organization

We utilized custom image analysis software developed in our group and published previously [300] to analyze the organization of the actin CSK and sarcomeres. Briefly, for analysis of the actin CSK, the orientation of actin fibers was determined using the OrientationJ plugin [308] and the actin OOP was calculated for each sample. The global OOP was calculated for each sample by analyzing ten fields of view (318. 5 µm by 318.5 µm). Five samples were compared for each condition on each day of comparison. Statistical analysis was performed using SigmaPlot™ 12.0 software (San Jose, CA). Data from each condition was analyzed using a Two Way ANOVA and compared pairwise using the Holm-Sidak method. Results with p-values less than 0.05 were considered statistically significant.

To quantify the expression of SAA, we measured the projected area of the pixels positive for SAA immunosignal relative the projected area of the pixels positive for phalloidin immunosignal using custom MATLAB software (MathWorks, Natick, MA). In order to determine the relative presence of sarcomeres as periodic structures in the SAA stainings, we employed a previously published method from our group [300]. In brief, the 2D Fourier transform of the SAA immunostaining is radially integrating in a 1D signal that contains the relative importance of each spatial frequency. This signal was then fitted, to separate the aperiodic contribution of the z-bodies from the periodic contribution of the z-disks. The ratio of the areas under the periodic and aperiodic components, named sarcomeric packing density, was used compare the relative assembly of sarcomeres among the conditions.

Myotube density was quantified by counting the number of myotubes per field of view for 10 fields of view, for 5 coverslips, for each condition on D3 and D6. The myotube diameter was quantified by measuring the projected, cross-sectional diameter of each myotube in each

field of view using ImageJ. The average myotube density and diameter were calculated for each sample. The means of 5 coverslips were compared using a Two Way ANOVA and compared pairwise using the Holm-Sidak method. Results with p-values less than 0.05 were considered statistically significant.

3.3.7   Muscular thin film contractility measurements

For contractility experiments, the tongue chips were transferred to a 60 mm Petri dish containing normal Tyrode's solution (1.8 mM $CaCl_2$, 5 mM glucose, 5 mM HEPES, 1 mM $MgCl_2$, 5.4 mM of KCl, 135 mM of NaCl, and 0.33 mM of NaH_2PO_4 in deionized water, pH 7.4 at 37 °C; Sigma-Aldrich). Field stimulation electrodes made of 1 mm platinum wire (VWR, Radnor, PA) were built into an acrylic lid and fitted on to the 35 mm Petri dish. Contraction of the skeletal muscle was induced using an external field stimulator (Myopacer, IonOptix Corp., Milton, MA) which applied field stimulation over a range of frequencies spanning from 1 Hz to 23 Hz, with an amplitude of 10V. The horizontal projection of film bending was captured using a Leica MZ9.5 stereomicroscope (Wetzlar, Germany) with 0.63X magnification, which was coupled to a National Instruments LabVIEW data acquisition board which was programmed to capture the experiment using a Basler A601f-2 camera (Exton, PA) at a frame rate of 100 frames per second. Contractile stress quantification was performed using a previously published method from our group [243, 244]. Briefly, the change in radius of curvature was measured by first thresholding each frame of the videos of the contractile experiments to measure the projection length of each film using a custom macro ImageJ software (NIH, Bethesda, MD) that has been previously described [244]. MATLAB software (MathWorks, Natick, MA) was used to then calculate the film stress using the film projection length from each frame, the film thickness, and the PDMS material properties. The film thickness was measured using a contact profilometer

(Dektak 6M, Veeco Instruments Inc., Plainview, NY). Baseline stress was measured as the stress within the engineered muscle at rest, prior to electrical stimulation. Peak stress was measured as the stress at maximum contraction. Dynamic stress was calculated as the difference between the baseline and peak stresses, representative of the contractile stress induced by electrical stimulation. Statistical analysis was performed using SigmaPlot™ 12.0 software (San Jose, CA). Data from each condition was analyzed using the Mann-Whitney Rank Sum Test for the baseline stress and dynamic stress, and t-test for peak stresses. Results with p-values less than 0.05 were considered statistically significant.

3.3.8   Western blot protein analysis

Protein was isolated from engineered human skeletal muscle tissue by lysing cells at 4°C in RIPA lysis buffer (Sigma, St. Louis, MO) plus Complete Mini (Roche Diagnostic, Mannheim, Germany). A capillary-based Wes™ Simple Western Analysis (ProteinSimple, San Jose, CA) was used to quantify protein expression levels according to the manufacturer's protocol. Briefly, 0.5 µg lysate samples were loaded into each capillary and proteins were separated by size in the separation matrix. Target skeletal muscle differentiation proteins were identified with the following primary antibodies: myogenin (Catalog # sc576, Santa Cruz Biotechnology, Santa Cruz, Ca), m-cadherin(Catalog # sc274093, Santa Cruz Biotechnology, Santa Cruz, Ca), and fast myosin heavy chain (Catalog # M4276, Sigma-Aldrich, St. Louis, MO). α-Tubulin antibody (Catalog #ab7291, Abcam, Cambridge, MA) was used as a loading control to normalize expression levels in each sample. The proteins were immunoprobed using mouse and rabbit secondary antibodies and chemiluminescent substrate provided by the manufacturer. Chemiluminescent signals were detected and quantified using Compass Software (ProteinSimple, San Jose, CA). Data was analyzed using a two way ANOVA and compared pairwise using the

Holm-Sidak method. Results with p-values less than 0.05 were considered statistically

significant.

4   Modeling Contractile Weakness in Duchenne Muscular Dystrophy Using Human Induced-Pluripotent Stem Cells and Soft Gelatin Muscular Thin Films

Cell-based therapeutic approaches for treatment of Duchenne muscular dystrophy (DMD) have been limited by poor engraftment and maturation of skeletal muscle myoblasts, a late stage muscle progenitor cell. Similarly, development of functional engineered human skeletal muscle *in vitro* and disease models of human skeletal muscle have been limited by poor myoblast fusion and immature sarcomerogenesis. However, it is unclear whether poor engraftment and *in vitro* differentiation is due to impairments inherent to myoblasts or due to an inhospitable microenvironment. Satellite cells, which are earlier stage muscle progenitor cells, have exhibited robust ability to repair muscle after transplantation in animal studies. But, human sources of satellite cells are scarce, and expansion *in vitro* while maintaining their phenotype has not yet been achieved. Recently, recapitulation of developmental stages of muscle formation *in vitro* have enabled differentiation of human pluripotent stem cells (hPSCs) into satellite cells capable of self-renewal and differentiation into myoblasts and eventually myofibers with mature sarcomere structure. Here, in order to distinguish the role of the microenvironment and cells source in muscle formation, we adapted gelatin muscular thin films, previously developed by our group for cardiac tissue engineering, to better recapitulate the stiffness and geometry of the native skeletal muscle extracellular matrix. We then compared the contractile strength of healthy and DMD human engineered muscle derived from primary myoblasts and hPSCs after an extended differentiation on the gelatin muscular thin films.

4.1 Introduction

Skeletal muscle is maintained throughout life by a local pool of muscle stem cells called satellite cells [74, 309]. *In vivo*, satellite cells rest in a quiescent state, tightly constrained between the plasma membrane of the underlying myofiber and the basal lamina that envelops the myofiber and the satellite cell [309, 310]. In response to mechanical stresses or muscle injury, satellite cells undergo rapid proliferation and differentiate to become myoblasts, which further differentiate and fuse to repair or replace the damaged myofiber [311, 312]. Muscular repair, though, is often disrupted in aging and diseased muscle due to deleterious changes to the skeletal muscle microenvironment such as fibrosis and decreased expression of fibronectin [81, 313]. These *in vivo* findings are consistent with *in vitro* studies that indicate substrates of tissue-like stiffness are optimal for maintenance of satellite cell quiescence [314] and differentiation of myoblasts [315].

Development of functional, *in vitro* disease models of skeletal muscle derived from humans has been limited by the availability of patient cell sources and limited differentiation and maturation of human myoblasts, often exhibiting only passive force generation [316, 317]. In a recent study, Madden et al. demonstrated robust physiologic function of 3-D, human skeletal muscle for the first time by seeding high densities of myoblasts within a soft matrigel hydrogel [102]. The human myobundles mimicked responses to drugs known to cause hypertrophy as well as atrophy and contracted in response to chemical and electrical stimulation, but the studies utilized only healthy human cell sources and required large numbers of cells [102]. Our group developed a functional, *in vitro* model of Duchenne muscular dystrophy (DMD) by directing muscle formation through careful control of healthy and DMD myoblasts' alignment and shape conferred through microcontact printing of specified patterns of fibronectin [318], an important ECM protein for muscle repair. However, the stiff substrate and flat surface geometry limited the

length of culture and the contractile strength of the DMD engineered muscle. Moreover, recent advances have demonstrated the ability to robustly differentiate mouse and human, healthy and DMD induce pluripotent stem cells (hPSCs) into mature myofibers through temporal recapitulation of the chemical cues that drive development of muscle lineages *in vivo* [11, 12]. However, hPSC-derived engineered muscle has not yet been tested functionally or compared to primary-derived engineered muscle.

Previously, our group developed gelatin hydrogel-based muscular thin films for extending the culture of engineered cardiac tissue [319], utilizing a micromolding technique to provide topographical cues to direct anisotropic tissue formation [319, 320]. Here, we aimed to leverage the advantages of the physiological stiffness and composition of gelatin hydrogels with the micromolding technique [319, 320] to improve myogenesis and, therefore, contractile function of engineered muscle. Furthermore, we hypothesized hPSC-derived muscle progenitors would form myofibers more efficiently than primary-derived myoblasts and as consequence greater contractile stress.

4.2 Results and Discussion

4.2.1 High throughput manufacture of gelatin muscular thin films (MTFs)

In vivo, myofibers are enveloped by a basal lamina composed of extracellular matrix (ECM) proteins laminin and collagen as well as proteoglycans [56]. Moreover, the basal lamina is within a larger, hierarchical fibrous structure that becomes continuous with tendons at the ends of muscle, providing a physical path for force transmission from thousands of myofibers to a tendon [321]. In addition to functioning as a conduit for force transmission, the composition and geometry of the ECM guides muscular repair by directing myoblast migration, polarization, and fusion [322]. In the present study, we aimed to adapt gelatin-based muscular thin films previously

developed in our group[319] for cardiac tissue engineering to better mimic the structure of the native muscle ECM. Based on our previous work engineering human skeletal muscle [318], we used PDMS stamps with 20 μm wide topographical features (grooves), spaced 20 μm (ridges) apart with 10 μm depth (Fig. 4-1 A) such that individual myofibers would be anchored to the gelatin hydrogel on all sides except for the exposed top surface. Furthermore, we aimed to engineer gelatin hydrogels of physiological stiffness [314] since a stiffness ranging from 2-12 kPa was found to be optimal for maintenance of satellite cell quiescence [314] and a stiffness ranging from 6-18 kPa was found optimal for sarcomerogenesis [315]. A previous report indicated that a 16.5% (w/v) gelatin solution crosslinked with 4% (w/v) microbial transglutaminase (MTG) resulted in a hydrogel with a Young's modulus of ~ 15 kPa [323]. However, during preliminary testing, we found that these concentrations formed thin films too thick to enable detection of film bending for the weak contractions of the engineered DMD muscle. By reducing the gelatin concentration to 10%, we found that we could fabricate thin films sufficiently thin (100 – 200 μm) for our purposes while still being of suitable stiffness. We measured the Young's modulus to be ~5 kPa by measuring the slope of the tangent of the stress-strain curve, in the linear low strain region, derived from applying equibiaxial strain to thin gelatin films while recording the applied force on a biaxial strain tester (Fig 4 – 1 B).
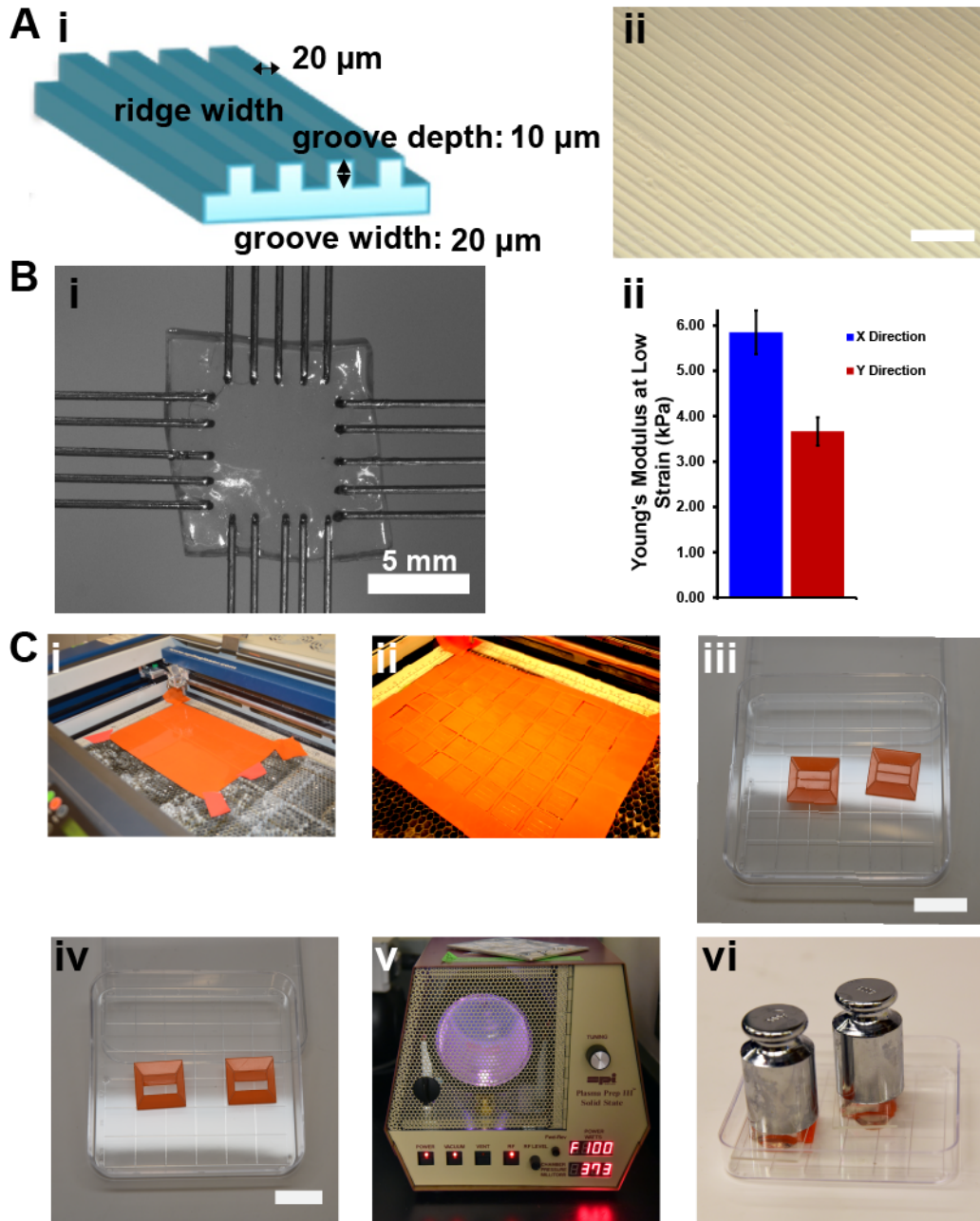
Figure 4-1. Manufacture of micromolded gelatin hydrogel substrates for engineered skeletal muscle.

(A) (i) The PDMS stamp has three salient features: 1) depth of grooves – 10 μm, 2) width of grooves – 20 μm, and 3) width of ridges - 20 μm. (ii) The pattern of the PDMS stamp is molded into the gelatin substrate. Scale bar is 200 μm. **(B)** (i) The Young's modulus was determined

(continued) using a biaxial mechanical tester at low strain (less than 10 %). (ii) The Young's

modulus was determined by measuring the slope of the stress-strain curve along each axis. The

average modulus was 4.96 ± 0.45 kPa, n=5 films. **(C)** Acrylic substrates are masked for selective

surface activation for gelatin adhesion: (i) A large sheet of acrylic is masked with a low adhesion

tape. (ii) Laser engraving enables rapid cutting of the tape layer as well as the underlying acrylic

to form coverslip substrates. (iii) The middle region of the masked acrylic substrate is cut in half.

Scale bar is 20 mm. (iv) Prior to plasma etching, the bottom half of the masked region is

removed. This region will be plasma-treated to enable secure gelatin bonding at the base of

gelatin cantilevers. Scale bar is 20 mm. (v) The chip base is treated with plasma for 10 minutes.

(vi) The upper region is removed after plasma treatment leaving just the mask frame, and freshly

mixed gelatin-microbial transglutaminase is added to the chip and is micromolded using a PDMS

stamp. A 500 g weight is added on top of the PDMS stamp to ensure a flat surface during curing.

Additionally, we adapted the manufacturing process for the gelatin MTF chips in order

to better facilitate scaling for higher throughput applications. Gelatin MTFs necessitate selective

binding of the gelatin hydrogel that each film is anchored to the underlying substrate on one end

while the other end is free [319]. Our previous method utilized masking of individual glass

coverslips with a low adhesion tape and several hour, multistep chemical activation to achieve

selective activation [319]. Here, we chose to use a thin, optically-transparent acrylic that was

flexible enough to prevent fracturing, as is common with glass coverslips during the masking

process, and amenable laser engraving thereby enabling a facile and efficient masking technique

(Fig. 4-1 C i-ii). After the acrylic sheet was masked with the low adhesion tape, laser engraving

was used to cut ~100, 22 mm x 22 mm coverslips. The masking on each coverslip is laser

engraved with an inner rectangle (16 mm x 10 mm) that is cut in half (2 rectangles: 16 mm x 5 mm) and an outer frame. In order to bond the gelatin hydrogel to the underlying acrylic substrate, the masking of the bottom half of the inner rectangle was removed, serving as the base for multiple MTFs (Fig. 4-1 C iii-iv), and was plasma treated (Fig. 4-1 C v), transiently functionalizing the substrate for protein binding [324]. After plasma treatment, the masking of the top half of the inner rectangle was removed leaving the outer frame. The gelatin-MTG solution was then rapidly pipetted on to the unmasked, inner rectangle in order to micromold the hydrogel prior to gelation and crosslinking. The PDMS stamp was carefully, but forcefully applied to the gelatin, pushing out excess hydrogel, facilitating a thin gelatin layer. A 500 g weight was placed on top of the PDMS stamp during the molding process to ensure homogenous thickness throughout (Fig. 4-1 C vi). After allowing for the crosslinking reaction to complete, the samples were immersed in phosphate buffered saline in order to rehydrate the hydrogel and to aid removal of the PDMS stamp. Lastly, 2 mm x 5 mm cantilevers were laser engraved into the hydrogel, leaving cantilevers anchored on one end and free on the other end (Fig. 4-2 A-B).
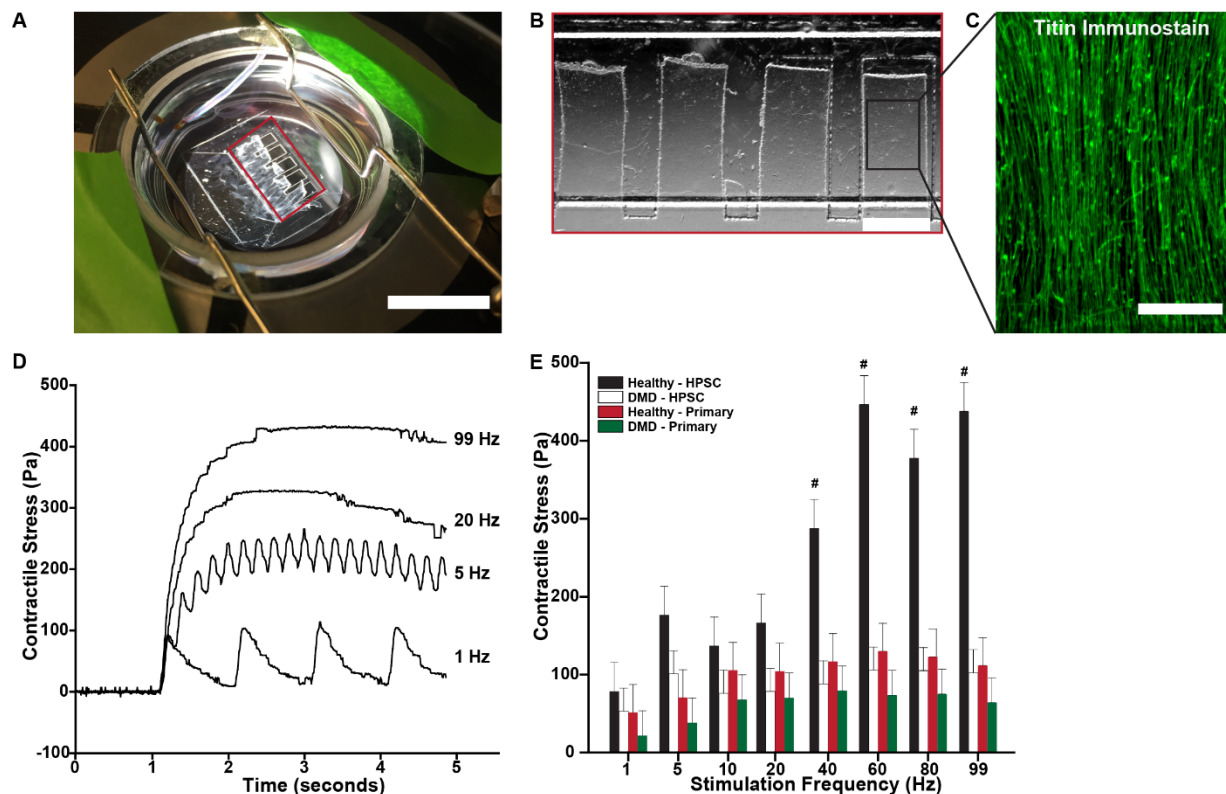
Figure 4-2. Functional Testing of Healthy and DMD hPSC-derived Engineered Muscle.

(A) Sample image of experimental set up. The chip is immersed in a 37°C experimental media maintained through feedback control. Platinum electrodes are fitted on to the petri dish. Scale bar is 20 mm. **(B)** Sample image of gelatin muscular thin films. Scale bar is 2 mm. **(C)** Representative immunostain of healthy, hPSC-derived muscle tissue stained for sarcomeric titin. Scale bar is 500 μm. **(D)** Sample stress traces of healthy hPSC-derived engineered muscle electrically stimulated at 1, 5, 20, and 99 Hz. **(E)** Contractile stress is plotted for healthy and DMD HPSC-derived engineered muscle as well as healthy and DMD primary-derived engineered muscle, stimulated from 1-99 Hz. Data points represent the mean ± SEM. N= 18 films, 6 chips, from 3 patients for the healthy, HPSC condition. N= 28 films, 6 chips, from 3 patients for the DMD, HPSC condition. N= 19 films, 6 chips for the healthy, primary-derived

condition. N= 24 films, 6 chips for the DMD, **(continued)** primary-derived condition. # indicates p<0.05 for healthy, HPSC condition relative to all other conditions.

4.2.2 Comparing Contractile Strength of Healthy and DMD, hPSC-Derived and Primary-Derived Engineered Muscle

Satellite cells exhibit robust ability to regenerate muscle after transplantation [325] in contrast to myoblasts that have demonstrated poor engraftment and maturation during clinical trials [326, 327]. Studies performed in young and old dystrophic mice indicate that the microenvironment may play a significant role in the success of subsequent engraftment and muscle formation: satellite cells in old *mdx* mice, a mouse model of DMD, exhibit poor muscular repair in comparison to young *mdx* mice [328]. However, when satellite cells from old *mdx* mice were transplanted into young *mdx* mice, muscular repair occurred as efficiently as in young *mdx* mice suggesting that increased ECM stiffness due to fibrosis in the extracellular microenvironment in dystrophic muscle may also contribute to decreased muscle repair [328]. It remains unclear though whether the failed engraftment of myoblasts in clinical trials was due to the use of myoblasts or due to a remodeled microenvironment.

We hypothesized healthy and DMD engineered muscle derived from hPSCs would be stronger than muscle derived from myoblasts harvested from patients, which we term primary-derived. We reasoned that primary myoblasts lose regenerative potential throughout life. One recent study demonstrated that the aged stem cell niche has significantly less fibronectin and deletion of the fibronectin gene in young muscle, recapitulated the poor regeneration observed in old muscle [81], suggesting that decreased synthesis and deposition of ECM proteins by muscle stem cells may underlie poor muscle regeneration. And, another recent study showed that satellite cells in both aged and dystrophic muscle exhibited impaired β-1 integrin activity

suggesting that the inability to sense the microenvironment and appropriately respond to cues critical for muscle repair is an acquired phenotype [329]. Hence, to test our hypothesis, we seeded primary-derived and hPSC-derived myoblasts on to the micromolded gelatin MTFs that are of similar stiffness to that of young muscle [315]. Moreover, we refrained from further functionalizing the gelatin hydrogel with ECM proteins like fibronectin known to guide muscle repair reasoning that hPSC-derived myoblasts would be able to appropriately sense its microenvironment and synthesize the needed ECM proteins while primary-derived myoblasts would fail to do so. We found that hPSC-derived myoblasts robustly formed myofibers (Fig. 4-2 C) and exhibited contractile kinetics similar to that of mature muscle over a broad range of stimulation frequencies (Fig. 4-2 D). Additionally, we found that hPSC-derived healthy muscle was significantly stronger than primary-derived healthy muscle, as well as both primary-derived and hPSC-derived DMD engineered muscle at stimulation frequencies greater than 40 Hz (Fig. 4-2 E). The significant and large differences in contractile stress at high frequencies is consistent with clinical observations that type 2 muscle, the stronger myofiber type with stimulation frequencies of greater than 40 Hz [330], is more severely affected in DMD [96]. Interestingly, hPSC-derived DMD muscle was not significantly stronger than primary-derived DMD muscle (Fig. 4-2 E). This result may be due to poor force transmission to the substrate due to loss of the dystroglycan complex in both of these conditions, instead of poorer muscle formation; but, this must be investigated further through structural and protein expression studies. Collectively, these data indicate hPSC-derived myoblasts or satellite cells may offer an improved therapeutic option over myoblast transplantation.

Here, we have presented an improved manufacturing method for fabrication of gelatin muscular thin films that better recapitulate the native muscle microenvironment for

quantification of engineered skeletal muscle contractile strength. Moreover, for the first time, we have demonstrated recapitulated the contractile weakness observed in DMD *in vitro* using hPSC-derived muscle progenitors. Furthermore, we have demonstrated that hPSC-derived healthy myoblasts exhibit greater regenerative potential compared to primary-derived healthy myoblasts. However, these results are preliminary and further investigation to better elucidate mechanistic understanding of impaired muscle formation in DMD. But, we believe this work represents a valuable tool for testing new pharmacological and cell-based therapies.

4.3   Methods and Materials

4.3.1   Gelatin Hydrogel Preparation

In order to fabricate gelatin hydrogels of physiologically-relevant stiffness, we mixed equivolume solutions of 20% (w/v) 175 bloom, porcine, type A gelatin (Sigma, St. Louis) in phosphate buffered saline (GIBCO) and 8% (w/v) microbial transglutaminase (MTG) (Ajinomoto, Fort Lee, NJ) in phosphate buffered saline as previously described [319]. The 20% gelatin solution was incubated at 65 ˚C to ensure all of the gelatin dissolved and to minimize the solution viscosity prior to micromolding. The 8% microbial transglutaminase solution was incubated at 37 ˚C prior to micromolding. Upon careful mixing to prevent bubble formation, a final 10% gelatin, 4% MTG final solution was formed immediately prior to micromolding.

4.3.2   Fabrication of PDMS stamps

In order to direct anisotropic tissue formation, the curing gelatin-MTG hydrogel is simultaneously micromolded by a microfeatured, polydimethylsiloxane (PDMS) (Sylgard 184, Dow Corning, Midland, MI) stamp as utilized for microcontact printing and soft lithography as described previously [319]. The PDMS stamps were fabricated utilizing previously published protocols [243, 245, 278]. Briefly, a custom chrome photomask was used to block selected regions of

an SU-8 2010 negative photoresist (MicroChem, Newton, MA) coated silicon wager. Using a mask aligner, the photoresist-coated silicon wafer was exposed to UV light for 10 seconds. Subsequently, regions shielded from the UV light were washed away using a development solution and remaining regions were cured via incubation at 180 °C for 30 minutes. The etched wafer serves as the negative mold for the PDMS stamp. After silane treatment, PDMS is poured over the etched silicon wafer, degassed, and allowed to cure at 65°C overnight. Lastly, the cured PDMS was carefully peeled from the etched silicon wafer and cut for application to 22 mm x 22 mm substrates. Both the stamps and the silicon wafer were stored for reuse.

4.3.3 Gelatin Muscular Thin Film Chip Fabrication

A 20 inch by 10 inch by 400 μm sheet of optically clear acrylic (Astra Products, Freeport, NY) was neatly covered or "masked" by a low adhesion tape (3M, St. Paul, MN). In order to selectively activate regions of the acrylic substrate, an 18 mm x 10 mm rectangle was laser engraved into the masking tape covering the acrylic sheet such that each rectangle was centered within a 22 mm by 22 mm chip (Fig. 4-1 C) that is simultaneously cut using a CO_2 laser (Epilog, Golden, CO). Next, the bottom half of the inner rectangle masking the acrylic substrate was removed from each chip, leaving the remaining tape. Each chip was placed in a 100 W Plasma Prep III plasma cleaner (SPI Supplies, West Chester, PA) for 10 minutes. Subsequently, the chips are removed from the plasma cleaner, and the masked upper region of the inner rectangle was removed, remaining the outer frame of the tape. Next, the 20% gelatin solution was carefully mixed with 8% microbial transglutaminase solution, forming a 10% gelatin, 4% microbial transglutaminase solution. Quickly, 400 μL of this solution was applied to the exposed rectangle on the acrylic substrate and gently applied to coat the entire region. Then, a microfeatured, PDMS stamp was carefully applied to each chip and a 500 g weight is placed on top of the

PDMS stamp. The samples are allowed to cure at room temperature overnight. Next, the samples were immersed in phosphate buffered saline for 20 minutes to allow for gel rehydration and to minimize gel tearing during removal of the PDMS stamp. The PDMS stamps were then carefully removed and stored for reuse. Next, an array of 4-6 cantilevers (2 mm wide, 5 mm long) was laser engraved into the gelatin hydrogels. Excess regions were removed with forceps. Lastly, the gelatin substrates were vigorously rinsed five times in phosphate buffered saline and sterilized using UV ozone exposure (Model# 342, Jetlight Company Inc., Phoenix, AZ) for 30 seconds and promptly sealed and stored for seeding.

4.3.4 hPSC-derived Skeletal Muscle Culture

hPSCs were differentiated according to previously published protocols [11, 12]. Briefly, embryoid bodies were dissociated to single cells and seeded at low density (~20,000 cells cm^{-2}) on to Matrigel-coated wells (Dow Corning). Dissociated cells are maintained in a growth medium containing a ROCK inhibitor for 1-2 days to prevent apoptosis. Subsequently, cultures of less than 25% confluence were utilized for primary differentiation. Primary differentiation of hPSCs was directed through sequential recapitulation of critical stages of paraxial mesoderm differentiation as described in detail by Chal et al.[11]. Subculturing of hPSC cultures was necessary every few days due to rapid proliferation. hPSCs were detached from the underlying substrate using 0.25% trypsin (GIBCO) and replated. After 2 weeks of primary differentiation, cultures can be cryopreserved for future use. At this stage of differentiation, the hPSCs exhibited markers characteristic of myoblasts. Myoblasts were seeded on to the gelatin substrates at a concentration of 62,000 cells cm^{-2}. Myoblast cultures were allowed to proliferate to confluence in normal growth media consisting of DMEM (GIBCO) and 20% fetal bovine serum (GIBCO). Next, to induce differentiation of the myoblasts, the growth media was replaced with a

differentiation media consisting of DMEM-F12 (Lonza), supplemented with 2% horse serum (GIBCO). Differentiation media was replenished every 48 hours. Experiments were performed after 2 weeks of differentiation.

4.3.5 Primary-Derived Skeletal Muscle Culture

Primary-derived, healthy human skeletal muscle myoblasts (Lonza, Walkersville, MD) were purchased and cultured in normal growth media consisting of DMEM (GIBCO) and 20% fetal bovine serum (GIBCO). Similarly, primary-derived, DMD human myoblasts were purchased from DV Biologics (Costa Mesa, CA) and were cultured in the same growth media. Myoblasts were seeded directly from the vial after thawing on to the gelatin substrates at a concentration of 62,000 cells cm^{-2} and permitted to proliferate to confluence in normal growth media. And, differentiation was induced using the same differentiation media. Experiments were performed after 2 weeks of differentiation.

4.3.6 Young's Modulus Measurements

To determine the Young's modulus of the gelatin hydrogels, we used a biomaterials mechanical tester (BioTester, CellScale Inc., Waterloo, ON) applying equibiaxial tensile loading. Biaxial strain was applied to the substrate at a rate of 1% strain per second and increased to 70% while the applied force was recorded at 15 Hz. The modulus was measured by calculating the slope of the tangent in the linear portion of the low strain region on the stress-strain curve. We averaged the modulus of the x and y axes. The tests were performed in Tyrode's solution: 1.8 mM $CaCl_2$, 5 mM glucose, 5 mM HEPES, 1 mM $MgCl_2$, 5.4 mM of KCl, 135 mM of NaCl, and 0.33 mM of NaH_2PO_4 in deionized water, pH 7.37-7.42 at 34-37 °C (Sigma-Aldrich).

4.3.7 Muscular Thin Film Contractility Measurements

For contractility experiments, the chips were transferred to a 60 mm Petri dish containing normal Tyrode's solution. Field simulation electrodes, composed of 1 mm platinum wire (VWR, Radnor, PA) were assembled within an acrylic top that fit on to the 60 mm Petri dish. Application of electrical field stimulation (Myopacer, IonOptix Corp., Milton, MA) was utilized to induce contraction of the engineered muscle. For each chip, we stimulated the engineered muscle with a range of frequencies: 1, 5, 10, 20, 40, 60, 80, and 99 Hz, with an amplitude of 20V or 30V when 20V was insufficient. Videos of film bending were acquired using a Leica MZ9.5 stereomicroscope (Wetzlar, Germany) with 0.63X magnification and a Basler A601f-2 camera (Exton, PA) at a frame rate of 100 frames per second. The contractile stress was quantified using a modified Stoney's equation previously described by our group [13, 242]. Briefly, the video of film bending is converted to a stack of thresholded images, utilized to acquire the projection length of each film during contraction using a custom ImageJ macro (NIH, Bethesda, MD). Contractile stress is then calculated using custom Matlab software (MathWorks, Natick, MA) that uses the project film lengths, the film thickness, and the Young's modulus of the gelatin as inputs. Film thickness was quantified for each substrate using a Zeiss LSM 5 LIVE confocal microscope (Oberkochen, Germany) using a 20x objective. The gelatin substrates were doped with 200 nm fluorescent beads (Invitrogen, Carlsbad, CA) that were well distributed throughout the gel. For each substrate, a Z-stack was taken and the thickness was measured manually, ranging between 150-200 μm. The software generates absolute stress values throughout the contraction. We calculated the contractile stress by taking the difference of the peak and minimum stress measurements.

4.3.8 Statistical Analysis

The contractile stress of healthy and DMD tissues were compared in SigmaPlot™ 12.0 software (San Jose, CA) using a Two-way ANOVA, by frequency and condition. Results with p-values less than 0.05 were considered significant.

5 Conclusion

5.1 How Can Human *In Vitro* Models Improve the Drug Pipeline for Pediatric Muscular Diseases?

Presently, the drug development pipeline is extremely inefficient. The cost and time-cost of drug approval is more than $1 billion and 10 years, respectively, while the success rate is less than 12% for drugs entering clinical trials after successfully passing through preclinical studies. Hence, improved preclinical screening, i.e. early identification of ineffective drugs, prior to costly clinical trials could significantly improve efficiency by decreasing the expenditure of time and resources towards an unsafe or ineffective drug.

From a clinical perspective, developing new drugs for pediatric populations presents an ethical dilemma. In order for the new drug to be beneficial, physicians must have drug dosing, safety, and efficacy data collected from well-controlled clinical trials. Including children in clinical trials, though, presents many issues including 1) risk of harm, 2) potential assignment to a placebo group and thereby purposely withholding a potentially effective therapy, and 3) limited statistical power of trials due to limited patient population size. Moreover, historically, there has been less incentive to develop new drugs for pediatric populations because children make up a smaller portion of the entire population and are relatively healthy compared to adults. Collectively, these issues have resulted in limited drug safety and efficacy data for children. And, as consequence, physicians are often faced with the dilemma of withholding a potentially beneficial treatment or administering a potentially harmful treatment, which has caused a high rate of adverse drug reactions in children as well as suboptimal care for the most vulnerable of our population.

5.2   A Human *In Vitro* Model of Allergic, Asthmatic Bronchoconstriction and

Bronchodilation

In chapter 2, we aimed to model allergic asthma *in vitro* utilizing a tissue engineering approach. In the human airway, laminar, anisotropic smooth muscle tissue wraps circumferentially around the airway lumen such that contraction causes airway narrowing and relaxation dilates the airway. To recapitulate this structure, we used microcontact printing of fibronectin to direct anisotropic tissue formation of primary human smooth muscle cells. In order to mimic the inflammation found in the airway of asthma patients, we treated the engineered smooth muscle tissues with the cytokine, interleukin-13. Interleukin-13 is found in high concentrations in the airways of some asthma patients resistant to existing therapies. And, a monoclonal antibody directed against interleukin-13, similar to mepolizumab which is directed against interleukin-5, has been tested in phase 3 clinical trials for asthma and atopic dermatitis.

To test our model, we designed an experiment based on pulmonary function tests used clinically for airway diseases. During pulmonary function testing, clinicians measure the rate and volume of forceful expiration at rest and after treatment with a muscarinic agonist that triggers airway narrowing. Asthma patients experience an exaggerated decrease in forced expiratory volume (FEV) in response to the muscarinic agonist. Using our *in vitro* platform, we triggered smooth muscle contraction in placebo-treated and interleukin-13-treated tissues using a muscarinic agonist and measured the contractile stress. We found interleukin-13 potentiated approximately a 100% increase in contractile stress relative to the placebo-treated tissues. Moreover, clinically, asthma is distinguished from other obstructive diseases of the airway by the reversibility of airway narrowing as measured with pulmonary function testing. Using standard airway drugs, namely β agonists and muscarinic antagonists, we demonstrated the reversibility of

healthy and asthmatic contraction. Importantly, we demonstrated that we could replicate the two major functional characteristics by acquiring a readout of contractile stress in our *in vitro* model.

In addition, we aimed to determine whether interleukin-13 potentiated hypercontractility through remodelling of expression of contractile proteins or smooth muscle structure. We found that interleukin-13 did not alter expression of canonical markers of smooth muscle's contractile phenotype but did cause increased expression of RhoA, consistent with findings in mice. Additionally, tissues treated with interleukin had fewer cells per area, indicating the smooth muscle cells within these engineered tissues had greater spreading area compared to tissues treated with the placebo, consistent with previous *in vitro* studies showing cell spreading caused increased phosphorylation of myosin light chain, a key regulator of smooth muscle contraction. Furthermore, we found that tissues treated with interleukin-13 had greater alignment of the actin cytoskeleton controlled to the healthy condition.

Lastly, we aimed to target the upregulated Rho/ROCK pathway with a ROCK inhibitor to test its potential utility as a treatment for asthma. We found that administering a ROCK inhibitor prior to performing contractile experiments significantly decreased the basal tone of healthy and asthmatic tissues. Moreover, the ROCK inhibitor prevented the hypercontraction observed previously in tissues treated with interleukin-13, suggesting a ROCK inhibitor could be efficacious in prevent bronchospasms in asthma patients. We also tested whether ROCK inhibitors could improve existing rescue therapy for asthma. The ROCK inhibitor exhibited greater efficacy in inducing relaxation in both healthy and asthmatic tissues when compared to standard β agonist treatment. And, furthermore, combined treatment of contracted asthmatic engineered muscle with β agonist and a ROCK inhibitor showed greater efficacy than either treatment alone.

Collectively, with this work, we have shown that the functional attributes of allergic asthma can be modelled by exposing engineered muscle to a key component of the inflammation in asthma patients. By engineering a system amenable to quantification of contractile stress, the assay readout is analogous to the clinical readout enabling straightforward interpretation of drug effects. As proof of principle, we demonstrated that we could use this model to assess the efficacy of new drugs through the testing of the ROCK inhibitor, HA1077. We believe this system can be utilized in preclinical screening of new asthma drugs, as well as preclinical safety studies for other types of drugs. While we utilized a single cytokine for our model, a patient-specific asthma model could be achieved through quantification of cytokine levels in the airway of an asthma using bronchoalveloar lavage. Reconstituting the patient-specific chemical microenvironment will enable a broad range of allergic asthma phenotypes to be modelled and utilized for preclinical screening. Hence, prior to testing in humans, we can identify potential treatment responders and non-responders which could speed drug development and approval, reduce costs, and prevent unnecessary exposure to harm.

5.3   A Human, *In Vitro* Model of Duchenne Muscular Dystrophy Muscle Formation and Contractility

In chapter 3, we presented a human *in vitro* model of DMD muscle formation and contractility. In DMD, dystrophin-deficiency potentiates muscle injury during muscle contraction due to weakening of the sarcolemma. And, muscular repair is impaired due to disrupted assymmetic division of DMD satellite cells. So, progressive muscle wasting as consequence of injury and failed repair underlies the rapid disease progression. We aimed to develop a platform that would enable assessment of muscular formation as well as contractile function. We engineered human skeletal muscle tissues by seeding myoblasts derived from

healthy or DMD patients on to substrates micropatterned with ECM found in healthy and regenerating muscle. We then differentiated the myoblasts for approximately a week prior to experimentation.

We found that both healthy and DMD myoblasts formed more muscle fibers when seeded on to fibronectin, which is upregulated in muscle niche after injury. However, healthy myoblasts demonstrated superior cytoskeletal and nuclear alignment indicating that DMD myoblasts had an inferior ability to sense microenvironmental cues and appropriately organize its intracellular structures prior to myofiber assembly despite exhibiting key indicators of progression through myogenesis , e.g. myogenin. The poor integration of microenvironmental cues was reflected by reduced myofiber formation and the immature structure of their contractile apparatus. This finding is important because it indicates new therapies will need to target both the muscle stem cell population as well as the mature muscle. Collectively, the structural deficits observed in the DMD tissues resulted in profound contractile weakness.

The small study size of the eteplirsen trial is representative of the challenges of executing clinical trials for rare diseases and for emerging gene-based therapies that are often effective for only subpopulations of a disease. Small clinical trials raise practical and ethical questions due to limited statistical power and hence limited ability to distinguish clinical effects. The contractile stress readout of our *in vitro* system provides a critical clinical analogue to quantitative muscle function tests. Systems amenable to measurement of surrogate end points, such as dystrophin in DMD or other components of the dystroglycan complex for other muscular dystrophy, as well as contractile strength can provide invaluable data that was lacking in the eteplirsen trial and supplement clinical trials. Moreover, early preclinical trials utilizing this platform could measure the ability of a drug to improve muscle formation and contractile strength. Furthermore, we

would be able to quantify the targeted protein expression and determine how much dystrophin expression is required for improved contractile function. Implementation of this platform could significantly improve preclinical screening of drugs for DMD as well as provide clinical data supporting the use of specific markers as surrogate endpoints in clinical trials for rare diseases.

5.4 Modeling Contractile Weakness in Duchenne Muscular Dystrophy Using Induced-Pluripotent Stem Cells and Soft Gelatin Muscular Thin Films

In chapter 4, we extend our work from chapter 3 modeling DMD *in vitro* utilizing muscle progenitor cells derived from human induced-pluripotent stem cells, for the first time. Therapeutic approaches utilizing myoblasts have failed in multiple clinical trials, though it is unclear whether the failure was due to the use of myoblasts or due to maladaptive changes within the muscle microenvironment. Here, we present data that suggests hPSC-derived muscle progenitor cells may have greater ability to engraft, form muscle, and exhibit functional attributes of mature muscle compared to primary-derived myoblasts. Furthermore, the advance of achieving functional hPSC-derived is also significant for development of preclinical models for drug screening. Our work in chapter 3 demonstrated the first human model of a genetic muscular disease. This was in part due to the limited availability of patient-derived myoblasts but was also due to the poor regenerative capacity of myoblasts. However, hPSC-derived muscle progenitors offers a renewable cell source with potentially greater function. These advances combined with platforms such the ones described here present opportunities to better understand the muscular diseases described in chapter 1 and muscle wasting that occurs during aging, in cancer, in acquired immunodeficiency syndrome (AIDS) as well as the interactions of muscle with other metabolic organs such as fat and the pancreas that have significant implications for public health.

Moreover, we adapted our MTF platform to better recapitulate the native microenvironment of muscle using a high throughput manufacturing process for gelatin muscular thin film chips. Gelatin muscular thin films present an important advance for understanding muscle biology and diseases for several reasons. Throughout life, the muscle microenvironment changes significantly. It naturally becomes fibrotic and the composition of deposited ECM protein changes. And, these changes have significant functional consequences in a broad range of conditions. Gelatin muscular thin films can function as substrate that can be tuned for its application. The stiffness can be modulated simply by adjusting the concentration of the enzyme crosslinker. Similarly, simple chemistry techniques enable bonding of different ECM proteins to gelatin scaffold.

Lastly, advances in manufacturing processes are critical for adaptation of *in vitro* models. The pharmaceutical industry often operates at the opposite end of the throughput/data quality spectrum: pharmaceutical companies often use high quantities of easily acquirable data, while academic institutions obtain low quantities of often novel data. Manufacturing science must aim to bridge these gaps to speed adaption and translation of *in vitro* models.

5.5 Limitations and Future Directions

This dissertation has demonstrated a proof of principle of human-relevant *in vitro* disease models of the airway musculature and skeletal muscle for the first time. As such, several important limitations can be addressed in future adaptations of this work. First of all, both of these models lack mechanical cues that guide the structure and function of these tissues *in vivo*. In the airway, breathing presents a cyclic tension force that may help prevent the bronchospasms observed in asthma patients. Integrating dynamic mechanical cues in future airway musculature models will enable greater insight into the interaction of new drugs with homeostatic mechanical

cues. Similarly, *in vivo*, skeletal muscle is constantly exposed to mechanical loads, which play an important part in disease progression in muscular dystrophies. These mechanical forces also help developing muscle grow and mature.

Additionally, both asthma and muscular dystrophies have a natural history lasting throughout the life of the patient. For the purposes of this dissertation, we focused on recapitulating key pathological hallmarks of the diseases at relatively short time courses (on the order of a week). Future work should focus on extending the culture of these models to better understand the chronic nature of disease progression. In asthma, in addition to exacerbations resulting in hypercontractility and airway narrowing, slow remodeling of the airway occurs and is not well understood. New insights into how airway smooth muscle contributes to long term remodeling in the context of chronic airway inflammation could significantly improve the treatment of asthma patients, particularly children. Similarly, assessing contractile function and muscular repair after repeated experiments of contractions induced by different stimulation frequencies could provide new insights into muscle injury and weakness in DMD. Collectively, these models and improved adaptations of these models can be utilized for improved preclinical screening of new drugs, supplementation of clinical trials for treatments for rare diseases, as well as academically to gain new insights into underlying pathophysiology. And furthermore, these models can be further adapted to model other smooth muscle diseases affecting the gut and vasculature as well as skeletal muscle diseases.

5.6 Funding Sources

6 Bibliography

1.   Rosato J. The ethics of clinical trials: A child's view. *J Law Med Ethics*. 2000;28:362-378

2.   Sweet BV, Schwemm AK, Parsons DM. Review of the processes for fda oversight of drugs, medical devices, and combination products. *Journal of managed care pharmacy : JMCP*. 2011;17:40-50

3.   Lipsky MS, Sharp LK. From idea to market: The drug approval process. *The Journal of the American Board of Family Practice / American Board of Family Practice*. 2001;14:362-367

4.   Eddershaw PJ, Dickins M. Advances in in vitro drug metabolism screening. *Pharm Sci Technol To*. 1999;2:13-19

5.   Low LA, Tagle DA. Tissue chips to aid drug development and modeling for rare diseases. *Expert Opinion on Orphan Drugs*. 2016:null-null

6.   DiMasi JA, Grabowski HG, Hansen RW. Innovation in the pharmaceutical industry: New estimates of r&d costs. *Journal of health economics*. 2016;47:20-33

7.   Halpern SD, Karlawish JH, Berlin JA. The continuing unethical conduct of underpowered clinical trials. *Jama*. 2002;288:358-362

8.   Adams CP, Brantner VV. Spending on new drug development1. *Health economics*. 2010;19:130-141

9.   FDA. Guidance for industry: Expedited programs for serious conditions — drugs and biologics. 2013

10.   Colburn WA. Optimizing the use of biomarkers, surrogate endpoints, and clinical endpoints for more efficient drug development. *Journal of clinical pharmacology*. 2000;40:1419-1427

11.   Chal J, Al Tanoury Z, Hestin M, Gobert B, Aivio S, Hick A, Cherrier T, Nesmith AP, Parker KK, Pourquie O. Generation of human muscle fibers and satellite-like cells from human pluripotent stem cells in vitro. *Nature protocols*. 2016;11:1833-1850

12. Chal J, Oginuma M, Al Tanoury Z, Gobert B, Sumara O, Hick A, Bousson F, Zidouni Y, Mursch C, Moncuquet P, Tassy O, Vincent S, Miyanari A, Bera A, Garnier JM, Guevara G, Hestin M, Kennedy L, Hayashi S, Drayton B, Cherrier T, Gayraud-Morel B, Gussoni E, Relaix F, Tajbakhsh S, Pourquie O. Differentiation of pluripotent stem cells to muscle fiber to model duchenne muscular dystrophy. *Nature biotechnology*. 2015;33:962-969

13. Wang G, McCain ML, Yang L, He A, Pasqualini FS, Agarwal A, Yuan H, Jiang D, Zhang D, Zangi L, Geva J, Roberts AE, Ma Q, Ding J, Chen J, Wang DZ, Li K, Wang J, Wanders RJ, Kulik W, Vaz FM, Laflamme MA, Murry CE, Chien KR, Kelley RI, Church GM, Parker KK, Pu WT. Modeling the mitochondrial cardiomyopathy of barth syndrome with induced pluripotent stem cell and heart-on-chip technologies. *Nat Med*. 2014;20:616-623

14. Lee TH, Song SH, Kim KL, Yi JY, Shin GH, Kim JY, Kim J, Han YM, Lee SH, Lee SH, Shim SH, Suh W. Functional recapitulation of smooth muscle cells via induced pluripotent stem cells from human aortic smooth muscle cells. *Circulation research*. 2010;106:120-128

15. Patsch C, Challet-Meylan L, Thoma EC, Urich E, Heckel T, O'Sullivan JF, Grainger SJ, Kapp FG, Sun L, Christensen K, Xia Y, Florido MH, He W, Pan W, Prummer M, Warren CR, Jakob-Roetne R, Certa U, Jagasia R, Freskgard PO, Adatto I, Kling D, Huang P, Zon LI, Chaikof EL, Gerszten RE, Graf M, Iacone R, Cowan CA. Generation of vascular endothelial and smooth muscle cells from human pluripotent stem cells. *Nature cell biology*. 2015;17:994-1003

16. Takahashi K, Tanabe K, Ohnuki M, Narita M, Ichisaka T, Tomoda K, Yamanaka S. Induction of pluripotent stem cells from adult human fibroblasts by defined factors. *Cell*. 2007;131:861-872

17. Ding Q, Regan SN, Xia Y, Oostrom LA, Cowan CA, Musunuru K. Enhanced efficiency of human pluripotent stem cell genome editing through replacing talens with crisprs. *Cell stem cell*. 2013;12:393-394

18. Hsu PD, Lander ES, Zhang F. Development and applications of crispr-cas9 for genome engineering. *Cell*. 2014;157:1262-1278

19. Nesmith AP, Agarwal A, McCain ML, Parker KK. Human airway musculature on a chip: An in vitro model of allergic asthmatic bronchoconstriction and bronchodilation. *Lab on a chip*. 2014;14:3925-3936

20.   March S, Ng S, Velmurugan S, Galstian A, Shan J, Logan DJ, Carpenter AE, Thomas D, Sim BK, Mota MM, Hoffman SL, Bhatia SN. A microscale human liver platform that supports the hepatic stages of plasmodium falciparum and vivax. *Cell host & microbe*. 2013;14:104-115

21.   Mennecozzi M, Landesmann B, Palosaari T, Harris G, Whelan M. Sex differences in liver toxicity-do female and male human primary hepatocytes react differently to toxicants in vitro? *PloS one*. 2015;10:e0122786

22.   Rashid ST, Corbineau S, Hannan N, Marciniak SJ, Miranda E, Alexander G, Huang-Doran I, Griffin J, Ahrlund-Richter L, Skepper J, Semple R, Weber A, Lomas DA, Vallier L. Modeling inherited metabolic disorders of the liver using human induced pluripotent stem cells. *The Journal of clinical investigation*. 2010;120:3127-3136

23.   Fattahi F, Asgari S, Pournasr B, Seifinejad A, Totonchi M, Taei A, Aghdami N, Salekdeh GH, Baharvand H. Disease-corrected hepatocyte-like cells from familial hypercholesterolemia-induced pluripotent stem cells. *Molecular biotechnology*. 2013;54:863-873

24.   Zhang S, Chen S, Li W, Guo X, Zhao P, Xu J, Chen Y, Pan Q, Liu X, Zychlinski D, Lu H, Tortorella MD, Schambach A, Wang Y, Pei D, Esteban MA. Rescue of atp7b function in hepatocyte-like cells from wilson's disease induced pluripotent stem cells using gene therapy or the chaperone drug curcumin. *Human molecular genetics*. 2011;20:3176-3187

25.   Jang KJ, Mehr AP, Hamilton GA, McPartlin LA, Chung S, Suh KY, Ingber DE. Human kidney proximal tubule-on-a-chip for drug transport and nephrotoxicity assessment. *Integrative biology : quantitative biosciences from nano to macro*. 2013;5:1119-1129

26.   Desrochers TM, Palma E, Kaplan DL. Tissue-engineered kidney disease models. *Advanced drug delivery reviews*. 2014;69-70:67-80

27.   Mosadegh B, Dabiri BE, Lockett MR, Derda R, Campbell P, Parker KK, Whitesides GM. Three-dimensional paper-based model for cardiac ischemia. *Advanced healthcare materials*. 2014;3:1036-1043

28.   Lahti AL, Kujala VJ, Chapman H, Koivisto AP, Pekkanen-Mattila M, Kerkela E, Hyttinen J, Kontula K, Swan H, Conklin BR, Yamanaka S, Silvennoinen O, Aalto-Setala K. Model for long qt syndrome type 2 using human ips cells demonstrates arrhythmogenic characteristics in cell culture. *Disease models & mechanisms*. 2012;5:220-230

29. Moretti A, Bellin M, Welling A, Jung CB, Lam JT, Bott-Flugel L, Dorn T, Goedel A, Hohnke C, Hofmann F, Seyfarth M, Sinnecker D, Schomig A, Laugwitz KL. Patient-specific induced pluripotent stem-cell models for long-qt syndrome. *The New England journal of medicine*. 2010;363:1397-1409

30. Itzhaki I, Maizels L, Huber I, Zwi-Dantsis L, Caspi O, Winterstern A, Feldman O, Gepstein A, Arbel G, Hammerman H, Boulos M, Gepstein L. Modelling the long qt syndrome with induced pluripotent stem cells. *Nature*. 2011;471:225-229

31. Benam KH, Villenave R, Lucchesi C, Varone A, Hubeau C, Lee HH, Alves SE, Salmon M, Ferrante TC, Weaver JC, Bahinski A, Hamilton GA, Ingber DE. Small airway-on-a-chip enables analysis of human lung inflammation and drug responses in vitro. *Nature methods*. 2016;13:151-157

32. Broadbent L, Villenave R, Guo-Parke H, Douglas I, Shields MD, Power UF. In vitro modeling of rsv infection and cytopathogenesis in well-differentiated human primary airway epithelial cells (wd-paecs). *Methods in molecular biology*. 2016;1442:119-139

33. Huh D, Leslie DC, Matthews BD, Fraser JP, Jurek S, Hamilton GA, Thorneloe KS, McAlexander MA, Ingber DE. A human disease model of drug toxicity-induced pulmonary edema in a lung-on-a-chip microdevice. *Science translational medicine*. 2012;4:159ra147

34. Huh D, Matthews BD, Mammoto A, Montoya-Zavala M, Hsin HY, Ingber DE. Reconstituting organ-level lung functions on a chip. *Science*. 2010;328:1662-1668

35. Kim HJ, Huh D, Hamilton G, Ingber DE. Human gut-on-a-chip inhabited by microbial flora that experiences intestinal peristalsis-like motions and flow. *Lab on a chip*. 2012;12:2165-2174

36. Lee J, Choi JH, Kim HJ. Human gut-on-a-chip technology: Will this revolutionize our understanding of ibd and future treatments? *Expert review of gastroenterology & hepatology*. 2016;10:883-885

37. Kim HJ, Li H, Collins JJ, Ingber DE. Contributions of microbiome and mechanical deformation to intestinal bacterial overgrowth and inflammation in a human gut-on-a-chip. *Proceedings of the National Academy of Sciences of the United States of America*. 2016;113:E7-15

38.   Cote CJ, Kauffman RE, Troendle GJ, Lambert GH. Is the "therapeutic orphan" about to be adopted? *Pediatrics*. 1996;98:118-123

39.   Gans-Brangs KR, Plourde PV. The evolution of legislation to regulate pediatric clinical trials: Present and continuing challenges. *Advanced drug delivery reviews*. 2006;58:106-115

40.   Wasserman R, Bocian A, Harris D, Slora E. Limited capacity in us pediatric drug trials: Qualitative analysis of expert interviews. *Paediatric drugs*. 2011;13:119-124

41.   Clavenna A, Bonati M. Adverse drug reactions in childhood: A review of prospective studies and safety alerts. *Arch Dis Child*. 2009;94:724-728

42.   Weiss J, Krebs S, Hoffmann C, Werner U, Neubert A, Brune K, Rascher W. Survey of adverse drug reactions on a pediatric ward: A strategy for early and detailed detection. *Pediatrics*. 2002;110:254-257

43.   Shah SS, Hall M, Goodman DM, Feuer P, Sharma V, Fargason C, Hyman D, Jenkins K, White ML, Levy FH, Levin JE, Bertoch D, Slonim AD. Off-label drug use in hospitalized children. *Arch Pediat Adol Med*. 2007;161:282-290

44.   Adminstration FaD. Accelerated approval correspondence of nda 206488. 2016

45.   Mendell JR, Goemans N, Lowes LP, Alfano LN, Berry K, Shao J, Kaye EM, Mercuri E, Eteplirsen Study G, Telethon Foundation DMDIN. Longitudinal effect of eteplirsen versus historical control on ambulation in duchenne muscular dystrophy. *Annals of neurology*. 2016;79:257-271

46.   Unger EF. Office director decisional memo, regarding nda 206488. 2016:84-126

47.   Califf RM. Re: Scientific dispute regarding accelerated approval of sarepta therapeutics' eteplirsen (nda 206488) - commissioner's decision. 2016:1-13

48.   Straub V, Campbell KP. Muscular dystrophies and the dystrophin-glycoprotein complex. *Current opinion in neurology*. 1997;10:168-175

49.   Emery AE. The muscular dystrophies. *Lancet*. 2002;359:687-695

50.   Straub V, Rafael JA, Chamberlain JS, Campbell KP. Animal models for muscular dystrophy show different patterns of sarcolemmal disruption. *The Journal of cell biology*. 1997;139:375-385

51.   Bloch RJ, Gonzalez-Serratos H. Lateral force transmission across costameres in skeletal muscle. *Exercise and sport sciences reviews*. 2003;31:73-78

52.   Rando TA. The dystrophin-glycoprotein complex, cellular signaling, and the regulation of cell survival in the muscular dystrophies. *Muscle & nerve*. 2001;24:1575-1594

53.   Disatnik MH, Rando TA. Integrin-mediated muscle cell spreading. The role of protein kinase c in outside-in and inside-out signaling and evidence of integrin cross-talk. *The Journal of biological chemistry*. 1999;274:32486-32492

54.   Mercuri E, Sewry C, Brown SC, Muntoni F. Congenital muscular dystrophies. *Seminars in pediatric neurology*. 2002;9:120-131

55.   Ross MH, Pawlina W. *Histology*. Lippincott Williams & Wilkins; 2006.

56.   Gillies AR, Lieber RL. Structure and function of the skeletal muscle extracellular matrix. *Muscle & nerve*. 2011;44:318-331

57.   Mercuri E, Yuva Y, Brown SC, Brockington M, Kinali M, Jungbluth H, Feng L, Sewry CA, Muntoni F. Collagen vi involvement in ullrich syndrome: A clinical, genetic, and immunohistochemical study. *Neurology*. 2002;58:1354-1359

58.   Campbell KP. Three muscular dystrophies: Loss of cytoskeleton-extracellular matrix linkage. *Cell*. 1995;80:675-679

59.   Tome FM, Evangelista T, Leclerc A, Sunada Y, Manole E, Estournet B, Barois A, Campbell KP, Fardeau M. Congenital muscular dystrophy with merosin deficiency. *Comptes rendus de l'Academie des sciences. Serie III, Sciences de la vie*. 1994;317:351-357

60.   Cohn RD, Campbell KP. Molecular basis of muscular dystrophies. *Muscle & nerve*. 2000;23:1456-1471

61.   Lampe AK, Bushby KM. Collagen vi related muscle disorders. *Journal of medical genetics*. 2005;42:673-685

62.   Sandona D, Betto R. Sarcoglycanopathies: Molecular pathogenesis and therapeutic prospects. *Expert reviews in molecular medicine*. 2009;11:e28

63.   Straub V, Bushby K. The childhood limb-girdle muscular dystrophies. *Seminars in pediatric neurology*. 2006;13:104-114

64.   Bushby KM. The limb-girdle muscular dystrophies-multiple genes, multiple mechanisms. *Human molecular genetics*. 1999;8:1875-1882

65.   Bushby KM. Making sense of the limb-girdle muscular dystrophies. *Brain : a journal of neurology*. 1999;122 (Pt 8):1403-1420

66.   Razani B, Lisanti MP. Caveolin-deficient mice: Insights into caveolar function human disease. *The Journal of clinical investigation*. 2001;108:1553-1561

67.   Galbiati F, Razani B, Lisanti MP. Caveolae and caveolin-3 in muscular dystrophy. *Trends in molecular medicine*. 2001;7:435-441

68.   Dumont NA, Wang YX, von Maltzahn J, Pasut A, Bentzinger CF, Brun CE, Rudnicki MA. Dystrophin expression in muscle stem cells regulates their polarity and asymmetric division. *Nat Med*. 2015;21:1455-1463

69.   Biggar WD. Duchenne muscular dystrophy. *Pediatrics in review / American Academy of Pediatrics*. 2006;27:83-88

70.   Sullivan T, Escalante-Alcalde D, Bhatt H, Anver M, Bhat N, Nagashima K, Stewart CL, Burke B. Loss of a-type lamin expression compromises nuclear envelope integrity leading to muscular dystrophy. *The Journal of cell biology*. 1999;147:913-920

71.   Bonne G, Mercuri E, Muchir A, Urtizberea A, Becane HM, Recan D, Merlini L, Wehnert M, Boor R, Reuner U, Vorgerd M, Wicklein EM, Eymard B, Duboc D, Penisson-Besnier I, Cuisset JM, Ferrer X, Desguerre I, Lacombe D, Bushby K, Pollitt C, Toniolo D, Fardeau M, Schwartz K, Muntoni F. Clinical and molecular genetic spectrum of autosomal dominant emery-dreifuss muscular dystrophy due to mutations of the lamin a/c gene. *Annals of neurology*. 2000;48:170-180

72.   Dahl KN, Ribeiro AJ, Lammerding J. Nuclear shape, mechanics, and mechanotransduction. *Circulation research*. 2008;102:1307-1318

73.   Lammerding J, Schulze PC, Takahashi T, Kozlov S, Sullivan T, Kamm RD, Stewart CL, Lee RT. Lamin a/c deficiency causes defective nuclear mechanics and mechanotransduction. *The Journal of clinical investigation*. 2004;113:370-378

74.   Wallace GQ, McNally EM. Mechanisms of muscle degeneration, regeneration, and repair in the muscular dystrophies. *Annual review of physiology*. 2009;71:37-57

75.   DiMauro S, Lamperti C. Muscle glycogenoses. *Muscle & nerve*. 2001;24:984-999

76.   DiMauro S, Spiegel R. Progress and problems in muscle glycogenoses. *Acta myologica : myopathies and cardiomyopathies : official journal of the Mediterranean Society of Myology / edited by the Gaetano Conte Academy for the study of striated muscle diseases*. 2011;30:96-102

77.   Dimauro S, Garone C. Metabolic disorders of fetal life: Glycogenoses and mitochondrial defects of the mitochondrial respiratory chain. *Seminars in fetal & neonatal medicine*. 2011;16:181-189

78.   Laforet P, Vianey-Saban C. Disorders of muscle lipid metabolism: Diagnostic and therapeutic challenges. *Neuromuscular disorders : NMD*. 2010;20:693-700

79.   Darras BT, Friedman NR. Metabolic myopathies: A clinical approach; part i. *Pediatric neurology*. 2000;22:87-97

80.   Darras BT, Friedman NR. Metabolic myopathies: A clinical approach; part ii. *Pediatric neurology*. 2000;22:171-181

81.   Lukjanenko L, Jung MJ, Hegde N, Perruisseau-Carrier C, Migliavacca E, Rozo M, Karaz S, Jacot G, Schmidt M, Li L, Metairon S, Raymond F, Lee U, Sizzano F, Wilson DH, Dumont NA, Palini A, Fassler R, Steiner P, Descombes P, Rudnicki MA, Fan C-M, von Maltzahn J, Feige JN, Bentzinger CF. Loss of fibronectin from the aged stem cell niche affects the regenerative capacity of skeletal muscle in mice. *Nat Med*. 2016;advance online publication

82.   Brislin RP, Theroux MC. Core myopathies and malignant hyperthermia susceptibility: A review. *Paediatric anaesthesia*. 2013;23:834-841

83.   Grounds MD, Sorokin L, White J. Strength at the extracellular matrix-muscle interface. *Scandinavian journal of medicine & science in sports*. 2005;15:381-391

84.   Sanes JR. The basement membrane/basal lamina of skeletal muscle. *The Journal of biological chemistry*. 2003;278:12601-12604

85.   Rybakova IN, Patel JR, Ervasti JM. The dystrophin complex forms a mechanically strong link between the sarcolemma and costameric actin. *The Journal of cell biology*. 2000;150:1209-1214

86.   Wilson KL, Berk JM. The nuclear envelope at a glance. *Journal of cell science*. 2010;123:1973-1978

87.   Clements L, Manilal S, Love DR, Morris GE. Direct interaction between emerin and lamin a. *Biochemical and biophysical research communications*. 2000;267:709-714

88.   Gruenbaum Y, Margalit A, Goldman RD, Shumaker DK, Wilson KL. The nuclear lamina comes of age. *Nature reviews. Molecular cell biology*. 2005;6:21-31

89.   Cortright RN, Muoio DM, Dohm GL. Skeletal muscle lipid metabolism: A frontier for new insights into fuel homeostasis. *The Journal of Nutritional Biochemistry*. 1997;8:228-245

90.   Jeukendrup AE. Regulation of fat metabolism in skeletal muscle. *Annals of the New York Academy of Sciences*. 2002;967:217-235

91.   Felig P, Wahren J. Fuel homeostasis in exercise. *The New England journal of medicine*. 1975;293:1078-1084

92.   Lamb GD. Excitation-contraction coupling in skeletal muscle: Comparisons with cardiac muscle. *Clinical and experimental pharmacology & physiology*. 2000;27:216-224

93.   Nance JR, Dowling JJ, Gibbs EM, Bonnemann CG. Congenital myopathies: An update. *Current neurology and neuroscience reports*. 2012;12:165-174

94.   Mayhew JE, Florence JM, Mayhew TP, Henricson EK, Leshner RT, McCarter RJ, Escolar DM. Reliable surrogate outcome measures in multicenter clinical trials of duchenne muscular dystrophy. *Muscle & nerve*. 2007;35:36-42

95.   Umemoto G, Furuya H, Kitashima A, Sakai M, Arahata H, Kikuta T. Dysphagia in duchenne muscular dystrophy versus myotonic dystrophy type 1. *Muscle & nerve*. 2012;46:490-495

96.   Brussock CM, Haley SM, Munsat TL, Bernhardt DB. Measurement of isometric force in children with and without duchenne's muscular dystrophy. *Physical therapy*. 1992;72:105-114

97.   Escolar DM, Henricson EK, Mayhew J, Florence J, Leshner R, Patel KM, Clemens PR. Clinical evaluator reliability for quantitative and manual muscle testing measures of strength in children. *Muscle & nerve*. 2001;24:787-793

98.   Juhas M, Engelmayr GC, Jr., Fontanella AN, Palmer GM, Bursac N. Biomimetic engineered muscle with capacity for vascular integration and functional maturation in vivo. *Proceedings of the National Academy of Sciences of the United States of America*. 2014;111:5508-5513

99.   Bian W, Bursac N. Engineered skeletal muscle tissue networks with controllable architecture. *Biomaterials*. 2009;30:1401-1412

100.   Vandenburgh H, Shansky J, Benesch-Lee F, Barbata V, Reid J, Thorrez L, Valentini R, Crawford G. Drug-screening platform based on the contractility of tissue-engineered muscle. *Muscle & nerve*. 2008;37:438-447

101.   Pirozzi KL, Long CJ, McAleer CW, Smith AS, Hickman JJ. Correlation of embryonic skeletal muscle myotube physical characteristics with contractile force generation on an atomic force microscope-based bio-microelectromechanical systems device. *Applied physics letters*. 2013;103:83108

102.   Madden L, Juhas M, Kraus WE, Truskey GA, Bursac N. Bioengineered human myobundles mimic clinical responses of skeletal muscle to drugs. *eLife*. 2015;4:e04885

103.   Liu Y, Sinha S, McDonald OG, Shang Y, Hoofnagle MH, Owens GK. Kruppel-like factor 4 abrogates myocardin-induced activation of smooth muscle gene expression. *The Journal of biological chemistry*. 2005;280:9719-9727

104.   Halayko AJ, Solway J. Molecular mechanisms of phenotypic plasticity in smooth muscle cells. *Journal of applied physiology*. 2001;90:358-368

105.   Akiho H, Tokita Y, Nakamura K, Satoh K, Nishiyama M, Tsuchiya N, Tsuchiya K, Ohbuchi K, Iwakura Y, Ihara E, Takayanagi R, Yamamoto M. Involvement of interleukin-17a-induced hypercontractility of intestinal smooth muscle cells in persistent gut motor dysfunction. *PloS one*. 2014;9:e92960

106.   Risse PA, Jo T, Suarez F, Hirota N, Tolloczko B, Ferraro P, Grutter P, Martin JG. Interleukin-13 inhibits proliferation and enhances contractility of human airway smooth muscle cells without change in contractile phenotype. *American journal of physiology. Lung cellular and molecular physiology*. 2011;300:L958-966

107.   Lee KM, Tsai KY, Wang N, Ingber DE. Extracellular matrix and pulmonary hypertension: Control of vascular smooth muscle cell contractility. *The American journal of physiology*. 1998;274:H76-82

108.   Wang F, He XY, Baines KJ, Gunawardhana LP, Simpson JL, Li F, Gibson PG. Different inflammatory phenotypes in adults and children with acute asthma. *The European respiratory journal*. 2011;38:567-574

109.   Lotvall J, Akdis CA, Bacharier LB, Bjermer L, Casale TB, Custovic A, Lemanske RF, Jr., Wardlaw AJ, Wenzel SE, Greenberger PA. Asthma endotypes: A new approach to classification of disease entities within the asthma syndrome. *The Journal of allergy and clinical immunology*. 2011;127:355-360

110.   Ohama T, Hori M, Ozaki H. Mechanism of abnormal intestinal motility in inflammatory bowel disease: How smooth muscle contraction is reduced? *Journal of smooth muscle research = Nihon Heikatsukin Gakkai kikanshi*. 2007;43:43-54

111.   Straumann A, Schoepfer AM. Therapeutic concepts in adult and paediatric eosinophilic oesophagitis. *Nature reviews. Gastroenterology & hepatology*. 2012;9:697-704

112.   Straumann A, Kristl J, Conus S, Vassina E, Spichtin HP, Beglinger C, Simon HU. Cytokine expression in healthy and inflamed mucosa: Probing the role of eosinophils in the digestive tract. *Inflammatory bowel diseases*. 2005;11:720-726

113.   Baumgart DC, Carding SR. Inflammatory bowel disease: Cause and immunobiology. *Lancet*. 2007;369:1627-1640

114.   Bouma G, Strober W. The immunological and genetic basis of inflammatory bowel disease. *Nature reviews. Immunology*. 2003;3:521-533

115. Wills-Karp M. Interleukin-13 in asthma pathogenesis. *Current allergy and asthma reports*. 2004;4:123-131

116. Wills-Karp M, Luyimbazi J, Xu X, Schofield B, Neben TY, Karp CL, Donaldson DD. Interleukin-13: Central mediator of allergic asthma. *Science*. 1998;282:2258-2261

117. Laporte JC, Moore PE, Baraldo S, Jouvin MH, Church TL, Schwartzman IN, Panettieri RA, Jr., Kinet JP, Shore SA. Direct effects of interleukin-13 on signaling pathways for physiological responses in cultured human airway smooth muscle cells. *Am J Respir Crit Care Med*. 2001;164:141-148

118. Chiba Y, Nakazawa S, Todoroki M, Shinozaki K, Sakai H, Misawa M. Interleukin-13 augments bronchial smooth muscle contractility with an up-regulation of rhoa protein. *Am J Respir Cell Mol Biol*. 2009;40:159-167

119. Akiho H, Lovato P, Deng Y, Ceponis PJ, Blennerhassett P, Collins SM. Interleukin-4- and -13-induced hypercontractility of human intestinal muscle cells-implication for motility changes in crohn's disease. *American journal of physiology. Gastrointestinal and liver physiology*. 2005;288:G609-615

120. Shi HZ, Xiao CQ, Zhong D, Qin SM, Liu Y, Liang GR, Xu H, Chen YQ, Long XM, Xie ZF. Effect of inhaled interleukin-5 on airway hyperreactivity and eosinophilia in asthmatics. *Am J Respir Crit Care Med*. 1998;157:204-209

121. Blanchard C, Wang N, Rothenberg ME. Eosinophilic esophagitis: Pathogenesis, genetics, and therapy. *The Journal of allergy and clinical immunology*. 2006;118:1054-1059

122. Gupta SK, Fitzgerald JF, Kondratyuk T, HogenEsch H. Cytokine expression in normal and inflamed esophageal mucosa: A study into the pathogenesis of allergic eosinophilic esophagitis. *Journal of pediatric gastroenterology and nutrition*. 2006;42:22-26

123. Aceves SS, Chen D, Newbury RO, Dohil R, Bastian JF, Broide DH. Mast cells infiltrate the esophageal smooth muscle in patients with eosinophilic esophagitis, express tgf-beta1, and increase esophageal smooth muscle contraction. *The Journal of allergy and clinical immunology*. 2010;126:1198-1204 e1194

124. Bradding P, Roberts JA, Britten KM, Montefort S, Djukanovic R, Mueller R, Heusser CH, Howarth PH, Holgate ST. Interleukin-4, -5, and -6 and tumor necrosis factor-alpha in normal and asthmatic airways: Evidence for the human mast cell as a source of these cytokines. *Am J Respir Cell Mol Biol*. 1994;10:471-480

125.   Barath P, Fishbein MC, Cao J, Berenson J, Helfant RH, Forrester JS. Tumor necrosis factor gene expression in human vascular intimal smooth muscle cells detected by in situ hybridization. *The American journal of pathology*. 1990;137:503-509

126.   Thomas PS, Yates DH, Barnes PJ. Tumor necrosis factor-alpha increases airway responsiveness and sputum neutrophilia in normal human subjects. *Am J Respir Crit Care Med*. 1995;152:76-80

127.   Boyle JJ, Weissberg PL, Bennett MR. Tumor necrosis factor-alpha promotes macrophage-induced vascular smooth muscle cell apoptosis by direct and autocrine mechanisms. *Arteriosclerosis, thrombosis, and vascular biology*. 2003;23:1553-1558

128.   Amrani Y, Chen H, Panettieri RA, Jr. Activation of tumor necrosis factor receptor 1 in airway smooth muscle: A potential pathway that modulates bronchial hyper-responsiveness in asthma? *Respiratory research*. 2000;1:49-53

129.   Ohama T, Hori M, Momotani E, Iwakura Y, Guo F, Kishi H, Kobayashi S, Ozaki H. Intestinal inflammation downregulates smooth muscle cpi-17 through induction of tnf-alpha and causes motility disorders. *American journal of physiology. Gastrointestinal and liver physiology*. 2007;292:G1429-1438

130.   Kudo M, Melton AC, Chen C, Engler MB, Huang KE, Ren X, Wang Y, Bernstein X, Li JT, Atabai K, Huang X, Sheppard D. Il-17a produced by alphabeta t cells drives airway hyper-responsiveness in mice and enhances mouse and human airway smooth muscle contraction. *Nat Med*. 2012;18:547-554

131.   Wuyts WA, Vanaudenaerde BM, Dupont LJ, Van Raemdonck DE, Demedts MG, Verleden GM. Interleukin-17--induced interleukin-8 release in human airway smooth muscle cells: Role for mitogen-activated kinases and nuclear factor-kappab. *The Journal of heart and lung transplantation : the official publication of the International Society for Heart Transplantation*. 2005;24:875-881

132.   Akiho H, Ihara E, Motomura Y, Nakamura K. Cytokine-induced alterations of gastrointestinal motility in gastrointestinal disorders. *World journal of gastrointestinal pathophysiology*. 2011;2:72-81

133.   Itoh H, Mukoyama M, Pratt RE, Gibbons GH, Dzau VJ. Multiple autocrine growth factors modulate vascular smooth muscle cell growth response to angiotensin ii. *The Journal of clinical investigation*. 1993;91:2268-2274

134.	Hautmann MB, Thompson MM, Swartz EA, Olson EN, Owens GK. Angiotensin ii-induced stimulation of smooth muscle alpha-actin expression by serum response factor and the homeodomain transcription factor mhox. *Circulation research*. 1997;81:600-610

135.	Owens GK, Geisterfer AA, Yang YW, Komoriya A. Transforming growth factor-beta-induced growth inhibition and cellular hypertrophy in cultured vascular smooth muscle cells. *The Journal of cell biology*. 1988;107:771-780

136.	Beppu LY, Anilkumar AA, Newbury RO, Dohil R, Broide DH, Aceves SS. Tgf-beta1-induced phospholamban expression alters esophageal smooth muscle cell contraction in patients with eosinophilic esophagitis. *The Journal of allergy and clinical immunology*. 2014;134:1100-1107 e1104

137.	Hautmann MB, Madsen CS, Owens GK. A transforming growth factor beta (tgfbeta) control element drives tgfbeta-induced stimulation of smooth muscle alpha-actin gene expression in concert with two carg elements. *The Journal of biological chemistry*. 1997;272:10948-10956

138.	Barnes PJ, Chung KF, Page CP. Inflammatory mediators and asthma. *Pharmacological reviews*. 1988;40:49-84

139.	Haworth SG. Pulmonary vascular remodeling in neonatal pulmonary hypertension. State of the art. *Chest*. 1988;93:133S-138S

140.	Panettieri RA, Tan EM, Ciocca V, Luttmann MA, Leonard TB, Hay DW. Effects of ltd4 on human airway smooth muscle cell proliferation, matrix expression, and contraction in vitro: Differential sensitivity to cysteinyl leukotriene receptor antagonists. *Am J Respir Cell Mol Biol*. 1998;19:453-461

141.	Polte TR, Eichler GS, Wang N, Ingber DE. Extracellular matrix controls myosin light chain phosphorylation and cell contractility through modulation of cell shape and cytoskeletal prestress. *American journal of physiology. Cell physiology*. 2004;286:C518-528

142.	Chan V, Burgess JK, Ratoff JC, O'Connor B J, Greenough A, Lee TH, Hirst SJ. Extracellular matrix regulates enhanced eotaxin expression in asthmatic airway smooth muscle cells. *Am J Respir Crit Care Med*. 2006;174:379-385

143. Hedin U, Thyberg J. Plasma fibronectin promotes modulation of arterial smooth-muscle cells from contractile to synthetic phenotype. *Differentiation; research in biological diversity*. 1987;33:239-246

144. Dekkers BG, Schaafsma D, Nelemans SA, Zaagsma J, Meurs H. Extracellular matrix proteins differentially regulate airway smooth muscle phenotype and function. *American journal of physiology. Lung cellular and molecular physiology*. 2007;292:L1405-1413

145. Hirst SJ, Twort CHC, Lee TH. Differential effects of extracellular matrix proteins on human airway smooth muscle cell proliferation and phenotype. *Am J Resp Cell Mol*. 2000;23:335-344

146. Cazzola M, Calzetta L, Rogliani P, Lauro D, Novelli L, Page CP, Kanabar V, Matera MG. High glucose enhances responsiveness of human airways smooth muscle via the rho/rock pathway. *Am J Respir Cell Mol Biol*. 2012;47:509-516

147. Xie Z, Gong MC, Su W, Xie D, Turk J, Guo Z. Role of calcium-independent phospholipase a2beta in high glucose-induced activation of rhoa, rho kinase, and cpi-17 in cultured vascular smooth muscle cells and vascular smooth muscle hypercontractility in diabetic animals. *The Journal of biological chemistry*. 2010;285:8628-8638

148. Reusch P, Wagdy H, Reusch R, Wilson E, Ives HE. Mechanical strain increases smooth muscle and decreases nonmuscle myosin expression in rat vascular smooth muscle cells. *Circulation research*. 1996;79:1046-1053

149. Stegemann JP, Hong H, Nerem RM. Mechanical, biochemical, and extracellular matrix effects on vascular smooth muscle cell phenotype. *Journal of applied physiology*. 2005;98:2321-2327

150. Lacolley P, Regnault V, Nicoletti A, Li Z, Michel JB. The vascular smooth muscle cell in arterial pathology: A cell that can take on multiple roles. *Cardiovascular research*. 2012;95:194-204

151. Boehme J, Sun X, Tormos KV, Gong W, Kellner M, Datar SA, Kameny RJ, Yuan JX, Raff GW, Fineman JR, Black SM, Maltepe E. Pulmonary artery smooth muscle cell hyperproliferation and metabolic shift triggered by pulmonary overcirculation. *American journal of physiology. Heart and circulatory physiology*. 2016;311:H944-H957

152.   Masoli M, Fabian D, Holt S, Beasley R, Global Initiative for Asthma P. The global burden of asthma: Executive summary of the gina dissemination committee report. *Allergy*. 2004;59:469-478

153.   Holt PG, Sly PD, Martinez FD, Weiss ST, Bjorksten B, von Mutius E, Wahn U. Drug development strategies for asthma: In search of a new paradigm. *Nature immunology*. 2004;5:695-698

154.   Giacoia GP. Incentive to study drugs in children and other governmental initiatives: Will patients with asthma benefit? *The Journal of allergy and clinical immunology*. 2000;106:S118-124

155.   Adcock IM, Caramori G, Chung KF. New targets for drug development in asthma. *Lancet*. 2008;372:1073-1087

156.   Bateman ED, Boushey HA, Bousquet J, Busse WW, Clark TJH, Pauwels RA, Pedersen SE, Grp GI. Can guideline-defined asthma control be achieved? The gaining optimal asthma control study. *Am J Resp Crit Care*. 2004;170:836-844

157.   Mullane K. The increasing challenge of discovering asthma drugs. *Biochemical pharmacology*. 2011;82:586-599

158.   Holmes AM, Solari R, Holgate ST. Animal models of asthma: Value, limitations and opportunities for alternative approaches. *Drug discovery today*. 2011;16:659-670

159.   Holgate ST, Polosa R. Treatment strategies for allergy and asthma. *Nature reviews. Immunology*. 2008;8:218-230

160.   Bush A, Menzies-Gow A. Phenotypic differences between pediatric and adult asthma. *Proceedings of the American Thoracic Society*. 2009;6:712-719

161.   Leckie MJ, ten Brinke A, Khan J, Diamant Z, O'Connor BJ, Walls CM, Mathur AK, Cowley HC, Chung KF, Djukanovic R, Hansel TT, Holgate ST, Sterk PJ, Barnes PJ. Effects of an interleukin-5 blocking monoclonal antibody on eosinophils, airway hyper-responsiveness, and the late asthmatic response. *Lancet*. 2000;356:2144-2148

162.   Flood-Page P, Swenson C, Faiferman I, Matthews J, Williams M, Brannick L, Robinson D, Wenzel S, Busse W, Hansel TT, Barnes NC, International Mepolizumab Study G. A

study to evaluate safety and efficacy of mepolizumab in patients with moderate persistent asthma. *Am J Respir Crit Care Med*. 2007;176:1062-1071

163.   Nair P, Pizzichini MM, Kjarsgaard M, Inman MD, Efthimiadis A, Pizzichini E, Hargreave FE, O'Byrne PM. Mepolizumab for prednisone-dependent asthma with sputum eosinophilia. *The New England journal of medicine*. 2009;360:985-993

164.   Pavord ID, Korn S, Howarth P, Bleecker ER, Buhl R, Keene ON, Ortega H, Chanez P. Mepolizumab for severe eosinophilic asthma (dream): A multicentre, double-blind, placebo-controlled trial. *Lancet*. 2012;380:651-659

165.   Ortega HG, Liu MC, Pavord ID, Brusselle GG, FitzGerald JM, Chetta A, Humbert M, Katz LE, Keene ON, Yancey SW, Chanez P, Investigators M. Mepolizumab treatment in patients with severe eosinophilic asthma. *The New England journal of medicine*. 2014;371:1198-1207

166.   Wenzel S. Severe asthma: From characteristics to phenotypes to endotypes. *Clin Exp Allergy*. 2012;42:650-658

167.   Wenzel SE. Asthma phenotypes: The evolution from clinical to molecular approaches. *Nat Med*. 2012;18:716-725

168.   Narayanan D, Adebiyi A, Jaggar JH. Inositol trisphosphate receptors in smooth muscle cells. *American journal of physiology. Heart and circulatory physiology*. 2012;302:H2190-2210

169.   Gunst SJ, Tang DD. The contractile apparatus and mechanical properties of airway smooth muscle. *The European respiratory journal*. 2000;15:600-616

170.   Uehata M, Ishizaki T, Satoh H, Ono T, Kawahara T, Morishita T, Tamakawa H, Yamagami K, Inui J, Maekawa M, Narumiya S. Calcium sensitization of smooth muscle mediated by a rho-associated protein kinase in hypertension. *Nature*. 1997;389:990-994

171.   Kureishi Y, Kobayashi S, Amano M, Kimura K, Kanaide H, Nakano T, Kaibuchi K, Ito M. Rho-associated kinase directly induces smooth muscle contraction through myosin light chain phosphorylation. *The Journal of biological chemistry*. 1997;272:12257-12260

172. Fukata Y, Amano M, Kaibuchi K. Rho-rho-kinase pathway in smooth muscle contraction and cytoskeletal reorganization of non-muscle cells. *Trends in pharmacological sciences*. 2001;22:32-39

173. Owens GK, Kumar MS, Wamhoff BR. Molecular regulation of vascular smooth muscle cell differentiation in development and disease. *Physiological reviews*. 2004;84:767-801

174. Gunst SJ, Zhang W. Actin cytoskeletal dynamics in smooth muscle: A new paradigm for the regulation of smooth muscle contraction. *American journal of physiology. Cell physiology*. 2008;295:C576-587

175. Zhang W, Wu Y, Du L, Tang DD, Gunst SJ. Activation of the arp2/3 complex by n-wasp is required for actin polymerization and contraction in smooth muscle. *American journal of physiology. Cell physiology*. 2005;288:C1145-1160

176. Mehta D, Tang DD, Wu MF, Atkinson S, Gunst SJ. Role of rho in ca(2+)-insensitive contraction and paxillin tyrosine phosphorylation in smooth muscle. *American journal of physiology. Cell physiology*. 2000;279:C308-318

177. Small JV. Geometry of actin-membrane attachments in the smooth muscle cell: The localisations of vinculin and alpha-actinin. *The EMBO journal*. 1985;4:45-49

178. Lehman W, Morgan KG. Structure and dynamics of the actin-based smooth muscle contractile and cytoskeletal apparatus. *Journal of muscle research and cell motility*. 2012;33:461-469

179. Zhang W, Gunst SJ. Interactions of airway smooth muscle cells with their tissue matrix: Implications for contraction. *Proceedings of the American Thoracic Society*. 2008;5:32-39

180. An SS, Laudadio RE, Lai J, Rogers RA, Fredberg JJ. Stiffness changes in cultured airway smooth muscle cells. *American journal of physiology. Cell physiology*. 2002;283:C792-801

181. Saha SK, Berry MA, Parker D, Siddiqui S, Morgan A, May R, Monk P, Bradding P, Wardlaw AJ, Pavord ID, Brightling CE. Increased sputum and bronchial biopsy il-13 expression in severe asthma. *J Allergy Clin Immun*. 2008;121:685-691

182.   Wills-Karp M, Chiaramonte M. Interleukin-13 in asthma. *Current opinion in pulmonary medicine*. 2003;9:21-27

183.   Grainge CL, Lau LCK, Ward JA, Dulay V, Lahiff G, Wilson S, Holgate S, Davies DE, Howarth PH. Effect of bronchoconstriction on airway remodeling in asthma. *New Engl J Med*. 2011;364:2006-2015

184.   Vignola AM, Kips J, Bousquet J. Tissue remodeling as a feature of persistent asthma. *The Journal of allergy and clinical immunology*. 2000;105:1041-1053

185.   Panettieri RA, Tan EML, Ciocca V, Luttmann MA, Leonard TB, Hay DWP. Effects of ltd4 on human airway smooth muscle cell proliferation, matrix expression, and contraction in vitro: Differential sensitivity to cysteinyl leukotriene receptor antagonists. *Am J Resp Cell Mol*. 1998;19:453-461

186.   Chetta A, Foresi A, DelDonno M, Bertorelli G, Pesci A, Olivieri D. Airways remodeling is a distinctive feature of asthma and is related to severity of disease. *Chest*. 1997;111:852-857

187.   Bai TR, Cooper J, Koelmeyer T, Pare PD, Weir TD. The effect of age and duration of disease on airway structure in fatal asthma. *Am J Resp Crit Care*. 2000;162:663-669

188.   Straumann A, Aceves SS, Blanchard C, Collins MH, Furuta GT, Hirano I, Schoepfer AM, Simon D, Simon HU. Pediatric and adult eosinophilic esophagitis: Similarities and differences. *Allergy*. 2012;67:477-490

189.   Fox VL, Nurko S, Teitelbaum JE, Badizadegan K, Furuta GT. High-resolution eus in children with eosinophilic "allergic" esophagitis. *Gastrointestinal endoscopy*. 2003;57:30-36

190.   Aceves SS, Newbury RO, Dohil R, Bastian JF, Broide DH. Esophageal remodeling in pediatric eosinophilic esophagitis. *The Journal of allergy and clinical immunology*. 2007;119:206-212

191.   Hirano I. Pathophysiology of achalasia. *Current gastroenterology reports*. 1999;1:198-202

192.   Spiess AE, Kahrilas PJ. Treating achalasia: From whalebone to laparoscope. *Jama*. 1998;280:638-642

193.	Park W, Vaezi MF. Etiology and pathogenesis of achalasia: The current understanding. *The American journal of gastroenterology*. 2005;100:1404-1414

194.	Khan WI, Collins SM. Gut motor function: Immunological control in enteric infection and inflammation. *Clinical and experimental immunology*. 2006;143:389-397

195.	Kumar V, Abbas AK, Fausto N, Aster JC. *Robbins and cotran pathologic basis of disease*. Elsevier Health Sciences; 2014.

196.	Hansen ML, Gunn PW, Kaelber DC. Underdiagnosis of hypertension in children and adolescents. *Jama*. 2007;298:874-879

197.	Falkner B, Lurbe E, Schaefer F. High blood pressure in children: Clinical and health policy implications. *Journal of clinical hypertension*. 2010;12:261-276

198.	Daniels SR, Loggie JM, Khoury P, Kimball TR. Left ventricular geometry and severe left ventricular hypertrophy in children and adolescents with essential hypertension. *Circulation*. 1998;97:1907-1911

199.	Sanchez A, Barth JD, Zhang L. The carotid artery wall thickness in teenagers is related to their diet and the typical risk factors of heart disease among adults. *Atherosclerosis*. 2000;152:265-266

200.	Flynn JT. Pharmacologic management of childhood hypertension: Current status, future challenges. *American journal of hypertension*. 2002;15:30S-33S

201.	Sinaiko AR. Hypertension in children. *The New England journal of medicine*. 1996;335:1968-1973

202.	Raj M. Essential hypertension in adolescents and children: Recent advances in causative mechanisms. *Indian journal of endocrinology and metabolism*. 2011;15 Suppl 4:S367-373

203.	Kotchen TA. Obesity-related hypertension: Epidemiology, pathophysiology, and clinical management. *American journal of hypertension*. 2010;23:1170-1178

204.	Bucher BS, Ferrarini A, Weber N, Bullo M, Bianchetti MG, Simonetti GD. Primary hypertension in childhood. *Current hypertension reports*. 2013;15:444-452

205.   Kotsis V, Stabouli S, Papakatsika S, Rizos Z, Parati G. Mechanisms of obesity-induced hypertension. *Hypertension research : official journal of the Japanese Society of Hypertension*. 2010;33:386-393

206.   Wagenseil JE, Mecham RP. Vascular extracellular matrix and arterial mechanics. *Physiological reviews*. 2009;89:957-989

207.   Hahn C, Schwartz MA. Mechanotransduction in vascular physiology and atherogenesis. *Nature reviews. Molecular cell biology*. 2009;10:53-62

208.   Milewicz DM, Guo DC, Tran-Fadulu V, Lafont AL, Papke CL, Inamoto S, Kwartler CS, Pannu H. Genetic basis of thoracic aortic aneurysms and dissections: Focus on smooth muscle cell contractile dysfunction. *Annual review of genomics and human genetics*. 2008;9:283-302

209.   Dingemans KP, Teeling P, Lagendijk JH, Becker AE. Extracellular matrix of the human aortic media: An ultrastructural histochemical and immunohistochemical study of the adult aortic media. *The Anatomical record*. 2000;258:1-14

210.   Isselbacher EM. Thoracic and abdominal aortic aneurysms. *Circulation*. 2005;111:816-828

211.   Jeremy RW, Huang H, Hwa J, McCarron H, Hughes CF, Richards JG. Relation between age, arterial distensibility, and aortic dilatation in the marfan syndrome. *The American journal of cardiology*. 1994;74:369-373

212.   Huang J, Davis EC, Chapman SL, Budatha M, Marmorstein LY, Word RA, Yanagisawa H. Fibulin-4 deficiency results in ascending aortic aneurysms: A potential link between abnormal smooth muscle cell phenotype and aneurysm progression. *Circulation research*. 2010;106:583-592

213.   Chung AW, Au Yeung K, Sandor GG, Judge DP, Dietz HC, van Breemen C. Loss of elastic fiber integrity and reduction of vascular smooth muscle contraction resulting from the upregulated activities of matrix metalloproteinase-2 and -9 in the thoracic aortic aneurysm in marfan syndrome. *Circulation research*. 2007;101:512-522

214.   Guo DC, Pannu H, Tran-Fadulu V, Papke CL, Yu RK, Avidan N, Bourgeois S, Estrera AL, Safi HJ, Sparks E, Amor D, Ades L, McConnell V, Willoughby CE, Abuelo D, Willing M, Lewis RA, Kim DH, Scherer S, Tung PP, Ahn C, Buja LM, Raman CS, Shete

SS, Milewicz DM. Mutations in smooth muscle alpha-actin (acta2) lead to thoracic aortic aneurysms and dissections. *Nature genetics*. 2007;39:1488-1493

215.   Zhu L, Vranckx R, Khau Van Kien P, Lalande A, Boisset N, Mathieu F, Wegman M, Glancy L, Gasc JM, Brunotte F, Bruneval P, Wolf JE, Michel JB, Jeunemaitre X. Mutations in myosin heavy chain 11 cause a syndrome associating thoracic aortic aneurysm/aortic dissection and patent ductus arteriosus. *Nature genetics*. 2006;38:343-349

216.   Toshner M, Tajsic T, Morrell NW. Pulmonary hypertension: Advances in pathogenesis and treatment. *British medical bulletin*. 2010;94:21-32

217.   Voelkel NF, Gomez-Arroyo J, Abbate A, Bogaard HJ, Nicolls MR. Pathobiology of pulmonary arterial hypertension and right ventricular failure. *European Respiratory Journal*. 2012;40:1555-1565

218.   Stern RC. Current concepts - the diagnosis of cystic fibrosis. *New Engl J Med*. 1997;336:487-491

219.   Stern RC. The diagnosis of cystic fibrosis. *The New England journal of medicine*. 1997;336:487-491

220.   Hays SR, Ferrando RE, Carter R, Wong HH, Woodruff PG. Structural changes to airway smooth muscle in cystic fibrosis. *Thorax*. 2005;60:226-228

221.   Eigen H, Bieler H, Grant D, Christoph K, Terrill D, Heilman DK, Ambrosius WT, Tepper RS. Spirometric pulmonary function in healthy preschool children. *Am J Respir Crit Care Med*. 2001;163:619-623

222.   Sastry BK, Narasimhan C, Reddy NK, Raju BS. Clinical efficacy of sildenafil in primary pulmonary hypertension: A randomized, placebo-controlled, double-blind, crossover study. *Journal of the American College of Cardiology*. 2004;43:1149-1153

223.   Camilleri M, Bharucha AE, di Lorenzo C, Hasler WL, Prather CM, Rao SS, Wald A. American neurogastroenterology and motility society consensus statement on intraluminal measurement of gastrointestinal and colonic motility in clinical practice. *Neurogastroenterology and motility : the official journal of the European Gastrointestinal Motility Society*. 2008;20:1269-1282

224.   Davis SD, Brody AS, Emond MJ, Brumback LC, Rosenfeld M. Endpoints for clinical trials in young children with cystic fibrosis. *Proceedings of the American Thoracic Society*. 2007;4:418-430

225.   Szefler SJ. Challenges in assessing outcomes for pediatric asthma. *The Journal of allergy and clinical immunology*. 2001;107:S456-464

226.   Remedios M, Campbell C, Jones DM, Kerlin P. Eosinophilic esophagitis in adults: Clinical, endoscopic, histologic findings, and response to treatment with fluticasone propionate. *Gastrointestinal endoscopy*. 2006;63:3-12

227.   Akinbami LJ, Schoendorf KC. Trends in childhood asthma: Prevalence, health care utilization, and mortality. *Pediatrics*. 2002;110:315-322

228.   Kuperman DA, Huang X, Koth LL, Chang GH, Dolganov GM, Zhu Z, Elias JA, Sheppard D, Erle DJ. Direct effects of interleukin-13 on epithelial cells cause airway hyperreactivity and mucus overproduction in asthma. *Nat Med*. 2002;8:885-889

229.   Barnes PJ. The cytokine network in asthma and chronic obstructive pulmonary disease. *Journal of Clinical Investigation*. 2008;118:3546-3556

230.   Guilbert TW, Morgan WJ, Zeiger RS, Mauger DT, Boehmer SJ, Szefler SJ, Bacharier LB, Lemanske RF, Strunk RC, Allen DB, Bloomberg GR, Heldt G, Krawiec M, Larsen G, Liu AH, Chinchilli VM, Sorkness CA, Taussig LM, Martinez FD. Long-term inhaled corticosteroids in preschool children at high risk for asthma. *New Engl J Med*. 2006;354:1985-1997

231.   Barnes PJ, Adcock IM. Glucocorticoid resistance in inflammatory diseases. *Lancet*. 2009;373:1905-1917

232.   Corren J, Lemanske RF, Hanania NA, Korenblat PE, Parsey MV, Arron JR, Harris JM, Scheerens H, Wu LC, Su Z, Mosesova S, Eisner MD, Bohen SP, Matthews JG. Lebrikizumab treatment in adults with asthma. *New Engl J Med*. 2011;365:1088-1098

233.   Zosky GR, Sly PD. Animal models of asthma. *Clin Exp Allergy*. 2007;37:973-988

234.   van der Worp HB, Howells DW, Sena ES, Porritt MJ, Rewell S, O'Collins V, Macleod MR. Can animal models of disease reliably inform human studies? *PLoS medicine*. 2010;7:e1000245

235.   Wright D, Sharma P, Ryu MH, Risse PA, Ngo M, Maarsingh H, Koziol-White C, Jha A, Halayko AJ, West AR. Models to study airway smooth muscle contraction in vivo, ex vivo and in vitro: Implications in understanding asthma. *Pulmonary pharmacology & therapeutics*. 2013;26:24-36

236.   Wang N, Tolic-Norrelykke IM, Chen J, Mijailovich SM, Butler JP, Fredberg JJ, Stamenovic D. Cell prestress. I. Stiffness and prestress are closely associated in adherent contractile cells. *American journal of physiology. Cell physiology*. 2002;282:C606-616

237.   Fabry B, Maksym GN, Shore SA, Moore PE, Panettieri RA, Butler JP, Fredberg JJ. Signal transduction in smooth muscle - selected contribution: Time course and heterogeneity of contractile responses in cultured human airway smooth muscle cells. *J Appl Physiol*. 2001;91:986-994

238.   An SS, Kim J, Ahn K, Trepat X, Drake KJ, Kumar S, Ling G, Purington C, Rangasamy T, Kensler TW, Mitzner W, Fredberg JJ, Biswal S. Cell stiffness, contractile stress and the role of extracellular matrix. *Biochemical and biophysical research communications*. 2009;382:697-703

239.   West AR, Zaman N, Cole DJ, Walker MJ, Legant WR, Boudou T, Chen CS, Favreau JT, Gaudette GR, Cowley EA, Maksym GN. Development and characterization of a 3d multicell microtissue culture model of airway smooth muscle. *American journal of physiology. Lung cellular and molecular physiology*. 2013;304:L4-16

240.   Humbert M, Durham SR, Kimmitt P, Powell N, Assoufi B, Pfister R, Menz G, Kay AB, Corrigan CJ. Elevated expression of messenger ribonucleic acid encoding il-13 in the bronchial mucosa of atopic and nonatopic subjects with asthma. *The Journal of allergy and clinical immunology*. 1997;99:657-665

241.   Prieto J, Lensmar C, Roquet A, Van der Ploeg I, Gigliotti D, Eklund A, Grunewald J. Increased interleukin-13 mrna expression in bronchoalveolar lavage cells of atopic patients with mild asthma after repeated low-dose allergen provocations. *Resp Med*. 2000;94:806-814

242.   Feinberg AW, Feigel A, Shevkoplyas SS, Sheehy S, Whitesides GM, Parker KK. Muscular thin films for building actuators and powering devices. *Science*. 2007;317:1366-1370

243.   Alford PW, Feinberg AW, Sheehy SP, Parker KK. Biohybrid thin films for measuring contractility in engineered cardiovascular muscle. *Biomaterials*. 2010;31:3613-3621

244.   Grosberg A, Alford PW, McCain ML, Parker KK. Ensembles of engineered cardiac tissues for physiological and pharmacological study: Heart on a chip. *Lab on a chip*. 2011;11:4165-4173

245.   Alford PW, Nesmith AP, Seywerd JN, Grosberg A, Parker KK. Vascular smooth muscle contractility depends on cell shape. *Integrative biology : quantitative biosciences from nano to macro*. 2011;3:1063-1070

246.   Alford PW, Dabiri BE, Goss JA, Hemphill MA, Brigham MD, Parker KK. Blast-induced phenotypic switching in cerebral vasospasm. *Proceedings of the National Academy of Sciences of the United States of America*. 2011;108:12705-12710

247.   Agarwal A, Goss JA, Cho A, McCain ML, Parker KK. Microfluidic heart on a chip for higher throughput pharmacological studies. *Lab on a chip*. 2013

248.   Sumino K, Sugar EA, Irvin CG, Kaminsky DA, Shade D, Wei CY, Holbrook JT, Wise RA, Castro M, Re ALAAC. Methacholine challenge test: Diagnostic characteristics in asthmatic patients receiving controller medications. *J Allergy Clin Immun*. 2012;130:69-+

249.   Boonsawat W, Salome CM, Woolcock AJ. Effect of allergen inhalation on the maximal response plateau of the dose-response curve to methacholine. *Am Rev Respir Dis*. 1992;146:565-569

250.   Badier M, Guillot C, Dubus JC. Bronchial challenge with carbachol in 3-6-year-old children: Body plethysmography assessments. *Pediatr Pulm*. 1999;27:117-123

251.   Feinberg AW, Alford PW, Jin H, Ripplinger CM, Werdich AA, Sheehy SP, Grosberg A, Parker KK. Controlling the contractile strength of engineered cardiac muscle by hierarchal tissue architecture. *Biomaterials*. 2012;33:5732-5741

252.   Grunstein MM, Hakonarson H, Leiter J, Chen M, Whelan R, Grunstein JS, Chuang S. Il-13-dependent autocrine signaling mediates altered responsiveness of ige-sensitized airway smooth muscle. *American journal of physiology. Lung cellular and molecular physiology*. 2002;282:L520-528

253.   Dekker FW, Schrier AC, Sterk PJ, Dijkman JH. Validity of peak expiratory flow measurement in assessing reversibility of airflow obstruction. *Thorax*. 1992;47:162-166

254.   Johnson M. Molecular mechanisms of beta(2)-adrenergic receptor function, response, and regulation. *The Journal of allergy and clinical immunology*. 2006;117:18-24; quiz 25

255.   Lipworth BJ, Clark RA, Dhillon DP, Brown RA, McDevitt DG. Beta-adrenoceptor responses to high doses of inhaled salbutamol in patients with bronchial asthma. *British journal of clinical pharmacology*. 1988;26:527-533

256.   Fairshter RD, Wilson AF. Response to inhaled metaproterenol and isoproterenol in asthmatic and normal subjects. *Chest*. 1980;78:44-50

257.   Fernandes LB, Fryer AD, Hirshman CA. M2 muscarinic receptors inhibit isoproterenol-induced relaxation of canine airway smooth-muscle. *J Pharmacol Exp Ther*. 1992;262:119-126

258.   Watson N, Eglen RM. Effects of muscarinic m(2) and m(3) receptor stimulation and antagonism on responses to isoprenaline of guinea-pig trachea in-vitro. *Brit J Pharmacol*. 1994;112:179-187

259.   Ebina M, Takahashi T, Chiba T, Motomiya M. Cellular hypertrophy and hyperplasia of airway smooth muscles underlying bronchial-asthma - a 3-d morphometric study. *Am Rev Respir Dis*. 1993;148:720-726

260.   Ebina M, Yaegashi H, Chiba R, Takahashi T, Motomiya M, Tanemura M. Hyperreactive site in the airway tree of asthmatic patients revealed by thickening of bronchial muscles. A morphometric study. *Am Rev Respir Dis*. 1990;141:1327-1332

261.   Togashi H, Emala CW, Hall IP, Hirshman CA. Carbachol-induced actin reorganization involves g(i) activation of rho in human airway smooth muscle cells. *Am J Physiol-Lung C*. 1998;274:L803-L809

262.   James A, Carroll N. Airway smooth muscle in health and disease; methods of measurement and relation to function. *The European respiratory journal*. 2000;15:782-789

263.   Lei M, Ghezzo H, Chen MF, Eidelman DH. Airway smooth muscle orientation in intraparenchymal airways. *J Appl Physiol*. 1997;82:70-77

264.   Bray MA, Sheehy SP, Parker KK. Sarcomere alignment is regulated by myocyte shape. *Cell motility and the cytoskeleton*. 2008;65:641-651

265. Volfson D, Cookson S, Hasty J, Tsimring LS. Biomechanical ordering of dense cell populations. *Proceedings of the National Academy of Sciences of the United States of America*. 2008;105:15346-15351

266. Halayko AJ, Camoretti-Mercado B, Forsythe SM, Vieira JE, Mitchell RW, Wylam ME, Hershenson MB, Solway J. Divergent differentiation paths in airway smooth muscle culture: Induction of functionally contractile myocytes. *Am J Physiol-Lung C*. 1999;276:L197-L206

267. Bai TR, Prasad FW. Abnormalities in airway smooth-muscle in fatal asthma. *Am Rev Respir Dis*. 1990;141:552-557

268. Halayko AJ, Salari H, Ma XF, Stephens NL. Markers of airway smooth muscle cell phenotype. *Am J Physiol-Lung C*. 1996;270:L1040-L1051

269. Schaafsma D, Bos IS, Zuidhof AB, Zaagsma J, Meurs H. The inhaled rho kinase inhibitor y-27632 protects against allergen-induced acute bronchoconstriction, airway hyperresponsiveness, and inflammation. *American journal of physiology. Lung cellular and molecular physiology*. 2008;295:L214-219

270. Capulli AK, Tian K, Mehandru N, Bukhta A, Choudhury SF, Suchyta M, Parker KK. Approaching the in vitro clinical trial: Engineering organs on chips. *Lab on a chip*. 2014

271. Mannino DM, Homa DM, Redd SC. Involuntary smoking and asthma severity in children: Data from the third national health and nutrition examination survey. *Chest*. 2002;122:409-415

272. Wardlaw AJ. The role of air pollution in asthma. *Clin Exp Allergy*. 1993;23:81-96

273. Quirce S, Barranco P. Cleaning agents and asthma. *J Investig Allergol Clin Immunol*. 2010;20:542-550; quiz 542p following 550

274. Szczeklik A, Nizankowska E. Clinical features and diagnosis of aspirin induced asthma. *Thorax*. 2000;55 Suppl 2:S42-44

275. Schuh S, Johnson DW, Callahan S, Canny G, Levison H. Efficacy of frequent nebulized ipratropium bromide added to frequent high-dose albuterol therapy in severe childhood asthma. *J Pediatr-Us*. 1995;126:639-645

276. Sankary RM, Jones CA, Madison JM, Brown JK. Muscarinic cholinergic inhibition of cyclic-amp accumulation in airway smooth-muscle - role of a pertussis toxin-sensitive protein. *Am Rev Respir Dis*. 1988;138:145-150

277. Tseng S, Kim R, Kim T, Morgan KG, Hai CM. F-actin disruption attenuates agonist-induced [ca2+], myosin phosphorylation, and force in smooth muscle. *Am J Physiol-Cell Ph*. 1997;272:C1960-C1967

278. Chen CS, Mrksich M, Huang S, Whitesides GM, Ingber DE. Geometric control of cell life and death. *Science*. 1997;276:1425-1428

279. Schram G, Fournier A, Leduc H, Dahdah N, Therien J, Vanasse M, Khairy P. All-cause mortality and cardiovascular outcomes with prophylactic steroid therapy in duchenne muscular dystrophy. *Journal of the American College of Cardiology*. 2013;61:948-954

280. Bushby K, Finkel R, Birnkrant DJ, Case LE, Clemens PR, Cripe L, Kaul A, Kinnett K, McDonald C, Pandya S, Poysky J, Shapiro F, Tomezsko J, Constantin C, Group DMDCCW. Diagnosis and management of duchenne muscular dystrophy, part 2: Implementation of multidisciplinary care. *The Lancet. Neurology*. 2010;9:177-189

281. Hamanaka-Kondoh S, Kondoh J, Tamine K, Hori K, Fujiwara S, Maeda Y, Matsumura T, Yasui K, Fujimura H, Sakoda S, Ono T. Tongue pressure during swallowing is decreased in patients with duchenne muscular dystrophy. *Neuromuscular disorders : NMD*. 2014;24:474-481

282. van den Engel-Hoek L, Erasmus CE, Hendriks JC, Geurts AC, Klein WM, Pillen S, Sie LT, de Swart BJ, de Groot IJ. Oral muscles are progressively affected in duchenne muscular dystrophy: Implications for dysphagia treatment. *Journal of neurology*. 2013;260:1295-1303

283. Webster MT, Manor U, Lippincott-Schwartz J, Fan C-M. Intravital imaging reveals ghost fibers as architectural units guiding myogenic progenitors during regeneration. *Cell stem cell*. 2016

284. Standish SM, Eversole LR. Regenerative changes in rat tongue muscle following crushing injury. *Oral surgery, oral medicine, and oral pathology*. 1970;30:87-98

285. Noden DM. Patterning of avian craniofacial muscles. *Developmental biology*. 1986;116:347-356

286.   Pasternak C, Wong S, Elson EL. Mechanical function of dystrophin in muscle cells. *The Journal of cell biology*. 1995;128:355-361

287.   Alexakis C, Partridge T, Bou-Gharios G. Implication of the satellite cell in dystrophic muscle fibrosis: A self-perpetuating mechanism of collagen overproduction. *American journal of physiology. Cell physiology*. 2007;293:C661-669

288.   Napadow VJ, Kamm RD, Gilbert RJ. A biomechanical model of sagittal tongue bending. *Journal of biomechanical engineering*. 2002;124:547-556

289.   Wedeen VJ, Reese TG, Napadow VJ, Gilbert RJ. Demonstration of primary and secondary muscle fiber architecture of the bovine tongue by diffusion tensor magnetic resonance imaging. *Biophysical journal*. 2001;80:1024-1028

290.   Kier WM, Smith KK. Tongues, tentacles and trunks - the biomechanics of movement in muscular-hydrostats. *Zool J Linn Soc-Lond*. 1985;83:307-324

291.   Grosberg A, Kuo PL, Guo CL, Geisse NA, Bray MA, Adams WJ, Sheehy SP, Parker KK. Self-organization of muscle cell structure and function. *PLoS computational biology*. 2011;7:e1001088

292.   Khatau SB, Hale CM, Stewart-Hutchinson PJ, Patel MS, Stewart CL, Searson PC, Hodzic D, Wirtz D. A perinuclear actin cap regulates nuclear shape. *Proceedings of the National Academy of Sciences of the United States of America*. 2009;106:19017-19022

293.   Ye GJ, Aratyn-Schaus Y, Nesmith AP, Pasqualini FS, Alford PW, Parker KK. The contractile strength of vascular smooth muscle myocytes is shape dependent. *Integrative biology : quantitative biosciences from nano to macro*. 2014;6:152-163

294.   Bray MA, Adams WJ, Geisse NA, Feinberg AW, Sheehy SP, Parker KK. Nuclear morphology and deformation in engineered cardiac myocytes and tissues. *Biomaterials*. 2010;31:5143-5150

295.   McGrath MJ, Mitchell CA, Coghill ID, Robinson PA, Brown S. Skeletal muscle lim protein 1 (slim1/fhl1) induces alpha 5 beta 1-integrin-dependent myocyte elongation. *American journal of physiology. Cell physiology*. 2003;285:C1513-1526

296. Nowak SJ, Nahirney PC, Hadjantonakis AK, Baylies MK. Nap1-mediated actin remodeling is essential for mammalian myoblast fusion. *Journal of cell science*. 2009;122:3282-3293

297. Fortier M, Comunale F, Kucharczak J, Blangy A, Charrasse S, Gauthier-Rouviere C. Rhoe controls myoblast alignment prior fusion through rhoa and rock. *Cell death and differentiation*. 2008;15:1221-1231

298. Zeschnigk M, Kozian D, Kuch C, Schmoll M, Starzinski-Powitz A. Involvement of m-cadherin in terminal differentiation of skeletal muscle cells. *Journal of cell science*. 1995;108 (Pt 9):2973-2981

299. Dabiri GA, Turnacioglu KK, Sanger JM, Sanger JW. Myofibrillogenesis visualized in living embryonic cardiomyocytes. *Proceedings of the National Academy of Sciences of the United States of America*. 1997;94:9493-9498

300. Pasqualini FS, Sheehy SP, Agarwal A, Aratyn-Schaus Y, Parker KK. Structural phenotyping of stem cell-derived cardiomyocytes. *Stem cell reports*. 2015;4:340-347

301. Lakonishok M, Muschler J, Horwitz AF. The alpha 5 beta 1 integrin associates with a dystrophin-containing lattice during muscle development. *Developmental biology*. 1992;152:209-220

302. Garcia AJ, Vega MD, Boettiger D. Modulation of cell proliferation and differentiation through substrate-dependent changes in fibronectin conformation. *Molecular biology of the cell*. 1999;10:785-798

303. Mayer U. Integrins: Redundant or important players in skeletal muscle? *The Journal of biological chemistry*. 2003;278:14587-14590

304. Street SF. Lateral transmission of tension in frog myofibers: A myofibrillar network and transverse cytoskeletal connections are possible transmitters. *Journal of cellular physiology*. 1983;114:346-364

305. Huijing PA. Muscular force transmission necessitates a multilevel integrative approach to the analysis of function of skeletal muscle. *Exercise and sport sciences reviews*. 2003;31:167-175

306.   Rahimov F, Kunkel LM. The cell biology of disease: Cellular and molecular mechanisms underlying muscular dystrophy. *The Journal of cell biology*. 2013;201:499-510

307.   Berens P. Circstat: A matlab toolbox for circular statistics. *J Stat Softw*. 2009;31:1-21

308.   Rezakhaniha R, Agianniotis A, Schrauwen JT, Griffa A, Sage D, Bouten CV, van de Vosse FN, Unser M, Stergiopulos N. Experimental investigation of collagen waviness and orientation in the arterial adventitia using confocal laser scanning microscopy. *Biomechanics and modeling in mechanobiology*. 2012;11:461-473

309.   Mauro A. Satellite cell of skeletal muscle fibers. *J Biophys Biochem Cytol*. 1961;9:493-495

310.   Cosgrove BD, Sacco A, Gilbert PM, Blau HM. A home away from home: Challenges and opportunities in engineering in vitro muscle satellite cell niches. *Differentiation; research in biological diversity*. 2009;78:185-194

311.   Snow MH. Myogenic cell formation in regenerating rat skeletal muscle injured by mincing. I. A fine structural study. *The Anatomical record*. 1977;188:181-199

312.   Snow MH. Myogenic cell formation in regenerating rat skeletal muscle injured by mincing. Ii. An autoradiographic study. *The Anatomical record*. 1977;188:201-217

313.   Mann CJ, Perdiguero E, Kharraz Y, Aguilar S, Pessina P, Serrano AL, Munoz-Canoves P. Aberrant repair and fibrosis development in skeletal muscle. *Skeletal muscle*. 2011;1:21

314.   Gilbert PM, Havenstrite KL, Magnusson KE, Sacco A, Leonardi NA, Kraft P, Nguyen NK, Thrun S, Lutolf MP, Blau HM. Substrate elasticity regulates skeletal muscle stem cell self-renewal in culture. *Science*. 2010;329:1078-1081

315.   Engler AJ, Griffin MA, Sen S, Bonnemann CG, Sweeney HL, Discher DE. Myotubes differentiate optimally on substrates with tissue-like stiffness: Pathological implications for soft or stiff microenvironments. *The Journal of cell biology*. 2004;166:877-887

316.   Powell CA, Smiley BL, Mills J, Vandenburgh HH. Mechanical stimulation improves tissue-engineered human skeletal muscle. *American journal of physiology. Cell physiology*. 2002;283:C1557-1565

317.   Mudera V, Smith AS, Brady MA, Lewis MP. The effect of cell density on the maturation and contractile ability of muscle derived cells in a 3d tissue-engineered skeletal muscle model and determination of the cellular and mechanical stimuli required for the synthesis of a postural phenotype. *Journal of cellular physiology*. 2010;225:646-653

318.   Nesmith AP, Wagner MA, Pasqualini FS, O'Connor BB, Pincus MJ, August PR, Parker KK. A human in vitro model of duchenne muscular dystrophy muscle formation and contractility. *The Journal of cell biology*. 2016

319.   McCain ML, Agarwal A, Nesmith HW, Nesmith AP, Parker KK. Micromolded gelatin hydrogels for extended culture of engineered cardiac tissues. *Biomaterials*. 2014;35:5462-5471

320.   Agarwal A, Farouz Y, Nesmith AP, Deravi LF, McCain ML, Parker KK. Micropatterning alginate substrates for in vitro cardiovascular muscle on a chip. *Advanced functional materials*. 2013;23:3738-3746

321.   Passerieux E, Rossignol R, Letellier T, Delage JP. Physical continuity of the perimysium from myofibers to tendons: Involvement in lateral force transmission in skeletal muscle. *Journal of structural biology*. 2007;159:19-28

322.   Webster MT, Manor U, Lippincott-Schwartz J, Fan CM. Intravital imaging reveals ghost fibers as architectural units guiding myogenic progenitors during regeneration. *Cell stem cell*. 2016;18:243-252

323.   McDermott MK, Chen T, Williams CM, Markley KM, Payne GF. Mechanical properties of biomimetic tissue adhesive based on the microbial transglutaminase-catalyzed crosslinking of gelatin. *Biomacromolecules*. 2004;5:1270-1279

324.   Siow KS, Britcher L, Kumar S, Griesser HJ. Plasma methods for the generation of chemically reactive surfaces for biomolecule immobilization and cell colonization - a review. *Plasma Process Polym*. 2006;3:392-418

325.   Sacco A, Doyonnas R, Kraft P, Vitorovic S, Blau HM. Self-renewal and expansion of single transplanted muscle stem cells. *Nature*. 2008;456:502-506

326.   Fan Y, Maley M, Beilharz M, Grounds M. Rapid death of injected myoblasts in myoblast transfer therapy. *Muscle & nerve*. 1996;19:853-860

327. Miller RG, Sharma KR, Pavlath GK, Gussoni E, Mynhier M, Lanctot AM, Greco CM, Steinman L, Blau HM. Myoblast implantation in duchenne muscular dystrophy: The san francisco study. *Muscle & nerve*. 1997;20:469-478

328. Boldrin L, Zammit PS, Morgan JE. Satellite cells from dystrophic muscle retain regenerative capacity. *Stem cell research*. 2015;14:20-29

329. Rozo M, Li L, Fan CM. Targeting beta1-integrin signaling enhances regeneration in aged and dystrophic muscle in mice. *Nat Med*. 2016

330. Hennig R, Lomo T. Firing patterns of motor units in normal rats. *Nature*. 1985;314:164-166

7 List of Publications

1. Sheehy SP, Grosberg A, Qin P, Behm D, Ferrier J, Eagleson M, **Nesmith AP**, Frull D, Falls J, Campbell P, McCain M, Willette R, Erding Hu, Parker KK. Recapitulating mature myocardium in an Organ-on-Chip platform with immature cardiac myocytes. <u>In preparation.</u>

2. Pasqualini FS, **Nesmith AP**, Horton RE, Sheehy SP, Parker KK. Mechanotransduction and Metabolism in Cardiomyocyte Microdomains. BioMed Research International. <u>In Review.</u>

3. Deravi LF, Sinatra NR, Chantre CO, **Nesmith AP**, Yuan H, Deravi SK, Goss JA, MacQueen LA, Badrossamy MR, Gonzalez GM, Phillips MS, Parker KK. Design and Fabrication of Fibrous Nanomaterials using Pull Spinning. Macromolecular Materials and Engineering. <u>In Review.</u>

4. Lind JU, Busbee TA, Valentine AD, Pasqualini FS, Yuan H, Park SJ, Yadid M, Kotikian A, **Nesmith AP**, Campbell P, Vlassak JJ, Lewis JA, Parker KK. 3D Printed, Instrumented Heart-on-a-chip Devices. Nature Materials. 24 October 2016.

5. **Nesmith AP**, Wagner MA, Pasqualini FS, Pincus MJ, August PR, Parker KK. A Human In Vitro Model of Duchenne Muscular Dystrophy Muscle Formation and Contractility. The Journal of Cell Biology. 3 October 2016.

6. Chal J, Ziad AT, Hestin M, Aivio S, Gobert B, Cherrier T, Hick A, **Nesmith AP**, Parker KK, Pourquie O. Generation of human muscle fibers and satellite-like cells from human pluripotent stem cells in vitro. Nature Protocols. 1 September 2016.

7. Ye GJ, **Nesmith AP**, Parker KK. The role of mechanotransduction on vascular smooth muscle myocytes cytoskeleton and contractile function. Anat Rec (Hoboken). 2014 Sep; 297(9):1758-69.

8. **Nesmith AP**, Agarwal A, McCain ML, Parker KK. Human airway musculature on a chip: an in vitro model of allergic asthmatic bronchoconstriction and bronchodilation. Lab Chip, 2014, 14, 3925-3936.

9. McCain ML, Agarwal A, Nesmith HW, **Nesmith AP**, Parker KK. Micromolded gelatin hydrogels for extended culture of engineered cardiac tissues Biomaterials. 2014 Jul;35(21):5462-71. 2014 April 14.

10. Ye GJC, Aratyn-Schaus Y, **Nesmith AP**, Pasqualini FS, Alford, PW, and Parker KK. The contractile strength of vascular smooth muscle myocytes is shape dependent. Integr. Biol., 2014; 6: 152-163

11. Agarwal A, Farouz Y, **Nesmith AP**, Deravi LF, McCain ML, Parker KK. Micropatterning Alginate Substrates for In Vitro Cardiovascular Muscle on a Chip. Adv. Funct. Mater. Adv. Funct. Mater. 2013; 23(30): 3738–46.

12. Grosberg A, **Nesmith AP**, Goss JA, Brigham MD, McCain ML, Parker KK. Muscle on a chip: In vitro contractility assays for smooth and striated muscle. J Pharmacol Toxicol Methods. 2012; 65:126-135.

13. Alford PW, **Nesmith AP**, Seywerd, JN, Grosberg A, Parker KK. Vascular smooth muscle contractility depends on cell shape. Integr. Biol. 2011;3(11):1063-1070.